Design, Microfabrication and Characterization of Capillary Force Actuators

A Dissertation

Presented to

the faculty of the School of Engineering and Applied Science

University of Virginia

in partial fulfillment

of the requirements for the degree
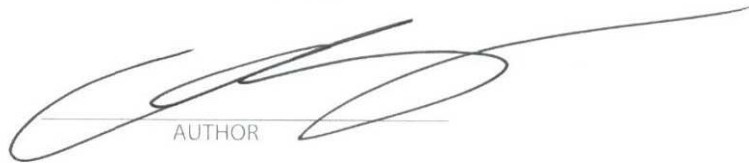
Doctor of Philosophy

by

Huihui Wang

August

2013

APPROVAL SHEET

The dissertation

is submitted in partial fulfillment of the requirements
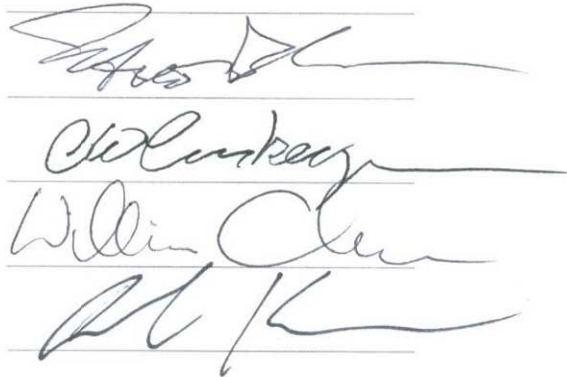
for the degree of

Doctor of Philosophy

AUTHOR

The dissertation has been read and approved by the examining committee:

Advisor

Accepted for the School of Engineering and Applied Science:

Dean, School of Engineering and Applied Science

August

2013

Abstract

Actuation converts one form of energy such as electrical, thermal, or chemical into mechanical energy acting on the physical world. Several Microsystem applications require forces and displacements exceeding the capabilities of conventional microscale actuation technologies.

Capillary Force Actuators (CFAs) are a new type of MEMS (Micro Electro Mechanical Systems) microactuator. They are capable of delivering significantly greater forces and larger actuation strokes than current technology. CFAs operate on a novel principle by employing a conducting liquid bridge between two surface electrodes covered with a thin dielectric layer. When the voltage is applied to the electrodes, the contact angle of the liquid changes, a process known as Electrowetting on Dielectric (EWOD). The contact angle change results in a change in the capillary pressure the droplet exerts on the surfaces, causing them to move in the direction normal to the surface. It has potential applications in microvalves of micro-total-analysis systems, in optical switch, in digital optics, and in variable capacitors in telecommunication systems.

This dissertation focuses on the design, microfabrication and experimental characterization of a CFA. We design standard CFA prototypes after the study of the physics of CFAs and FEA simulations. An optimized microfabrication process is proposed based on results from several trial and error experiments. We built up a displacement test platform to characterize CFAs' mechanical behaviors. A

nanonindenter method measures their force. As a result, we demonstrate the CFA actuation principle.

Meanwhile, EWOD prototypes are fabricated and characterized to understand the electrowetting phenomenon, which is involved in CFA physics. A contact angle measurement platform is set up by integrating electrical current measurements to study the electrowetting behaviors of our prototypes. In the electrowetting study, we focus on the study of contact angle change in response to different time modulated signals. After studying the influence of different materials of dielectric layers and hydrophobic layers, conductive liquids, and semiconductor wafers on the electrowetting, we identify suitable materials and conductive liquid solutions for a CFA prototype.

Acknowledgements

First and foremost, I would like to express my sincerest gratitude to my advisor, Prof. Michael Reed, for his inspiring mentorship via freedom to explore and create, encouragement, patience, confidence-building, and his financial support via the National Science Foundation under Grant ECCS 0801908. The years with his effective mentoring since June 2008 are the most enjoyable and productive time of my academic journey so far. He always has been and always will be my role model in my pursuit of academic excellence. I am equally in debt to Prof. Carl Knospe for his understanding and help when I faced difficulties during my studies. I am greatly indebted to Prof. Reed and Knospe for writing reference letters on my behalf to support my academic job search.

I would like to thank my dissertation advisory committee members, Prof. Scott Barker, Prof. Arthur Lichtenberger and Prof. William Messner, for their invaluable time and helpful suggestions. I would like to acknowledge Dr. Jianzhong Zhu for his guide and help in the early period of my PhD study and Mr John Gaskins for his help in the nanoindenter tests. Acknowledgement should be given to Dr. Lander's group in Chemistry department at UVa for lending us their expensive interferometer equipment. I also thank the engineers in the clean room i.e. Joe Beatrice, Harry Wade, Mariano Alexandre Lobo and Tim Pernell as well as Harry Powell in the ECE department. I would like to thank people working related with Capillary Force Actuators and Electrowetting projects.

Finally, I would like to thank my husband, Houbing Song, for his tireless support and unconditional love, and my parents as well as my aunt for their encouragement. This dissertation is impossible without the understanding of my parents-in-law.

Contents

List of Tables

List of Figures

1 Introduction

1.1 Microactuators

Microactuators, like microdrivers, microoptics, microfluids, positioning and gripper systems, are categorized based on their different physical principles or applications [1-9]. Four common types of microactuators are electrostatic, magnetic, piezoelectric and thermal. Electrostatic actuators are the most common due to their simple structures, quick response, high efficiency, low power consumption, and straightforward fabrication [10-23]. Magnetic microactuators have the ability to provide attractive and repulsive forces, unlike electrostatic actuators which can only generate attractive forces. The advantage of magnetic microactuators is their lack of friction when operated in levitation mode; however, their output force is small [24-26]. Thermal actuators can provide a considerably larger force and stroke; however they have a low actuation speed and high power consumption [27-29]. Piezoelectric microactuators take advantage of the coupling between mechanical deformation and electrical polarization, but they are limited due to few material choices that can withstand a large bending force and typically have very limited strokes [30, 31]. A summary of different microactuators in terms of force and displacement range is listed in Table 1.1 based on data in [1]. It is useful to compare force and displacements of different actuators by evaluating their size and power level. In this dissertation, we will focus on the comparison of a CFA with similarly sized electrostatic actuators. We will give a comparison mathematically in the Section 1.3.

Table 1.1 Microactuator Comparison [1]

Microactuators	Force	Displacement
Electrostatic	10^{-6}-10^{-3} N	10^{-6}-10^{-4} m
Electromagnetic	10^{-7}-10^{-4} N	10^{-5}-10^{-3} m
Thermal	10^{-5}-10^{-4} N	10^{-6}-10^{-4} m
Piezoelectric	10^{-6}-10^{-5} N	10^{-7}-10^{-3} m

1.2 Capillary Force Actuators

The Capillary Force Actuator (CFA) proposed by C. R. Knospe at UVa, is a new and promising technology for MEMS actuation, capable of delivering larger forces and larger strokes than current MEMS technologies [32]. As shown in Fig. 1.1, the CFA employs a conducting liquid bridge between two surfaces covered with electrodes, thin dielectrics, and hydrophobic layers. When voltage is applied to the electrodes, the contact angle of the liquid changes due to the fringing electrical field, a phenomenon known as Electrowetting on Dielectric (EWOD), which will be described in section 2.1. Due to the change in contact angle, the Laplace pressure of the droplet changes, causing the electrodes to move in the direction normal to the surface.
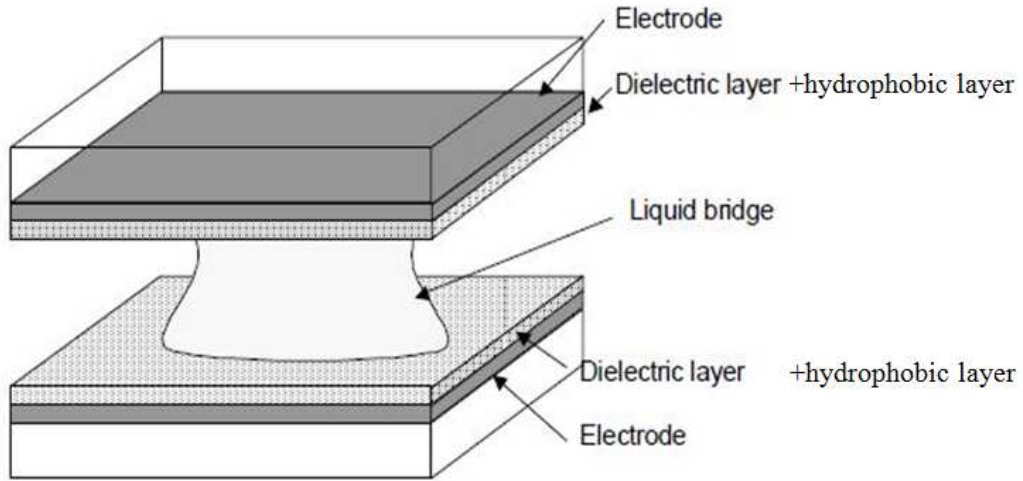
Fig. 1.1 Elements of a capillary force actuator [32]

1.3 An Electrostatic Perspective for Capillary Force Actuation

The advantages of a CFA can be understood through an explanation of the basic electrostatic principles of the actuation [32]. The following analysis derives from the work of Madou [5] and Nezamoddini [33].

The electrostatic energy stored in two parallel plates or a comb configuration is

$$E_1 = \frac{1}{2} C_1 V^2 \qquad (1.1)$$

where E_1 is the electrostatic energy, C_1 is the capacitance and V is the applied voltage. The electrostatic force F_1, is the negative spatial derivative of the electrostatic energy (potential energy). The force is generated due to the changing capacitance between the two plates due to distance variance:

$$F_1 = -\left(\frac{\partial E_1}{\partial x}\right)$$
$$= -\frac{1}{2}\left(\frac{\partial C_1}{\partial x}\right)V^2 \qquad (1.2)$$

Here $C_1 = \frac{\varepsilon_0 S_1}{h}$, ε_0 is the permittivity of free space, S_1 is the effective area, x is the

8

displacement, and h is the distance between the plates, V is the voltage between the plates.

$$\frac{\partial C_1}{\partial x} = -\frac{\varepsilon_0 S_1}{h^2}$$
(1.3)

We substitute Eqn.1.3 into Eqn.1.2 and get

$$F_1 = \frac{1}{2}\left(\frac{\varepsilon_0 S_1}{h^2}\right)V^2$$
(1.4)

For a CFA, the capacitance change is due to the change in the surface area of the liquid forming one plate of the capacitor. The capacitance is $C_2 = \frac{\varepsilon_d S_2}{t_d}$, ε_d is the effective dielectric constant of the layers, S_2 is the effective area between liquid and solid, t_d is the effective thickness of the dielectric layer and hydrophobic layer. Assuming the volume of the conductive liquid V_0 is constant,

$$dV_0 = S_2 \times dh + dS_2 \times h = 0 \Rightarrow dS_2 = -\frac{S_2}{h}dh = -\frac{S_2}{h}dx$$

$$F_2 = -\left(\frac{\partial E_2}{\partial x}\right)$$

$$= -\frac{1}{2}\left(\frac{\partial C_2}{\partial x}\right)V^2$$
(1.5)

Here E_2 is the electrostatic energy, and F_2 is the electrostatic component of the capillary force.

$$\frac{\partial C_2}{\partial x} = -\frac{1}{2}\frac{\varepsilon_d}{t_d}\frac{\partial S_2}{\partial x}V^2$$
(1.6)

Finally,

$$F_2 = \frac{1}{2}\frac{\varepsilon_d S_2}{t_d h}V^2$$
(1.7)

We can compare the forces of electrostatic actuators and CFAs based on Eqn. 1.4 and 1.7 as follows: assuming the surface area change of the capillary force actuator is

9

small, i.e. $S_1=S_2$,

$$\frac{\left(\dfrac{\partial C}{\partial x}\right)_{CFA}}{\left(\dfrac{\partial C}{\partial x}\right)_{electrostatc}} = \left(\frac{\varepsilon_d}{\varepsilon_0}\right)\left(\frac{h}{t_d}\right) \qquad (1.8)$$

Usually $\dfrac{\varepsilon_d}{\varepsilon_0} \geq 4$ and $\dfrac{h}{t_d} \geq 100$, so the capillary force is generally higher than that

of the traditional two plate electrostatic actuators, by a factor of greater than 400.

1.4 Dissertation Organization

The dissertation is organized as follows:

Chapter 2—Electrowetting will focus on electrowetting physics, a brief review of

the contact angle saturation phenomenon which is still a topic of considerable debate

in the electrowetting field, and our study of electrowetting behaviors in response to

various time modulated signals;

Chapter 3—Design will describe the physical design of the CFA, including the

corresponding mask design;

Chapter 4—Fabrication will discuss the fabrication process, fabrication results

and the final assembly process;

Chapter 5—Characterization will describe the CFA mechanical properties in terms

of the force and displacement;

Chapter 6—Conclusions and Future work will summarize the current research

work and explore potential future direction for the CFA.

2 Electrowetting

2.1 Electrowetting Basics

Electrocapillary wetting was introduced by Lippmann in 1875 [34]; Berge later initiated research of EWOD principles [35]. A general EWOD setup is shown in Fig. 2.1: a wetting liquid sits on top of a planar electrode covered with a thin dielectric layer and a hydrophobic layer. Applying a voltage between the liquid and the electrode changes the apparent contact angle of the wetting liquid. The contact angle is described by the Lippmann-Young equation [35]:

$$\cos \theta_v = \cos \theta_0 + \frac{\varepsilon_d}{2 t_d \sigma_{gl}} V^2 \tag{2.1}$$

where ε_d is the dielectric constant, t_d is the thickness of the dielectric layer, σ_{gl} is the air-liquid surface tension constant, θ_v is the apparent contact angle with an electric field, θ_0 is the natural contact angle without an electric field, and V is the voltage applied to the device.

In the past decade, electrowetting has been successfully applied to microfluidics [36-38], optical applications such as autofocus lenses [39] and display systems [40-42], and capillary motors [43]. However, some aspects of electrowetting are not fully understood. Contact angle saturation, for example, is a phenomenon not yet explained with current model. Methods from electrocapillary studies [44, 45] and electromechanics [46-49] have proposed the same description of the apparent contact angle (i.e., the macroscopic response); however, debate continues about the real

contact angle near the triple contact line (the microscopic response).
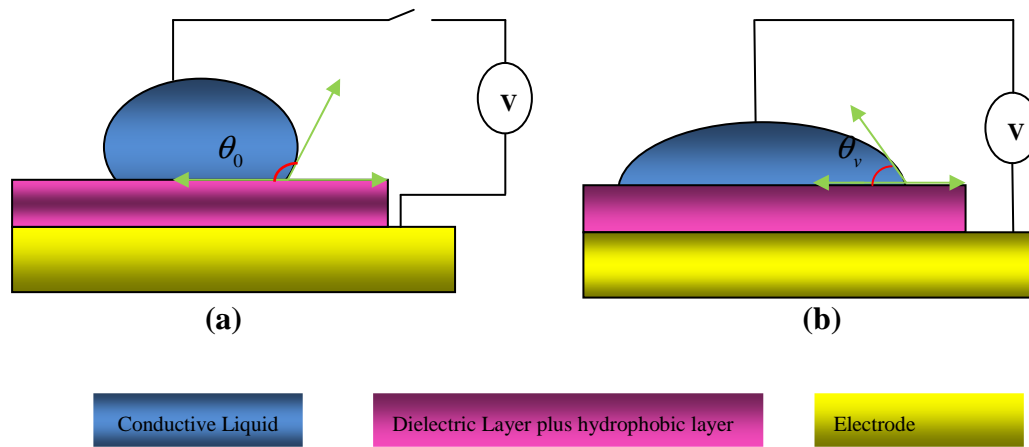
Fig. 2.1 A general setup of EWOD (a) Without bias (b) With bias

2.2 Contact Angle Saturation Review

In EWOD tests, especially tests with a sessile drop in air, the contact angle will not continue to change as the applied voltage increases; this is referred to as contact angle saturation. For example, the contact angle in Fig. 2.2. changes from 112 degree to 90 degree as the voltage increases and saturates at 90 degree after 13 V. This saturation behavior will limit CFA performance since the capillary force is related with the contact angle, see Eqn. 3.1. So during electrowetting tests, we will be interested in the voltage where the contact angle saturation occurs. As a result, prototype CFA devices will be operated below this voltage to avoid the influence of this contact angle saturation.
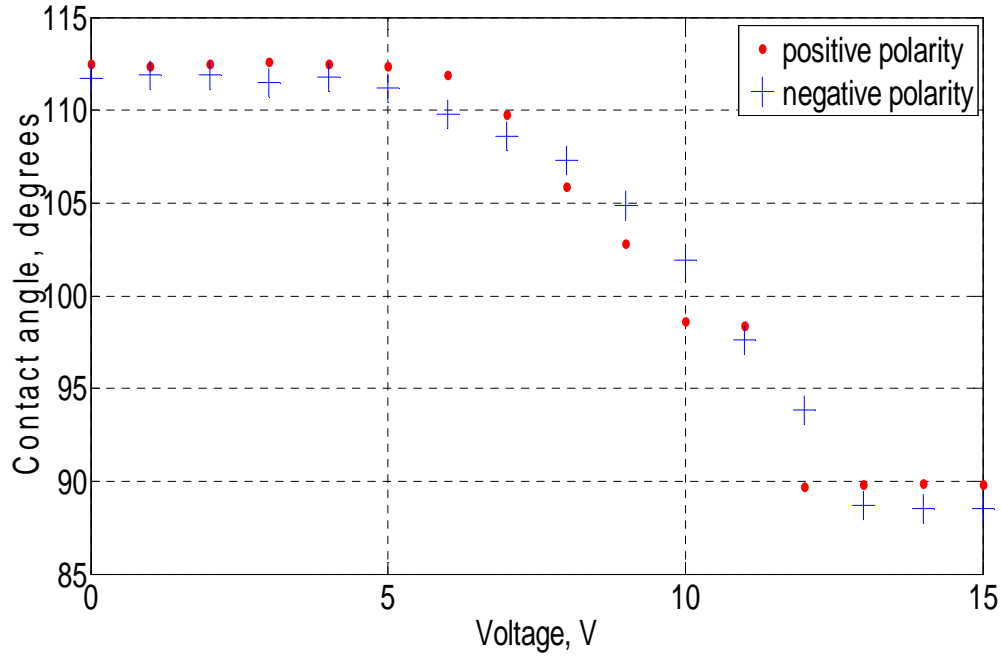
Fig. 2.2 An example of the contact angle change responding to DC voltage (wafer: P type, resist: 1-10 ohm.cm, the dielectric layer: 21 nm SiO$_2$, the hydrophobic layer: 22 nm Teflon AF1600 from DuPont [50], the drop is DI water plus 1 wt% NaCl, the red dots show results under the positive polarity to the drop, the blue dot show results under the negative polarity to the drop)

Over many years the phenomenon of contact angle saturation has been examined by researchers worldwide but is still poorly understood. Several hypotheses have been presented including nonlinear response of the material at high electric field [48], charge trapping [51], dielectric breakdown [37, 52], electrical resistance of the droplet [53], contact line instability [54], air ionization at the contact line [55], and zero solid-liquid interfacial surface tension [56-58].

Mugele proposed that the nonlinear response of the material due to the divergence of the electrical field at the contact line is likely to have the contact angle saturation [48]. Meanwhile, this theory also provides a good description of electrowetting after the calculation of the microscopic field distributions. After reviewing the existing mechanism of contact angle saturation, the paper suggests improving the dielectric

strength and the chemical inertness of the insulation layer in order to have better devices.

The charge trapping model is perhaps the most influential mechanism. Verheijen and Prins [51] proposed that charge in the liquid is injected into the solid at sufficiently high fields. By applying a charge to the solid that is opposite the sign of the charge generated by the power supply, the voltage drop across the interfacial layer is reduced. In this case, the electrowetting is not efficient resulting in contact angle saturation. This charge injection mechanism, however, has not been experimentally verified at this time.

Papathanasiou and Boudouvis made a connection between the dielectric breakdown strength and contact angle saturation [37, 52]. They argued that the crucial aspect of the contact angle saturation mechanism is the field strength close to the breakdown. They conducted a series of experiments on different dielectric materials to ascertain whether current leakage was related to the solid-liquid circle radius. They suggested that a stacked oxide-nitride-oxide (ONO) dielectric layer with a high breakdown strength is a good choice for some electrowetting devices.

For an experiment with a low-resistance liquid and a high-resistance dielectric, Shapiro et al [53] argued that the electrical resistance of a droplet will increase as the contact angle decreases due to the longer travel distance of ions in the liquid. However, Sedev [58] did not observe a significant difference in contact angle saturation in their experiments when they used solutions of different concentration.

Vallet et al [54] presented a phenomenon of the contact line instability, i.e. it was

suggested that using pure water and a voltage above a certain value, small droplets should be ejected from a large mother drop [54]. However, this instability phenomenon was suppressed when salt water was used. From the luminescence observed during experiments, they proposed that the contact angle saturation was due to the air ionization near but outside the contact line [51].

Sedev restated that the zero solid-liquid interfacial surface tension is not a mechanism hypothesis but that it merely demonstrated the limit of the Lippmann Young equation [58]. They tried to interpret the contact angle saturation from the thermodynamic limit perspective [56, 57]. However, Mugele [48] objected to this theory because of the poor understanding of absolute value of solid-liquid interfacial tension in the field of physical chemistry, no mechanism to destabilize the solid-liquid interface, and the constant solid-liquid interfacial tension during electrowetting. Since solid-liquid interfacial tension is poorly understood, the contact angle saturation may be interpreted well from the electromechanical perspective.

2.3 Contact Angle Measurement

Using the Lippmann-Young equation, it is logical to measure the contact angle change of a drop under an applied voltage in order to characterize the electrowetting phenomenon. This section introduces the sample preparation and the contact angle test platform, and presents the test results along with our analysis.

2.3.1 Sample Preparation

A 2 inch Si wafer with p type dopant (1-10 ohm.cm) is used as the electrode. A SiO$_2$ layer is thermally grown on Si in a rapid thermal annealing (RTA) machine. Fig. 2.3 demonstrates a relationship of the thickness of a SiO$_2$ layer vs. the temperature in RTA. After several tests, a 30 nm thick SiO$_2$ layer, grown at 1100ºC degree for 5 mins with a 100 sccm flow rate of O$_2$, was chosen as the dielectric layer .
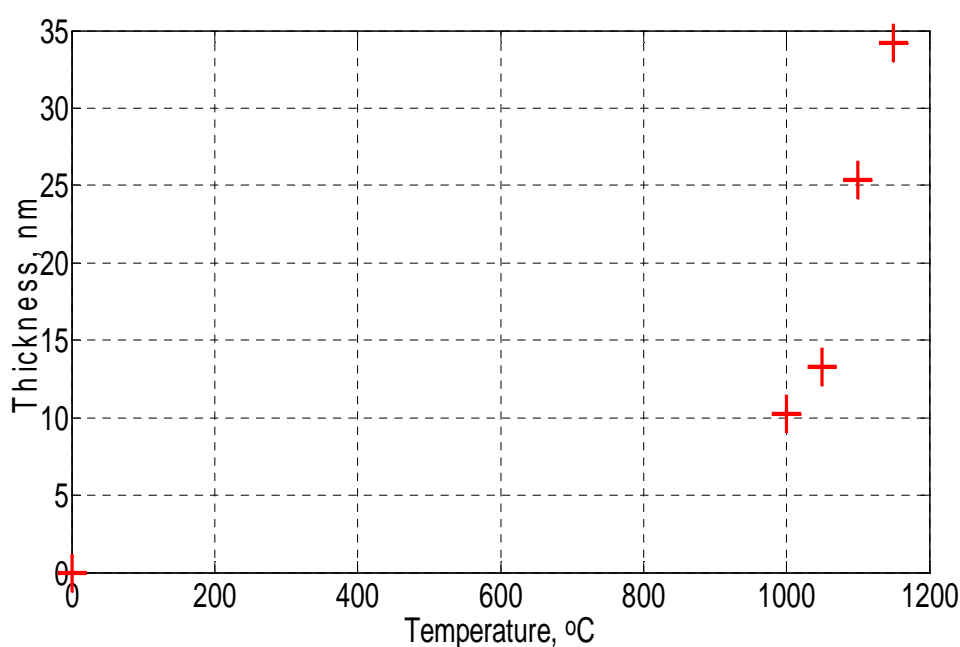
Fig. 2.3 SiO$_2$ layer thickness vs. temperature in RTA

Cytop, a fluoropolymer, from Asahi Glass company [59] is widely used in EWOD tests as a hydrophobic layer due to its easy realization of thinner layers and lower hysteresis. Before depositing this on top of the SiO$_2$ layer, an edge area of SiO$_2$ was covered with a small piece of tape for later electrical contact. A 30 nm thick hydrophobic layer was then partially spun on the SiO$_2$ layer at 2000 rpm for 30 s. The

wafer was then baked at 160ºC degree for half an hour after waiting for 5 mins at room temperature. In order to get a good electrical contact, the SiO_2 not covered by Cytop layer is removed in buffered oxide etchant (BOE). Finally, electrically conductive epoxy is used to connect a wire to this bare Si area, see Fig. 2.1. The substrate bias voltage is applied through a 50 µm diameter Au wire, wrapped on an Au needle and held in place by conductive epoxy. Samples are kept in a vacuum desiccator before testing to avoid contamination and surface degradation.

The thickness of the SiO_2 and Cytop layers are measured with an ellipsometer. The layer thicknesses are verified using an Atomic Force Microscope (AFM) instrument. Before each measurement, the surface qualities like the cleanness, roughness and morphology are checked using an optical microscope.

2.3.2 Contact Angle Measurement Platform

An important parameter characterizing electrowetting is the contact angle. We set up a contact angle test platform in our laboratory, see Fig. 2.4. It consists of two linear transfer stages, one for moving the wafer and the other one for aligning the needle just over the center of the drop. A microscope connected with a Panasonic GPKR222 video camera is used to record side views of the drop under time modulated signals. A Dazzle card with related Pinnacle software [60] was used to integrate the camera with a computer. For the DC test, a step DC voltage is provided by an Agilent 3136A power supply and controlled by Labview. A recorded video is processed by the Virtual Dub and Matlab programs. For the AC test, the signal is generated using a National

Instruments myDAQ card and a linear power supply controlled by Labivew, Fig. 2.5. This AC setup will also provide data for the dynamic displacement of a CFA actuator.
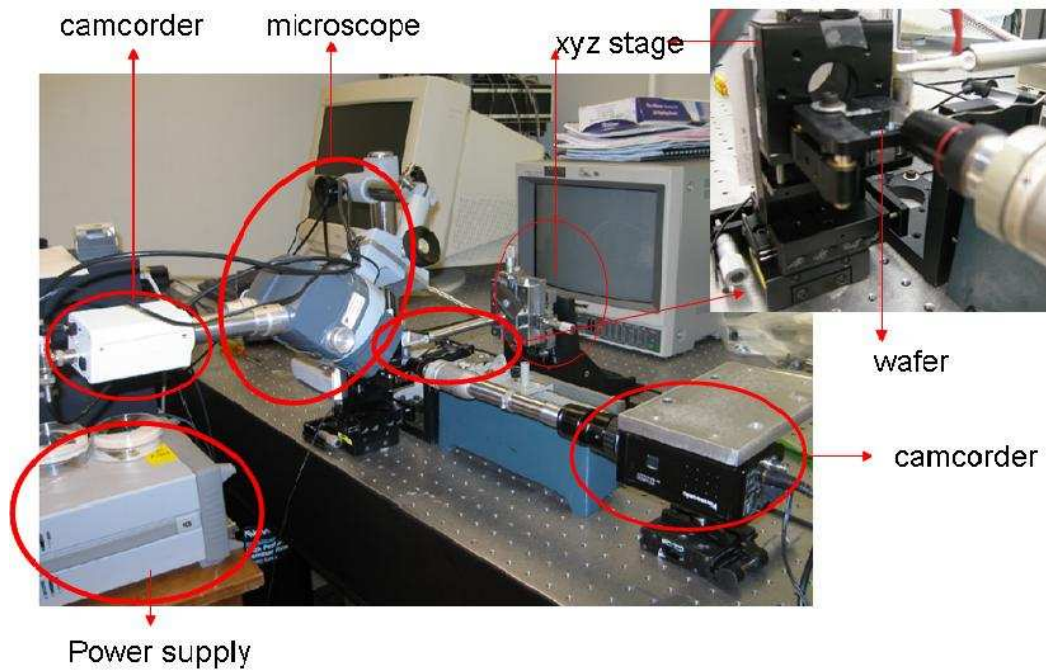
Fig. 2.4 A contact angle test platform
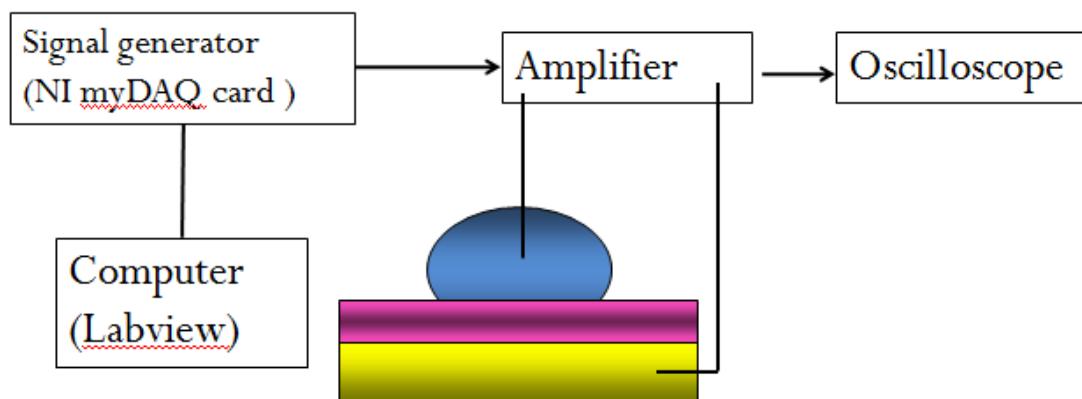
Fig. 2.5 An AC signal generation system

2.3.3 Contact Angle Measurement Test Results and Analysis

Since the capillary force is related with the contact angle, it is necessary to

understand how the contact angle of a droplet changes on thinner dielectric and hydrophobic layers. As a result, the contact angle measurements can provide useful information for our later CFA tests. We did many tests trying to determine best choices for time modulated signal range, Si wafers, liquid solution, and hydrophobic layer.

The contact angle measurement here focuses on the contact angle changes during DC and time modulated signals. In addition, we use Si wafers with different doping concentration and dielectric layer surface treatments. We also performed electrowetting tests on various hydrophobic layers including Teflon (from the Dupont company) and Cytop. Several types of solutions are used to study the electrowetting behavior, including 0.01 M NaCl solution, 0.01 M Na_2SO_4 solution, and deionized (DI) water plus propylene glycol.

A number of time modulated signals such as a step DC signal, a DC bias plus a constant amplitude AC signal, AC signals at 500 Hz, 1 kHz and 10 kHz, and an AC signal with variable amplitude and equal bias were applied. Table 2.1 summarizes the different time modulated signals.

Table 2.1 Summary of time modulated signals for electrowetting tests

Signal type	Amplitude	Frequency
DC	0-15 V	
AC	0-15 V	500 Hz, 1 kHz, or 10 kHz
AC+DC	AC and DC amplitudes equal and scanned from 0-15 V simultaneously	1 kHz or 10 kHz
AC+DC	AC: constant at 1 V DC: 0-20 V	1 kHz or 10 kHz

We also studied the influence that different wafer dopant types and concentration as well as the annealing treatment of a thinner dielectric layer have on the contact angle change. Table 2.2 lists a summary of different test cases mentioned above. The samples in these tests are still silicon wafers with a SiO_2 as a dielectric layer and Cytop as a hydrophobic layer. The drop is DI water mixed with sodium sulfate (Na_2SO_4) or DI water plus propylene glycol (PG) solution. We apply DC voltages with the amplitude scanned from 0 to 15 V and change voltage polarity to the drop. Representative test results are shown in Fig. 2.6-2.9.

Table 2.2 Summary of electrowetting tests on different wafers

Test group number	Wafer dopant type	Wafer resistivity	Dielectric layer treatment
1	P	1-10 ohm.cm	No annealing treatment
2	P	1-10 ohm.cm	Annealing treatment with Ar+H_2 gas
3	P	0.001-0.005 ohm.cm	Annealing treatment with Ar+H_2 gas
4	N	0.02-0.024 ohm.cm	No annealing treatment

Fig. 2.6 An Electrowetting test under AC voltage (AC amplitude: 0-15 V, frequency: 500 Hz, the drop shows there is an oscillation along the drop edge at 500 Hz)
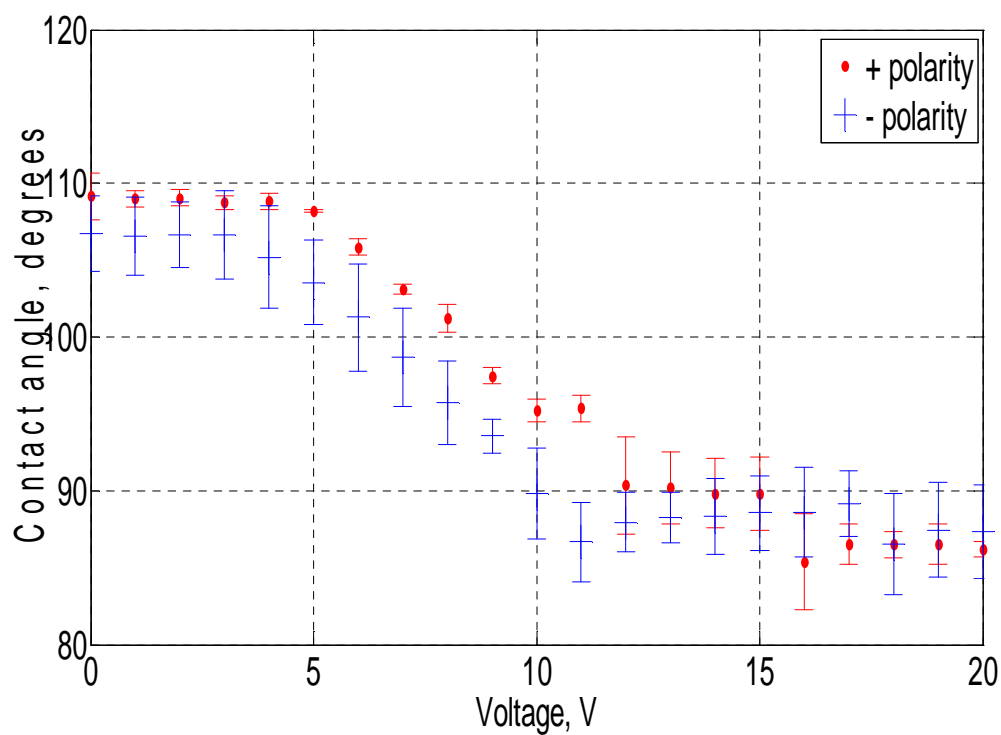
Fig. 2.7 Electrowetting test results of AC plus DC (AC amplitude: 1 V, frequency: 10 kHz, DC amplitude: 0-20 V, solution: Na_2SO_4+DI water, the red dots show results under the positive polarity to the drop, and the blue crosses show results under the negative polarity to the drop)
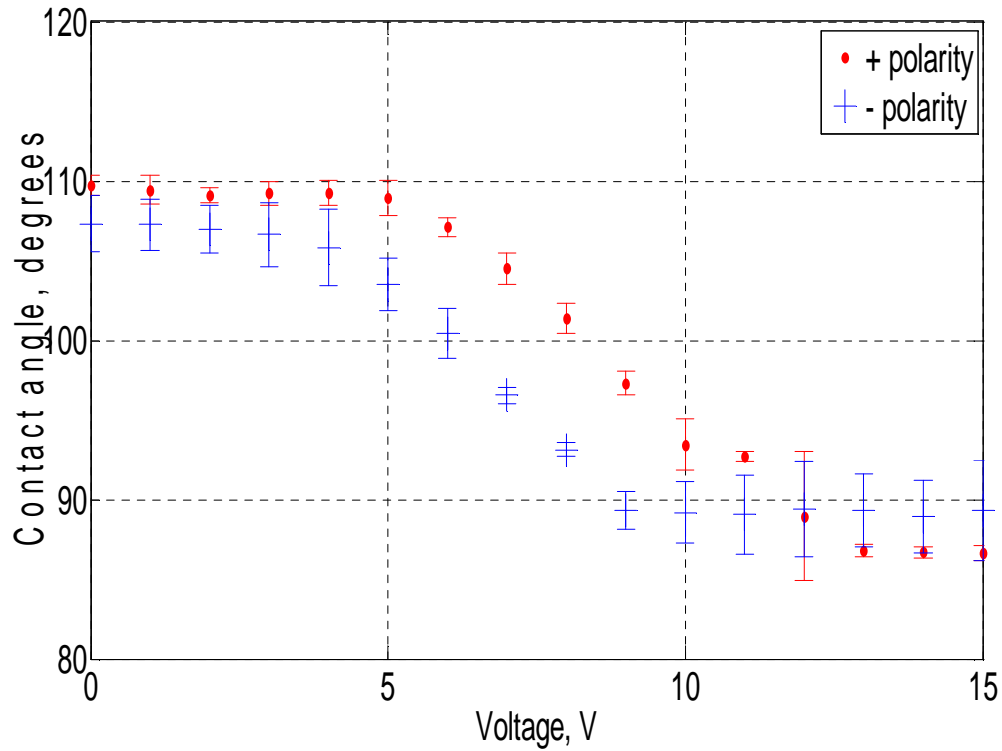
Fig. 2.8 Average results of the contact angle change responding to DC voltage (wafer: P type, resist: 1-10 ohm.cm, the dielectric layer without the forming gas treatment, the drop is DI water plus Na$_2$SO$_4$, the red dots show results under the positive polarity to the drop, and the blue crosses show results under the negative polarity to the drop)

From Fig. 2.6, we observe the oscillation along the drop curvature which has been mentioned in other papers [61, 62]. The electrowetting tests under time modulated voltages at a high frequency show that electrowetting has a 'quasi-static' behavior. That is why there is essentially no difference of contact angle change observed between the AC tests with a higher frequency and those with a DC signal applied, see Fig. 2.7-2.8.
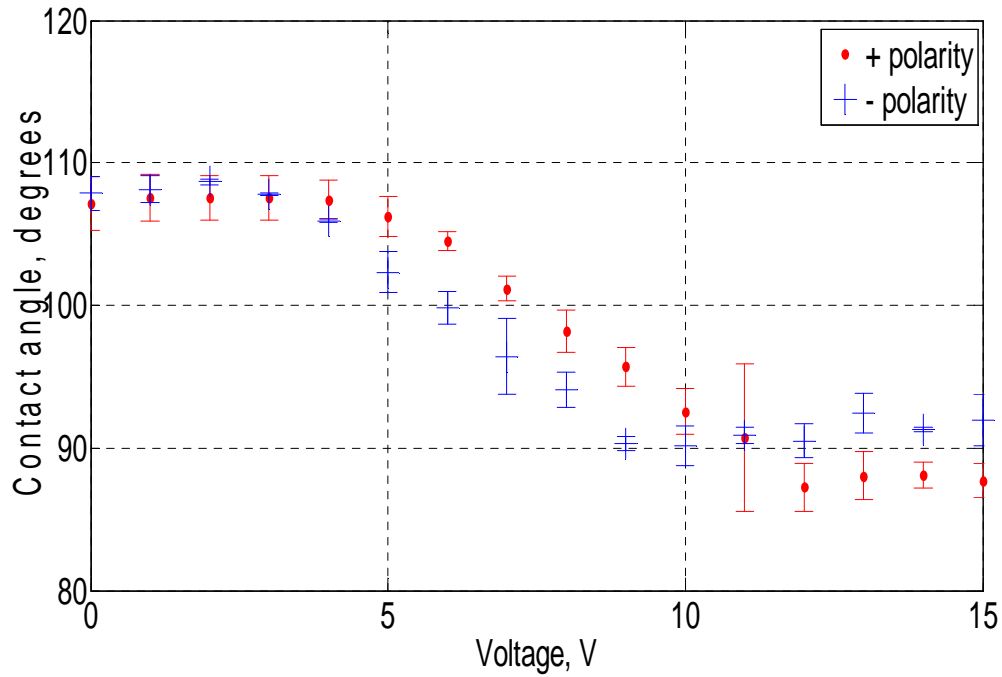
Fig. 2.9 Average results of the contact angle change responding to DC voltage (wafer: P type, resist: 1-10 ohm.cm, the dielectric layer with the forming gas treatment, the drop is DI water plus Na$_2$SO$_4$, the red dots show results under the positive polarity to the drop, and the blue crosses show results under the negative polarity to the drop)

In addition, the electrowetting tests under DC voltages show that the contact angle always starts to change at a lower voltage when the negative polarity power is applied to a drop compared with the case when a positive polarity power applied to the drop, see Fig. 2.7-2.9. This phenomenon is independent of the drop solution used, the dopant types, and the doping concentration of the wafers. The contact angle also changes at a lower voltage when the doping concentration of a silicon wafer is higher since it has a higher conductivity. We notice that the electrolysis is likely to happen when the dielectric layer is thinner (20 nm thick SiO$_2$) compared with a thicker dielectric layer (37 nm thick SiO$_2$). We tried to anneal a thinner SiO$_2$ layer in H$_2$ plus Ar forming gas after the thermal growth to get a higher quality dielectric layer. However, the

23

electrowetting test results do not show there is a difference in contact angle change when the dielectric layer is treated with or without the forming gas.

Table 2.3 lists a summary of tests on different hydrophobic layers like Teflon or Ctyop with different drop solutions used.

Table 2.3 Electrowetting tests with different solutions and on different hydrophobic layer

Test Group	Solution	Hydrophobic layer
1	DI+PG (1:1 volume ratio)	Teflon
2	DI+PG (3:1 volume ratio)	Teflon
3	1 wt% NaCl	Teflon
4	1 wt% NaCl	Cytop

Fig. 2.10 Average results of the contact angle change responding to DC voltage (wafer: P type, resist: 1-10 ohm.cm, the dielectric layer: 23 nm SiO$_2$, the hydrophobic layer: 32 nm Teflon, the drop is DI water plus propylene glycol (3:1 volume ratio), the red dots show results under the negative polarity to the drop, and blue crosses show results under the positive polarity to the drop)
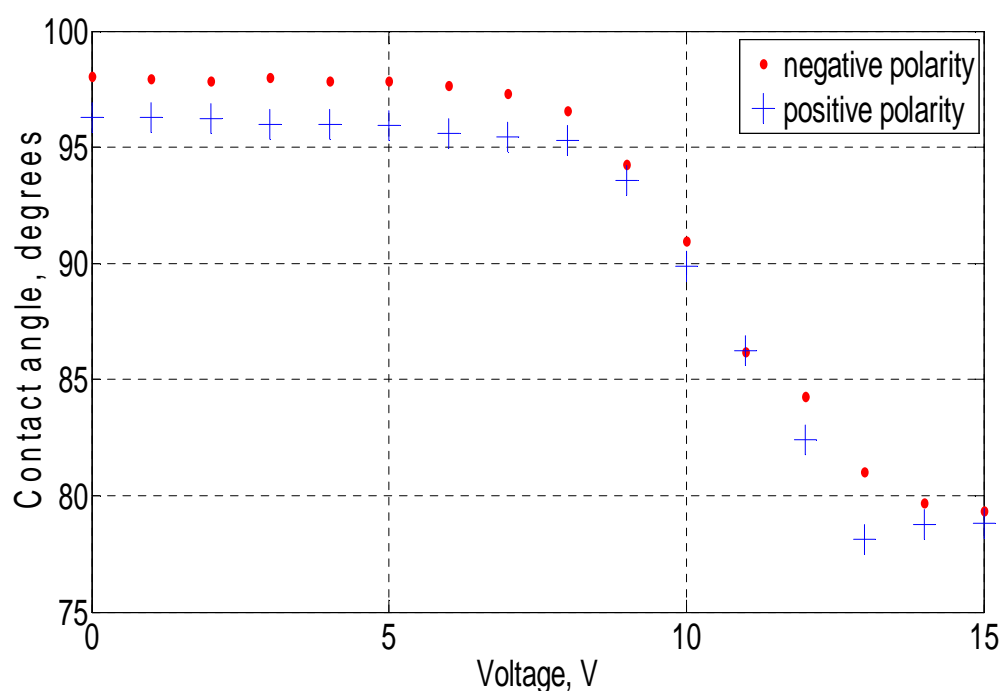
For tests with DI plus propylene glycol solution on a Teflon layer, the reader can observe that there is still a shift between different polarities to the drop, i.e. the contact angle changes at a lower voltage when the negative DC bias is applied to a droplet compared with that when the positive DC bias is applied to the droplet.

2.4 Hysteresis test

Hysteresis is defined as the difference between the advancing and receding contact angles. It is not expected that a hydrophobic layer will have significant hysteresis under time modulated signals; but such hysteresis would be harmful to actuator performance. So it is necessary to determine the hysteresis properties of various hydrophobic layers and determine a preparation method to achieve low hysteresis.

Several methods can be used to test the hysteresis such as tilting base method, i.e. measuring the difference of advancing and receding angles or a tensiometer based method, i.e. a dynamic method, to measure the advancing and receding angles. Here, we used a tensiometer K100 from Kruss considering its accuracy and easy operation.

We turn to the dynamic test method to characterize hysteresis on a Cytop layer with different solutions. We also examine the hysteresis of differently treated Cytop layers. Careful efforts were given to prepare samples with identical length (see Fig. 2.11) in order to have the same contact angles on both Si wafer surfaces.
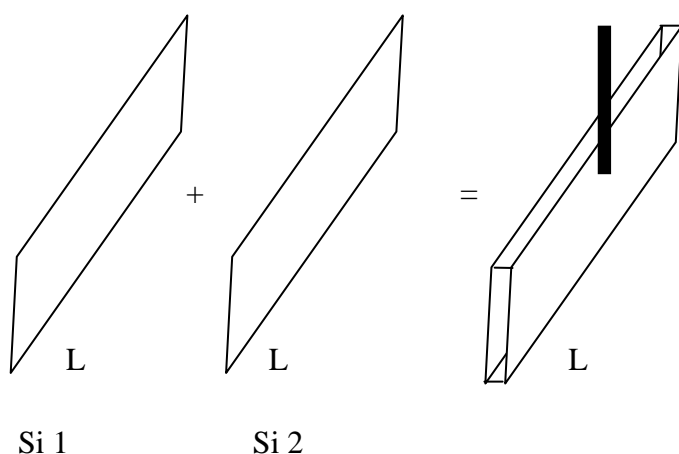
Fig. 2.11 Sample preparation for hysteresis test (two Si wafers with the same length L were glued together. A match bar was glued to one Si wafer for being held in the tensiometer.)

Fig. 2.11 shows how to prepare a sample for this hysteresis test. The important step is to maintain two pieces of wafers with the same length parameters in order to get an accurate contact angle hysteresis. Experiment results show that the contact angle hysteresis increases as we add either propylene glycol or salt water to DI water see Fig. 2.12. and 2.13.
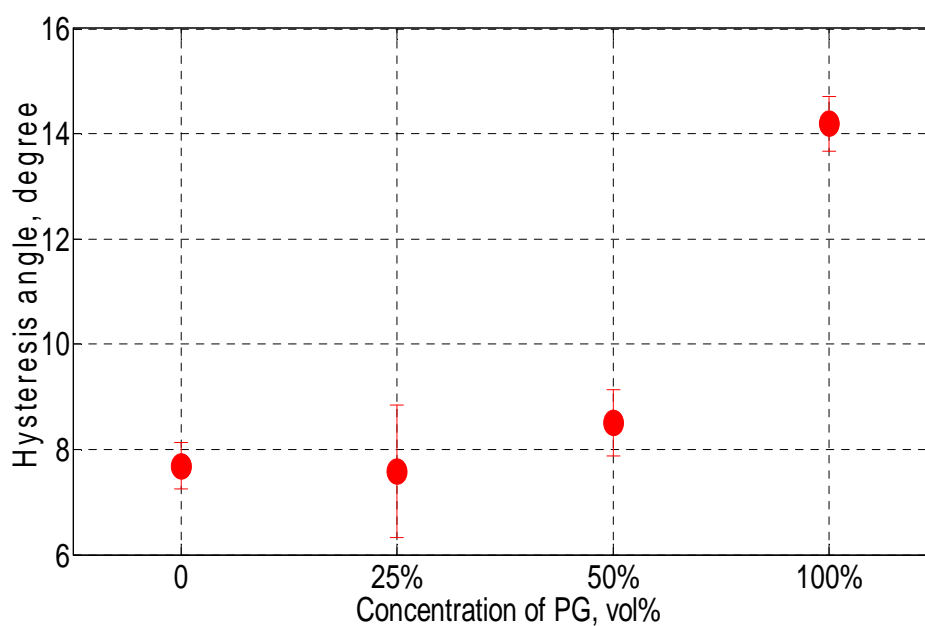
Fig. 2.12 Contact angle hysteresis vs. concentration of PG on Cytop, a hydrophobic layer
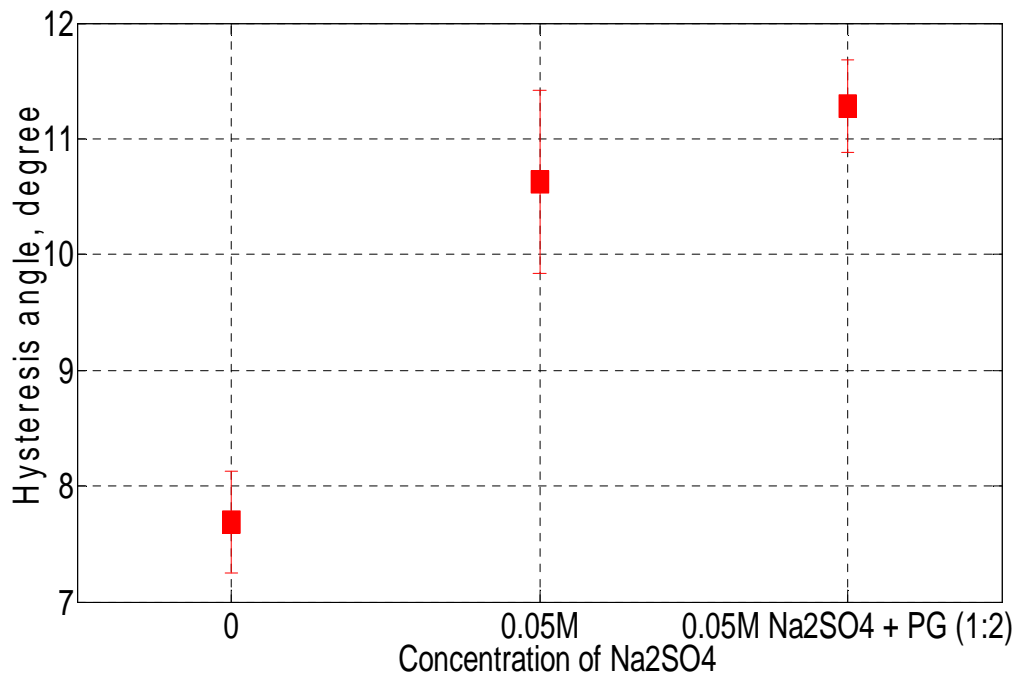
Fig. 2.13 Contact angle hysteresis versus concentration of Na$_2$SO$_4$ with or without PG

2.5 Summary

The electrowetting behavior of various samples were studied, especially with different time modulated signals. After we set up the contact angle test platform, we did many tests using time modulated signals, different conductive liquids, hydrophobic layers, and various wafer types. From the test results, we do not find there is a substantial difference in electrowetting between DC and AC signals at higher frequencies. This is because the bulk inertia of the droplet limits the response to fast signals, i.e. AC signals at a high frequency. From the Lippmann-Young equation it is understood that the droplet shape depends on the applied voltage. Thus, the voltage amplitude is a key parameter for the contact angle change.

To minimize evaporation, increase conductivity, and limit hysteresis, a Na$_2$SO$_4$

plus propylene glycol/DI water solution was chosen as the solution for the CFA prototype. Cytop was chosen as a hydrophobic layer since it is easy to form a thin layer (30 nm) at a lower spin speed (1000 rpm), and it has a smaller contact angle hysteresis compared with those of Teflon. Also, we observed that the contact angle usually starts changing at a lower voltage when negative polarity is applied to the drop compared with the case of the positive polarity; the mechanism for this is not yet clear.

3 Design

3.1 Physical Design

Following the study of CFA physics, the original CFA prototype was designed as shown in Fig. 3.1. This prototype takes into consideration the design guidelines developed by Nezamoddini [33], fabrication issues, and design experiences. The design of a top moving plate begins with a common structure: a movable central mass with flexures. Parameters of the CFA prototypes were chosen as shown in Table 3.1.

| Support structure | SiO₂ | Conductive Liquid | SOI wafer | Cytop |
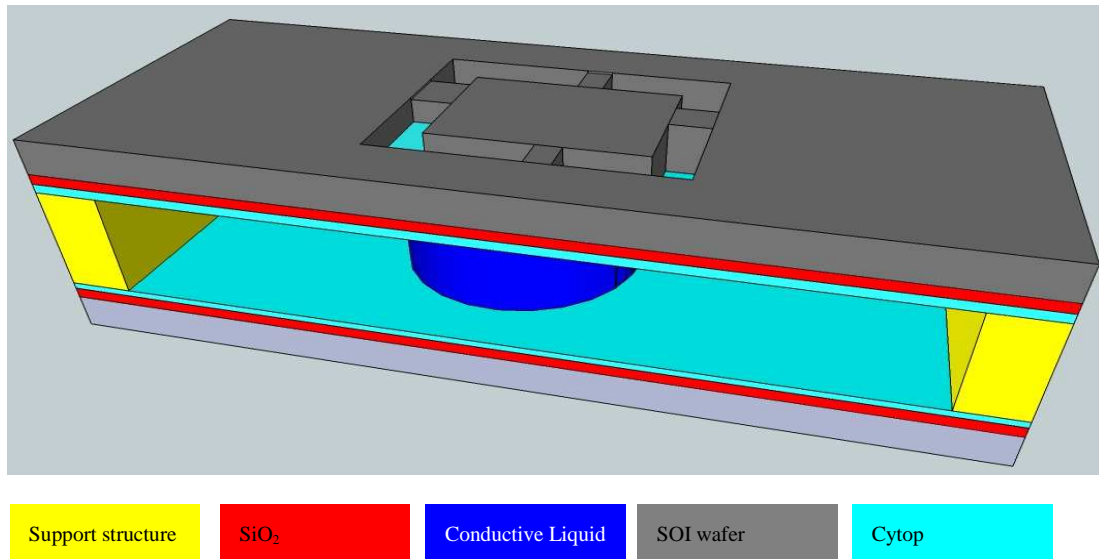
Fig. 3.1 Prototype design of the CFA

Based on electrowetting tests, we decided to keep using a thinner dielectric layer and a hydrophobic layer since we wish to operate our CFA in a low voltage range. Considering the available lab facilities, we choose the gap between two plates, the volume of a conductive liquid, and the length of each element square. Finally, we

calculate the force exerted on a CFA top platen based on Eqn. 3.1 [33].

$$F = -2\pi r \sigma \left(\frac{1}{2} + \frac{r}{h} \cos \theta_v \right)$$ (3.1)

Here, F is the capillary force acting on the moving plate, r is the liquid radius on the

solid surface, h is the liquid height, σ is the surface tension of the conductive liquid,

and θ_v is the apparent contact angle.

Table 3.1 Design Parameters

Parameter	Value
Voltage	20 V
Dielectric constant of the dielectric layer	3.8
Dielectric layer thickness	30 nm
Dielectric constant of the hydrophobic layer	1.8
Hydrophobic layer thickness	30 nm
Surface tension of the conductive liquid	50 mN/m
Gap between two plates	100 µm
Radius of the squashed conductive liquid	546 µm
Volume of the conductive liquid	0.1 µL
Length of the central mass square	2 mm
Total force on the moving plate	1.35 mN

The major design consideration is how to fabricate a released top platen structure,

i.e. the suspended structures connected with the central mass square. Considering the

microfabrication technologies available in our clean room, we employed a bulk

microfabrication technology. Silicon on Insulator (SOI) wafer is a good choice to

30

release a structure with a controllable thickness using this microfabrication technology.

Taking into account available device layer thicknesses in commercial SOI wafers, and

the mask resolution for the photolithography step, the thickness and the width of the

suspended structures were chosen as 3 μm and 30 μm respectively. To select the length

of the suspended structure, we were guided by Nezamoddini's design chart [33]. The

CFA will produce a sufficiently large force, resulting in a significant out of plane

displacement which precludes the use of linear beam deflection equations to calculate

the necessary beam length; the linear beam model is only accurate when the

displacement is small.

We determined on the beam length using nonlinear beam theory and Finite

Element Analysis (FEA) simulation. Beam nonlinearity is largely due to two effects:

intrinsic material nonlinearity (the stress/strain relation is nonlinear), and the extrinsic

geometry nonlinearity due to the constrained geometry. Only the extrinsic geometry

nonlinearity is important in this CFA design. The main sources of the geometric

nonlinearity are large axial stress and large geometric deflection. It has been shown

that the geometric nonlinearity arises at a very small displacement (less than 1 μm)

compared with the thickness (2 μm) of a fixed-fixed beam (200 μm long and 20 μm

wide) which is widely used in MEMS structures [63]. In [63], Qi demonstrates that the

large axial stress is an important source of geometric nonlinearity based on ABAQUS

simulations. When this geometric nonlinearity occurs, the beam acts as a stretching

string. Here we also notice this geometric nonlinearity based on ANSYS simulation

results, see Fig. 3.2. The fixed-fixed beam is 20 μm long, 1 μm wide and 1 μm thick. It

shows that the beam has this stretching string behavior when the displacement is about

5 μm.
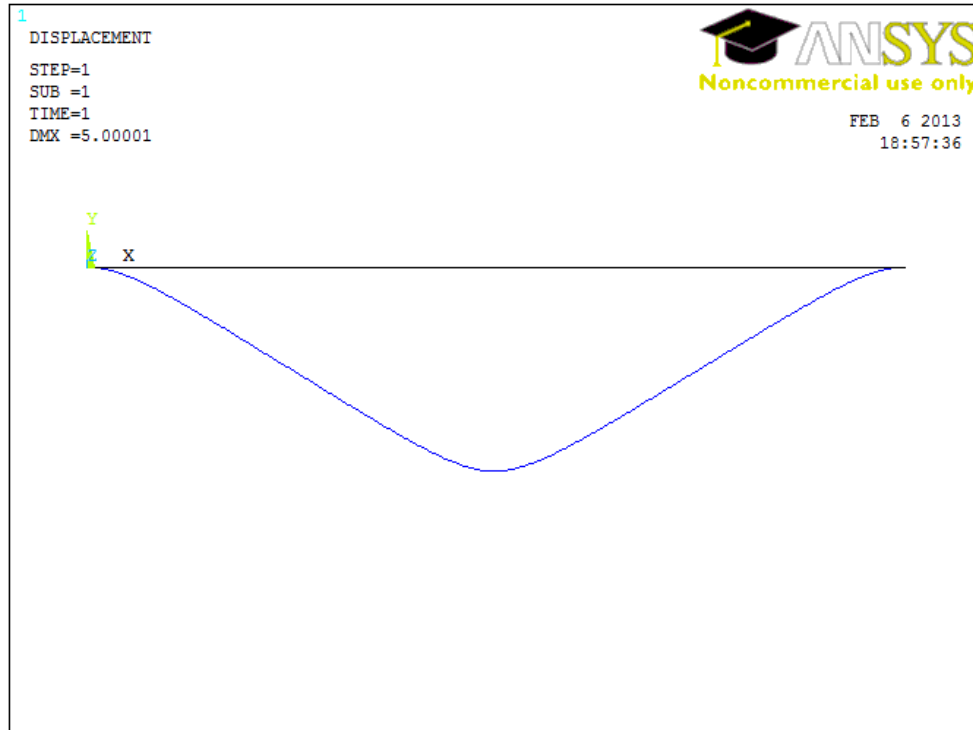
Fig. 3.2 ANSYS simulation result (The fixed-fixed beam is 20 μm long, 1 μm wide and 1 μm thick under a central point force. The beam has shown the streching string behavior when the dispalcement is about 5 μm.)

Based on the discussion about the geometry nonlinearity and FEA simulation results, we calculate the beam length based on the maximum out of plane displacement (30 μm) predicted by design chart in [33].

F_y
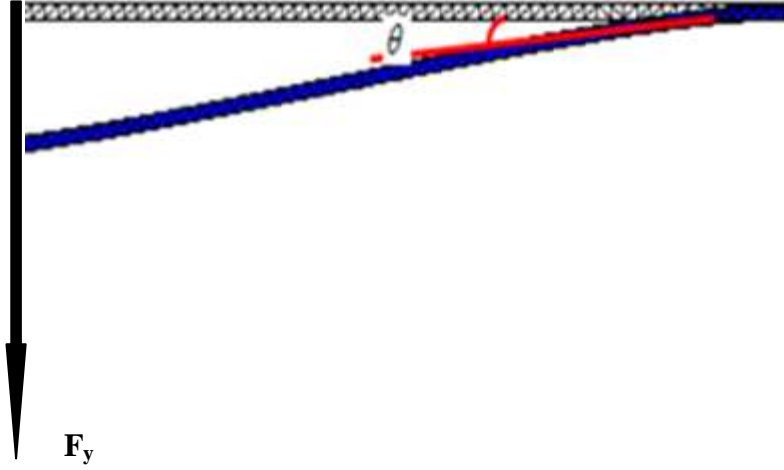
Fig. 3.3 The geometry of a deformed beam having a streching string behavior

The dimensions of the beam can be estimated using the following equation,

$$F_y = EA\varepsilon \sin^2 \theta \qquad (3.2)$$

Here $E = 180GPa$, the Young's Modulus of Si; $A = bh = 90\mu m^2$, the cross sectional

area; $b = 30\mu m$, the beam width; $h = 3\mu m$, the beam thickness; ε is the axial strain of

the beam, and θ is the angle shown in Fig. 3.3. Based on the geometric relationship,

the beam length is about $285\mu m$.

After the initial design of the suspended beam, we move to mask design and

fabrication process steps. However, because we frequently encountered crack failure in

the beam gap region during the XeF$_2$ etching step, we designed a series of masks with

different beam length in order to optimize the beam length. The mask included beam

length ranging from 200 µm to 350 µm. Finally, we identify the optimized beam

length at about 250 µm.

After the design of the suspended beam structures on a top platen, simulation is

done by ANSYS, see Fig. 3.4. We choose element solid 185 for a central mass and

element shell 63 for beams. Young's modulus is 180 GPa and Poisson ratio is 0.27.

Fig. 3.5 shows that the simulated displacement vs. force of both single-beam and two-beam designs connected with a central mass. To conserve simulation time, we only simulate the quarter of a top platen structure since it is symmetric. From the simulation results, we can tell that the force/displacement relationship is nonlinear, and results confirm the approximation used in our design of the suspended structures. The displacement of the single beam is double as that of the double beam structure when the force is smaller than 10 μN. The geometry nonlinearity is apparent in earlier when the force applied to a single beam structure. The simulation results indicate the feasibility of our design.
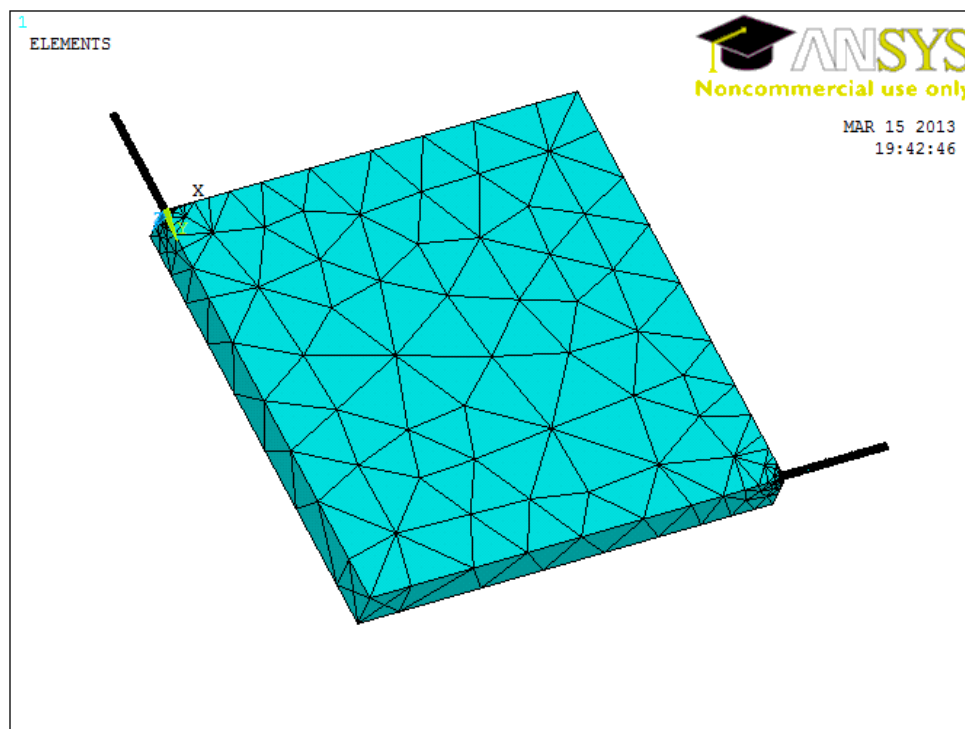
Fig. 3.4 A quarter of the suspended structure on the top platen
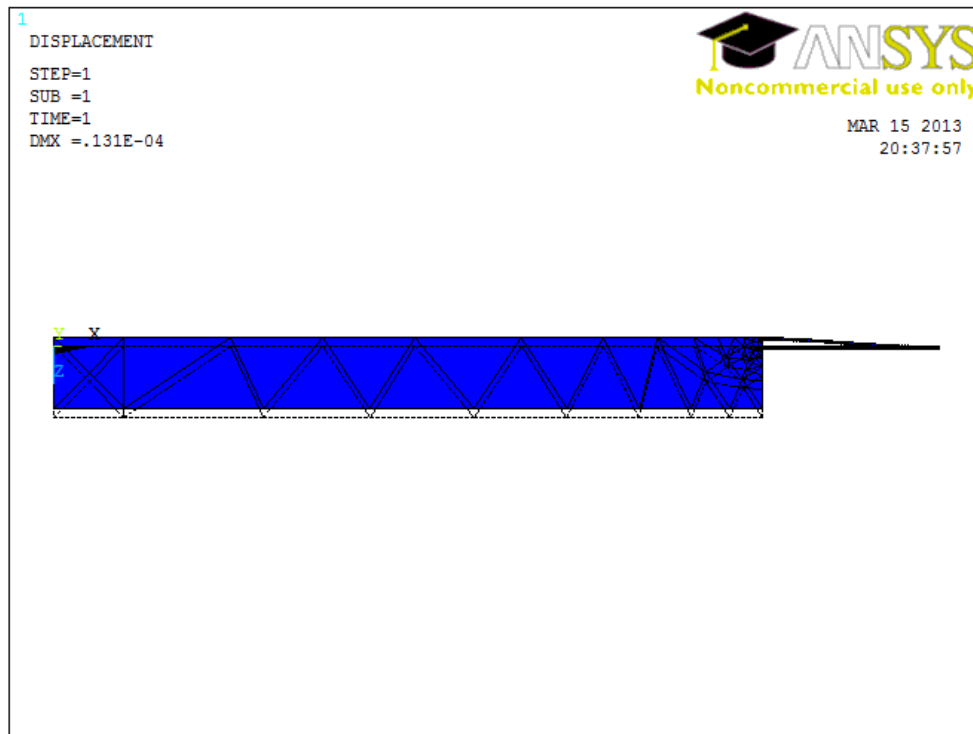
Fig. 3.5 ANSYS simulated results of deformed beam showing a nonlinear behavior like a stretching string
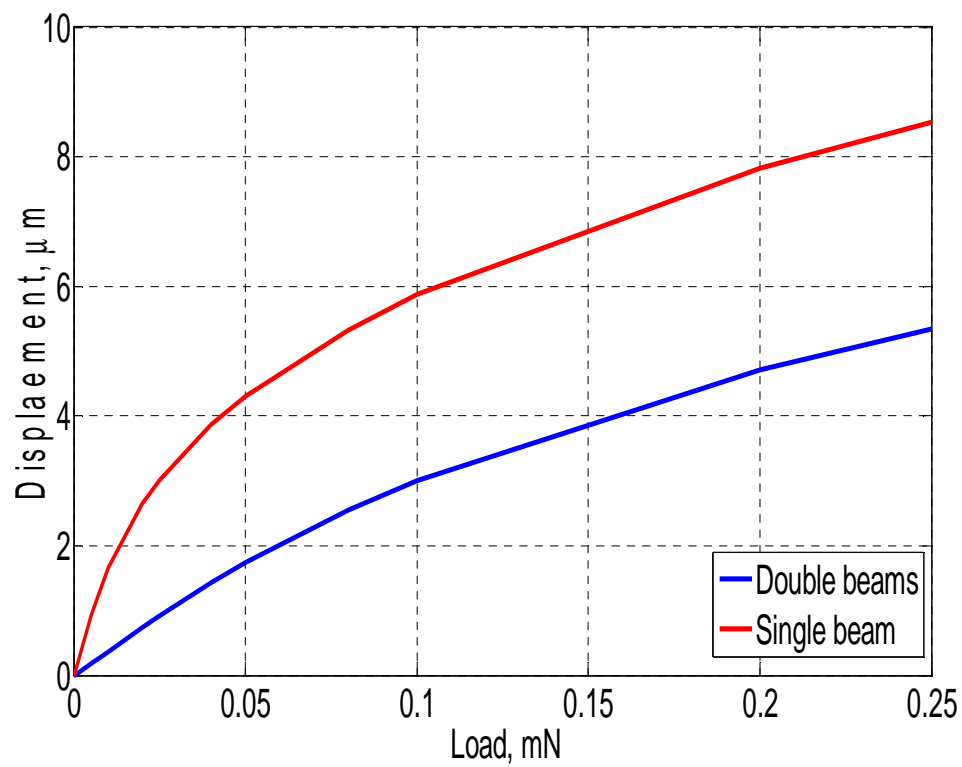
Fig. 3.6 ANSYS simulated results of displacement vs. force of the suspended structures

3.2 Mask Design

In order to optimize the flexure design, a series of test beams with different lengths and shapes were designed and microfabricated, see Fig. 3.7. Fig. 3.7 (a) is the back side mask. The five CFA top platen elements are 2 mm square in the center and the gap width is about 20 μm considering the isotropic etching property of XeF_2 and the wafer thickness. Two group marks near the edge are for the double side alignment in the later steps. Fig. 3.7 (b) is the mask for contact pads on the top side of a wafer. Fig. 3.7 (c) is the top side mask. Fig. 3.7 (d-h) illustrate various flexure designs.
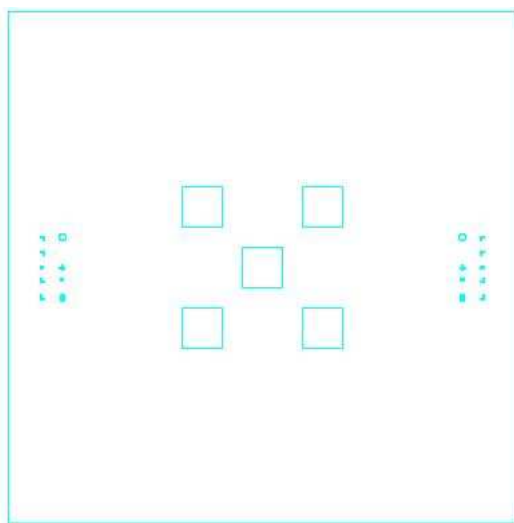
(a) The mask for a CFA top platen   (b) The mask for contact pads

Several patterns are shown in (d)-(h)
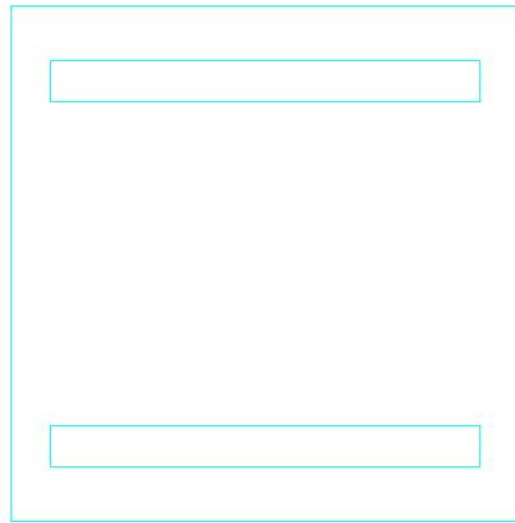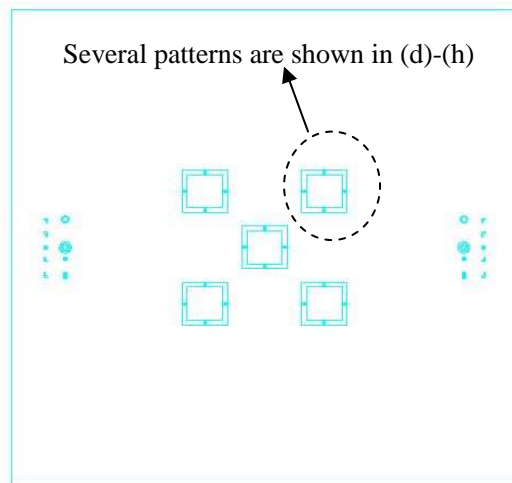
(c) The mask of the front side
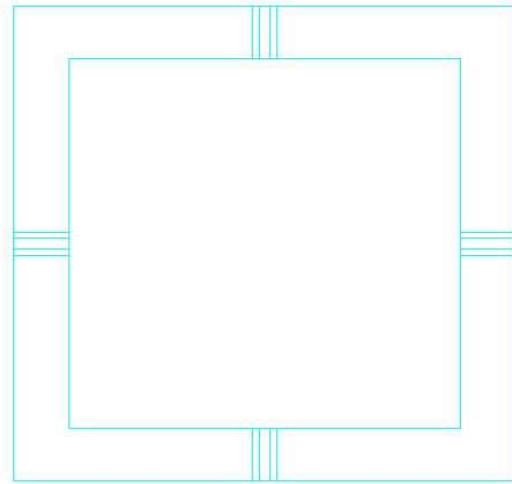
(d) Pattern 1
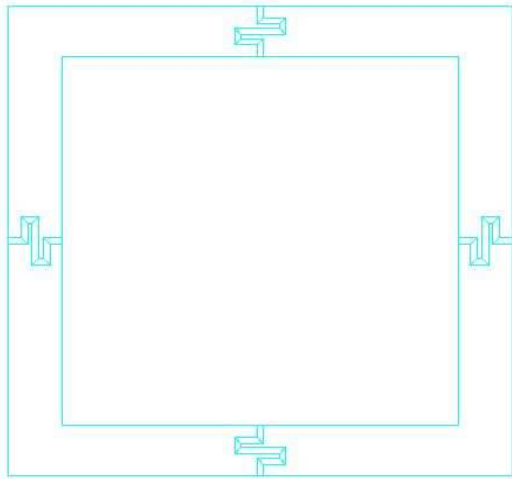
(e) Pattern 2

(f) Pattern 3

<div align="center">(g) Pattern 4   (h) Pattern 5</div>
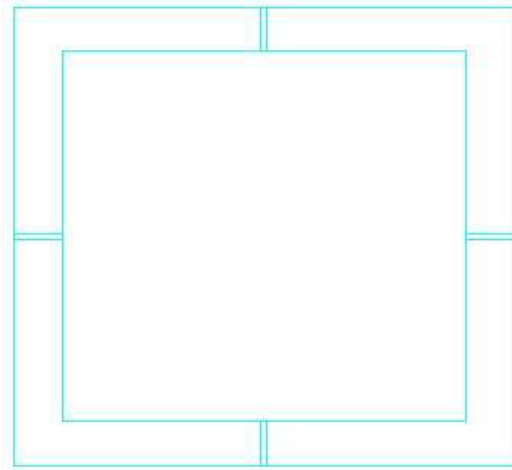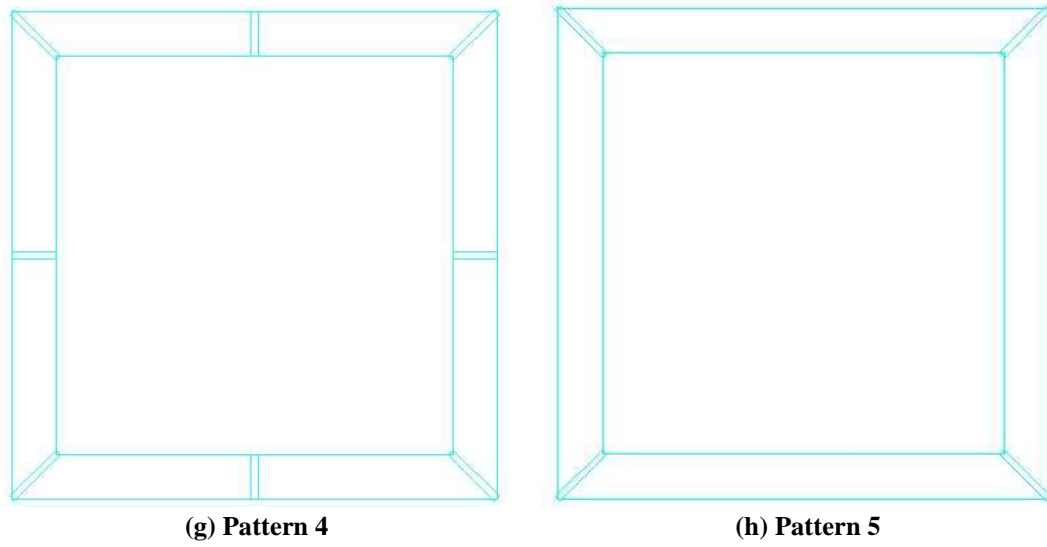
Fig. 3.7 Masks for defining the top plates of the CFA (beam dimensions in c-h: length-250 μm, width-30 μm, thickness-3 μm)

Finally we choose the design of Fig. 3.7 as it exhibited the best fabrication yield rate and mechanical behavior.

After characterizing the first generation CFA prototype, we subsequently redesigned our mask to increase the fabrication yield and achieve a larger out-of-plane displacement. Fig. 3.8 is the final mask for the second generation CFA prototype. We increased the five CFA top platen elements to nine (on the same size SOI wafer). To get a larger out-of-plane displacement, we reduce the eight beams to four at each element to make the plates more compliant. Other dimensions are the same as those in Fig. 3.7.
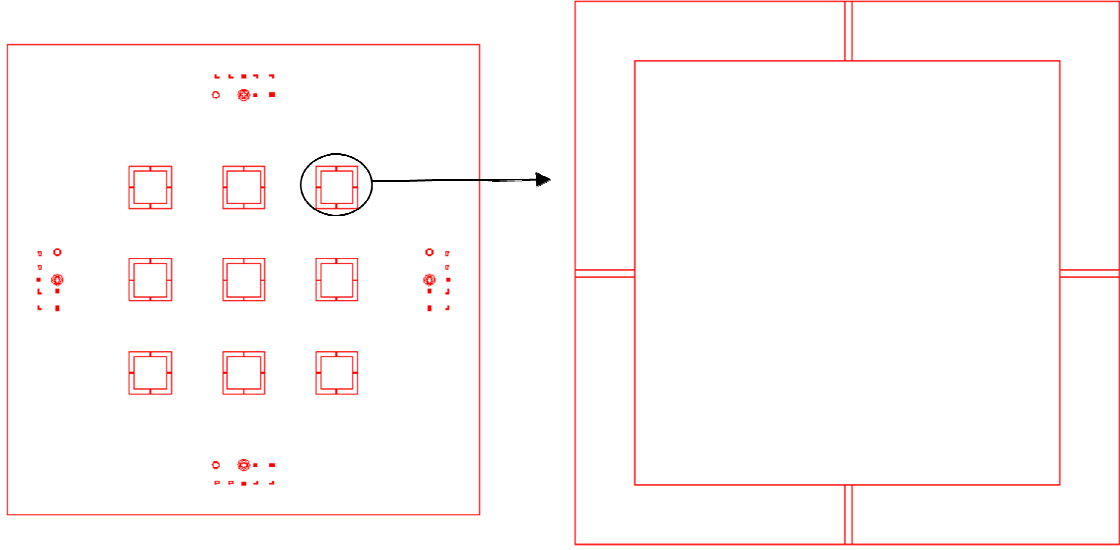
Fig. 3.8 Mask of the second generation CFA prototype of top platen (Beam dimensions: length-250 μm, width-30 μm, thickness-3 μm)

3.3 Summary

The CFA design is based on previous electrowetting test results, the design chart of Nezamoddini [33] and fabrication factors. Special efforts are given to the design of a top platen by making use of nonlinear beam theory and FEA simulation. ANSYS simulation results confirm the nonlinear relationship between the displacement and applied force. Then the design of masks for different CFA prototypes is discussed considering fabrication issues (including yield) and mechanical behaviors. The fabrication process is explored in the next chapter.

4 Fabrication

This section describes the fabrication process of the CFA prototype. The whole structure of the CFA prototype is shown in Fig. 4.1. It is a sandwich structure including two plates and a conductive liquid between these two plates. The top wafer contains the moving part is referred to as the top platen and other one is called the bottom plate. Each plate consists of a thin dielectric layer and a thin hydrophobic layer. Two plates were fabricated first and then assembled together.

| Support structure | SiO_2 | Conductive Liquid | SOI wafer | Cytop |
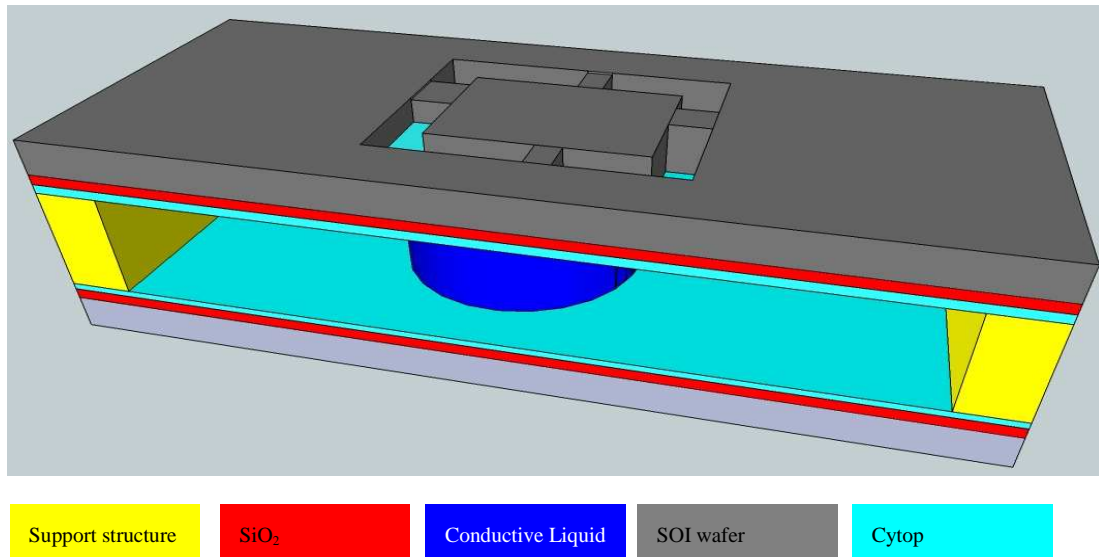
Fig. 4.1 Prototype design of the CFA

4.1 Fabrication of the Bottom Plate

A 2 inch Si wafer with p type dopants is used as the electrode. A 30 nm thick SiO_2 layer is thermally grown on Si wafers in a rapid thermal annealing (RTA) machine at 1100ºC degree for 10 mins with 100 sccm flow rate of O_2. In order to cut this 2 inch

wafer to a size small enough (5 mm square, the smaller Si wafer in Fig. 4.2) to fit the

assembly process, photoresist is spun on the Si wafer at 2000 rpm for 30 s, baked at

100ºC for 2 mins, and cut. The small wafer is rinsed with acetone, DI water, and dried

with N_2. A 30 nm thick hydrophobic layer (Cytop [59]) is then spun on the SiO_2 layer

at 2000 rpm for 30 s and baked at 170ºC degree for 1 hour after waiting for 5 mins at

room temperature. To obtain a good electrical contact, the native oxide layer on this Si

wafer is removed first using buffered oxide etchant (BOE). A thin Au layer is

deposited on it by electron beam evaporation. A coated wire is fixed to the Si wafer by

conductive epoxy 8331 from MG chemicals and cured at room temperature overnight.

We paint a GaIn metal liquid onto the back of the larger Si wafer and sit it onto this big

Si wafer. A final view of the bottom plate is shown in Fig. 4.2.
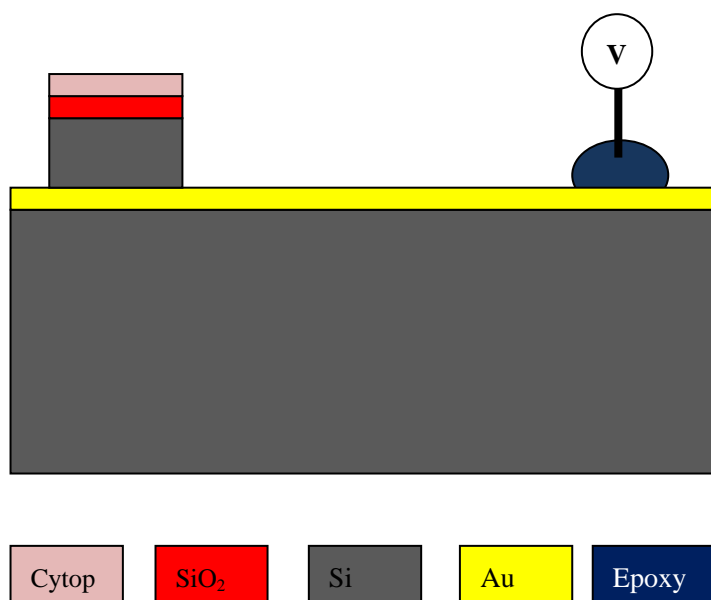
Fig. 4.2 A schematic figure of the bottom plate assembly showing method of electrical contact

4.2 Fabrication of the Top Platen

To produce a structure that is both thin and small in size, there are two major fabrication approaches—bulk and surface fabrication. Considering our clean room capabilities, we decided to use a bulk method to fabricate the platen structure. A silicon-on-insulator (SOI) wafer is advantageous for this considering the accuracy of the thickness control for the flexures. Here, we start with a 3 µm thick Si layer (device layer), a 1 µm thick buried SiO_2 layer (the buried oxide layer), and a 400 µm thick Si bulk layer (handle layer). We explored both wet and dry etching techniques for performing the bulk release etch.

4.2.1 Wet Etching Method

After the mask design of the top platen, we first chose to pursue the wet etching method since it is usually a fast and easy way to etch the Si bulk. KOH (Potassium hydroxide), TMAH (Tetramethylammonium hydroxide), and EDP (Ethylenediamine pyrocatechol) are three chemical etchants for Si. However, the selectivity between SiO_2 and Si is small when using KOH etchant; EDP is corrosive; and we did not obtain consistent results using TMAH. Therefore, we turned to a dry etching approach for the bulk etch process.

4.2.2 Dry Etching Method

XeF_2 is a dry, plasma-less, and fast etchant for Si etching. However, it is an isotropic etchant so we need to parameterize the etch rate of Si in XeF_2. In order to get a beam with a length of 250 µm, we need to lap the back side of the SOI wafer to an

optimized thickness taking into consideration the isotropic property of XeF_2 and the mask resolution limit. A series of SOI test wafers were used to parameterize the etchant rate. To optimize the etch rate, the gap width of the beam structure, and the SOI wafer thickness, several test samples with different thicknesses and gap widths patterns were etched in XeF_2. We finally converged to a process employing a 100 μm thick SOI wafer with a 30 μm wide initial gap.

A reproducible fabrication process of the top platen along with the optimized etch rate and thickness is shown in Fig. 4.3. Fig. 4.3 (a) is a color guide for different materials used in the whole fabrication flow. Fig. 4.3 (b-l) only show major steps of the fabrication process. Detailed fabrication recipes are described in Appendix B.

| Si | SiO_2 | Photoresist |
| Al | Cytop | Wax | Glass slide |

(a)

30 nm SiO_2

3 μm Si

1 μm SiO_2

400 μm Si

(b) Thermal growth of SiO₂ on SOI wafer
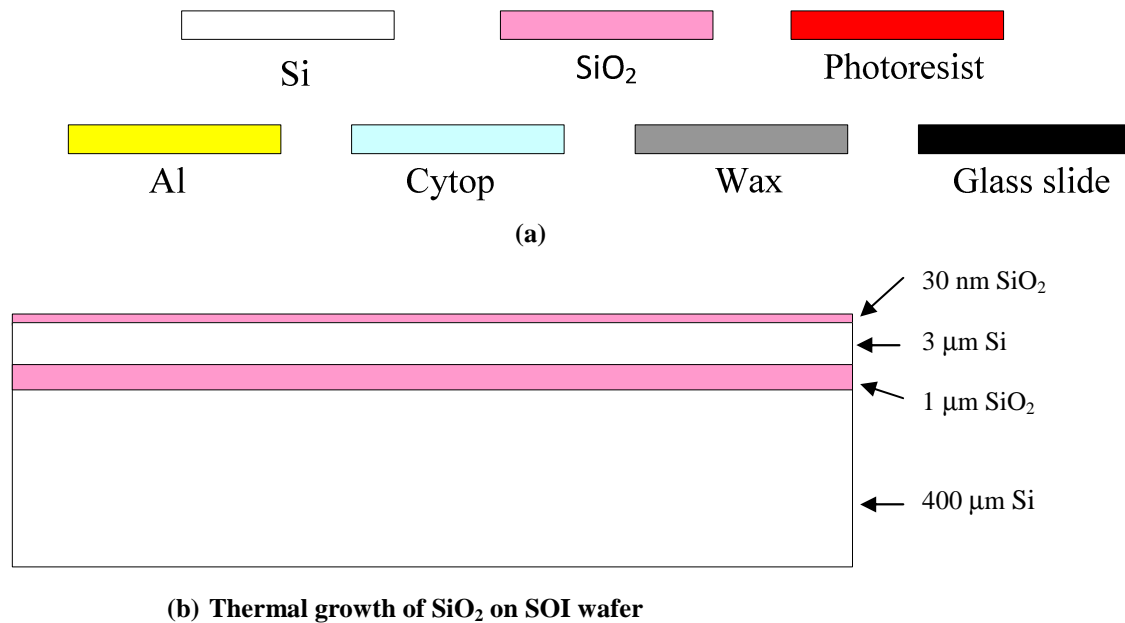
The SOI wafer is put into the rapid thermal annealing machine and heated at 1100ºC for 10 mins with 100 sccm flow rate of O_2. The SiO_2 is thermally grown on the SOI wafer.

43

Glass
Photoresist
30 nm SiO_2
3 µm Si
1 µm SiO_2
100 µm Si

(c) Lap Si substrate to 100 µm
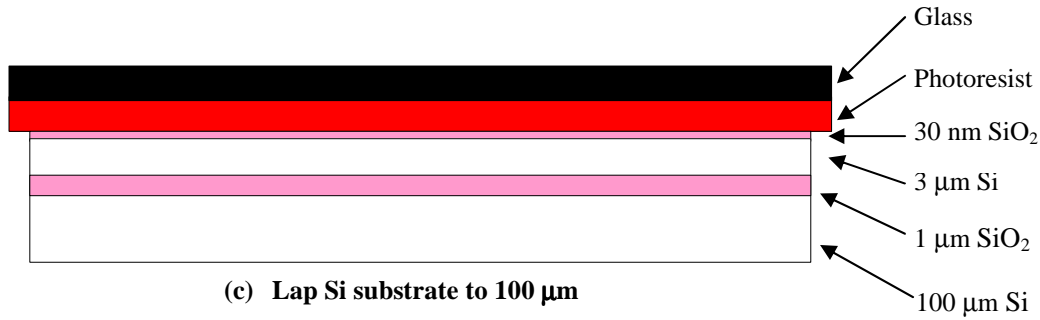
The SOI wafer is then cut to a 1inch square and fixed to the lapping glass substrate (with the device layer facing down). The thick SOI bulk layer is then lapped to 100 µm thick. The reason we want to lap the SOI wafer is that the isotropic etching property of the XeF_2 in a later step must be considered.

30 nm SiO_2
3 µm Si
1 µm SiO_2
100 µm Si
200 nm Al

(d) Backside Al deposition

After the SOI wafer is lapped to 100 µm thick, the wafers are released from the glass substrate. A 200 nm thick Al layer is deposited on the back side of the SOI wafer using electron beam evaporation equipment.

100 nm Al

Photoresist

30 nm SiO$_2$

3 μm Si

1 μm SiO$_2$

100 μm Si

200 nm Al

Photoresist

Glass

(e) Contact patterning, deposit Al
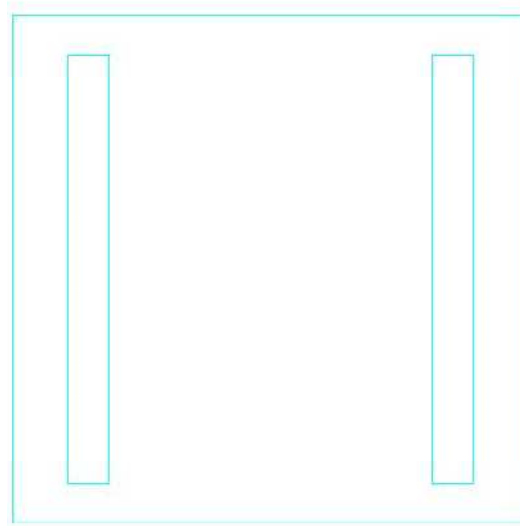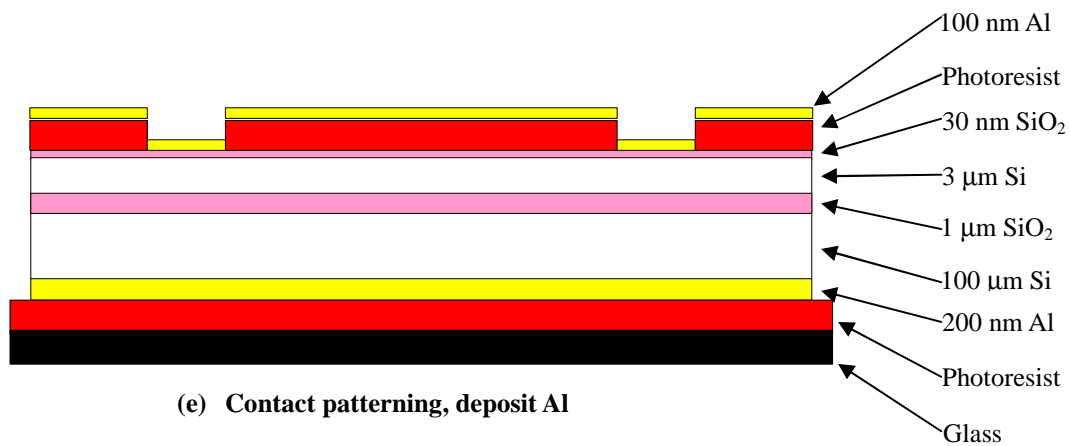
(e2) Contact patterning mask for step (e)

With the SOI wafer fixed to the glass substrate for ease of handling, the top side of the SOI wafer is patterned using photolithography. The SiO$_2$ is etched in BOE and rinsed in DI water before a 200 nm thick Al layer is deposited on the top side.

100 nm Al

30 nm SiO$_2$

3 μm Si

1 μm SiO$_2$

100 μm Si

200 nm Al
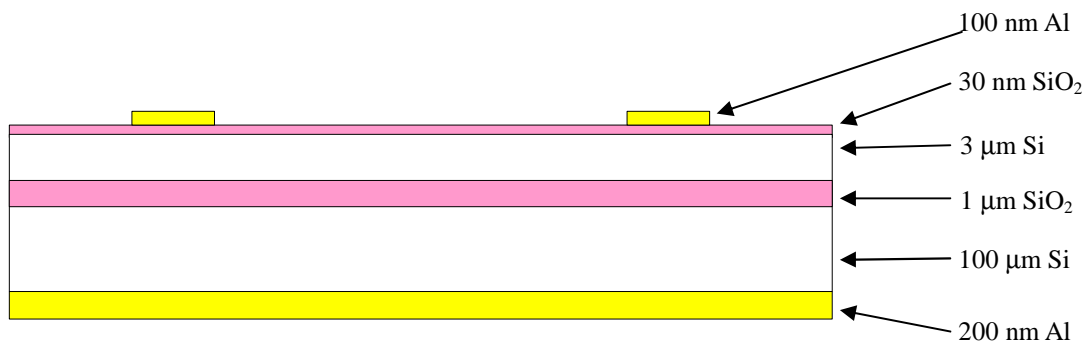
(f) The top view of the Al liftoff

The contact pads are patterned on the top side of the SOI wafer by the lift off photolithography in heated N-Methyl-2-pyrrolidone (NMP).

Glass

Photoresist

30 nm SiO$_2$

3 μm Si

1 μm SiO$_2$

100 μm Si

200 nm Al

Photoresist
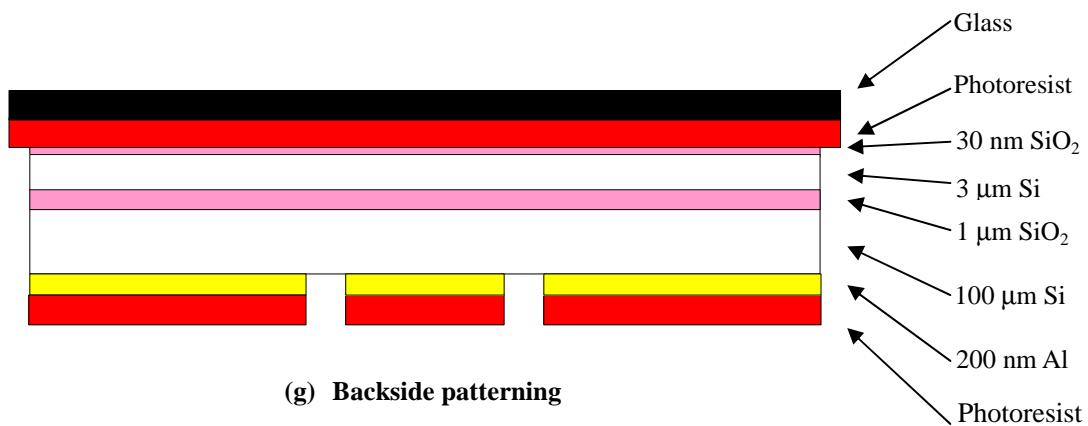
(g) Backside patterning
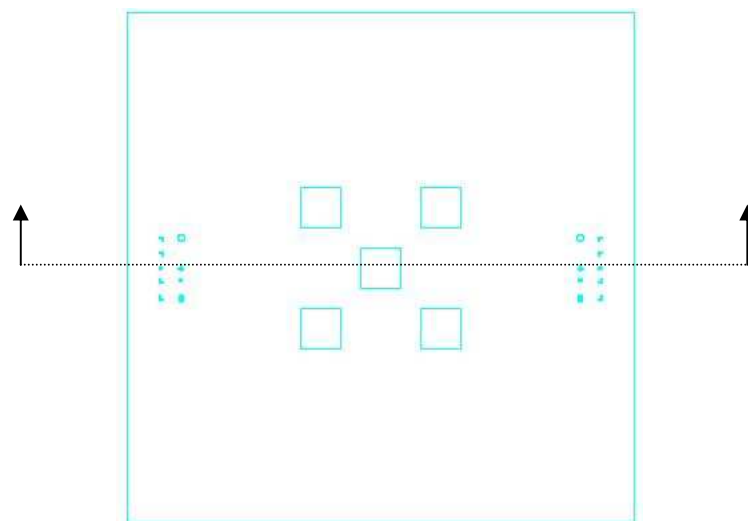
(g2) The mask for backside patterning

46

The back side of the SOI wafer is patterned by photolithography after the SOI wafer is fixed to a glass slide. Then the Al layer is wet etched in a commercial Al type D etchant. The Al layer here defines marks as marks that are used for double sided alignment.

(h) Backside XeF2 etch through Si substrate
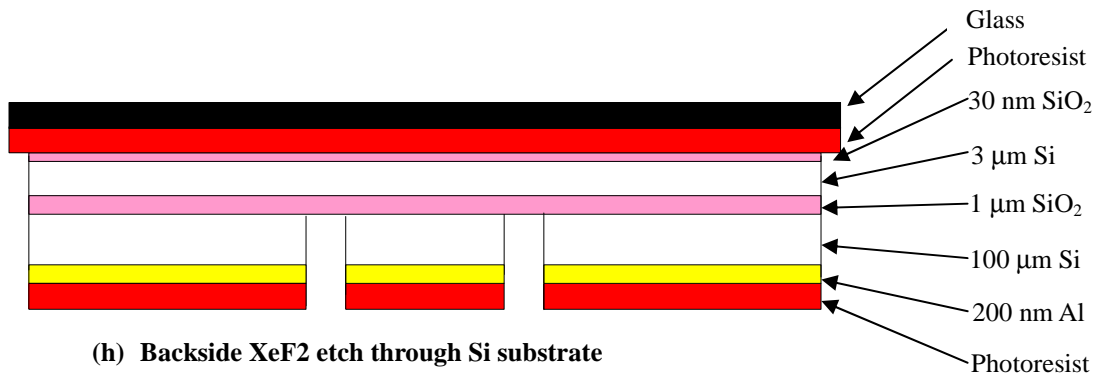
Just before we put the SOI wafer in the XeF_2, the wafer except the 5 or 9 elements in the middle part is protected by a HF resistant tape. The wafer is etched with 20 cycles (each cycle takes 1 minute).
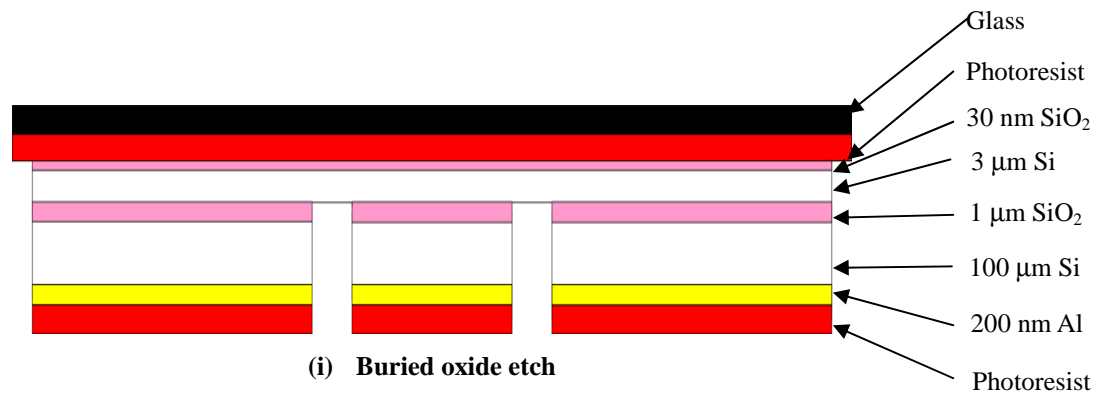
(i) Buried oxide etch

The SOI wafer is dipped in BOE for one hour to remove the 1 µm thick buried oxide layer. Then the tape is removed in acetone and heated NMP.

47

Photoresist
30 nm Si
3 µm Si
1 µm SiO₂
100 µm Si
200 nm Al
Photoresist
Glass

(j) Electrode/suspension pattern definition

(j2) Mask for electrode/suspension pattern definition
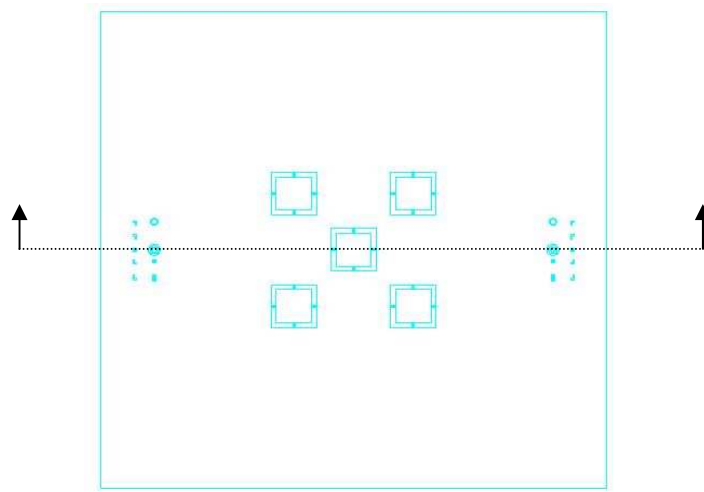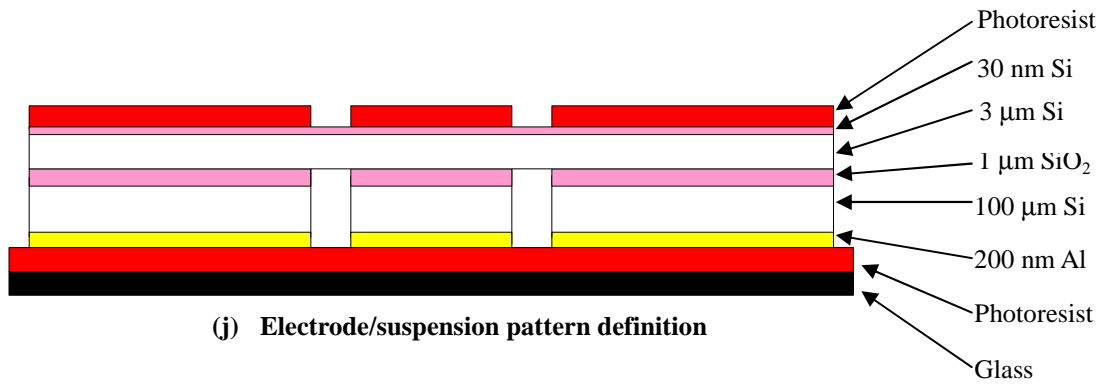
The top side of the SOI wafer is again patterned using the EVG 620 double side aligner. The thermal of SiO₂ is etched using BOE.

Photoresist
30nm SiO₂
3 µm Si
1 µm SiO₂
100 µm Si
200 nm Al
Photoresist
Glass

(k) Etch Si layer in SF₆
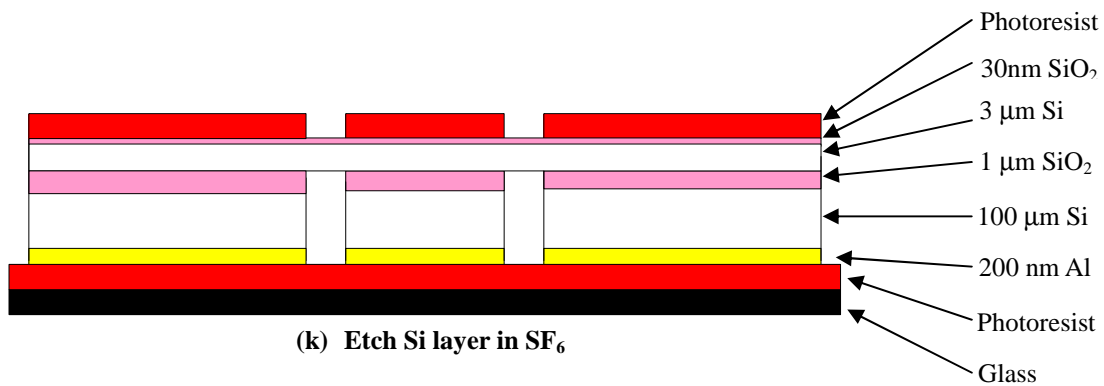
The silicon device layer is etched in a SF₆ plasma to produce the final structure.

48

Cytop
30 nm SiO$_2$
3 µm Si
1 µm SiO$_2$
100 µm Si
200 nm Al

(l) Spin hydrophobic Cytop film
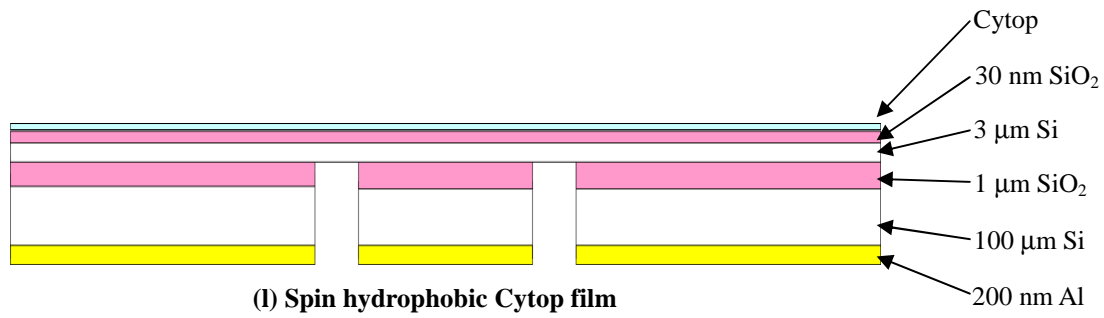
Fig. 4.3 Fabrication process of the top platen

After the SOI is released in heated NMP, the hydrophobic Cytop layer is spun at 1000 rpm for 30 s on the top side of the SOI wafer and baked at 160ºC for 30 minutes.

A scanning electron microscopy (SEM) view of the top platen is shown in Fig.4.4. We firstly began with an eight-beam structure to demonstrate the functionality of a CFA, see Fig. 4.4 (a). Then, we redesigned our top platen with a four-beam structure to increase the out of plane displacement, Fig. 4.4 (b).

(a)
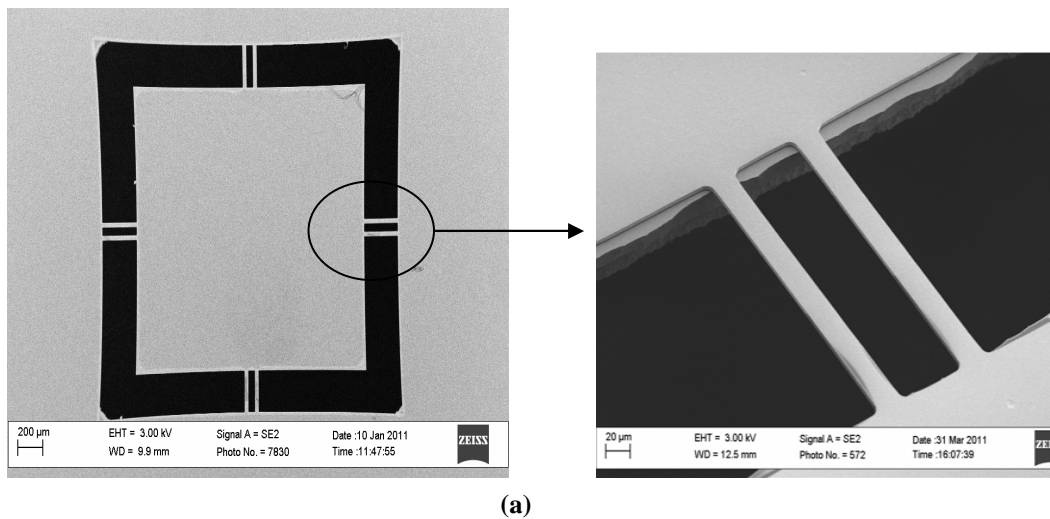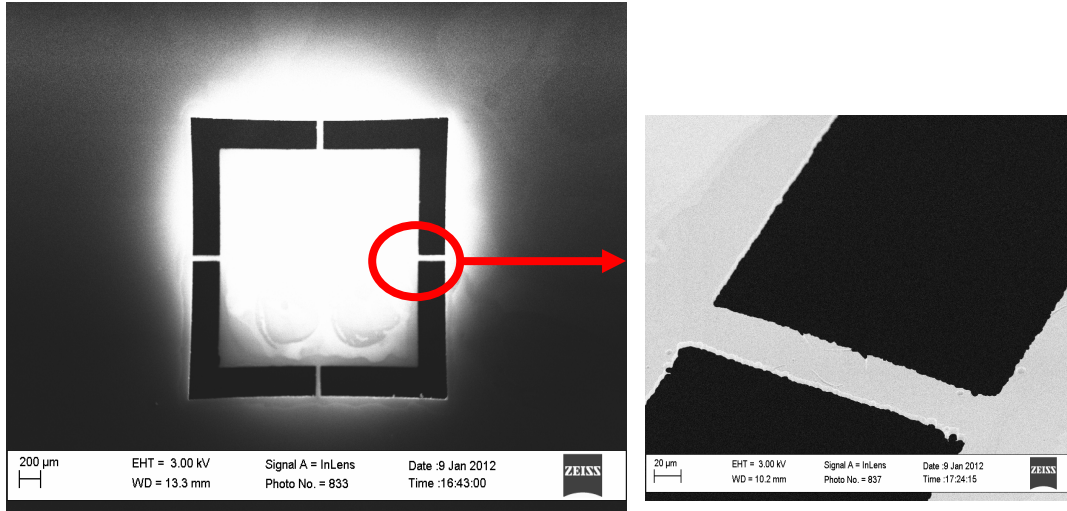
(b)

Fig. 4.4 Scanning Electron Microscopy (SEM) images of the true top moving platen (a) The first generation prototype of a CFA top platen. (b) the second generation prototype of a CFA top platen

4.3 Assembly Processes

4.3.1 Evaporation Tests

Before we assembled the top and bottom plates, we performed evaporation tests to optimize the ratio of electrolyte to propylene glycol. Using comparable volumes of different liquids on the same bottom plate, under the same environment conditions, the results (Fig. 4.5) show that the drop evaporates more rapidly with lower concentration of PG. Though the DI : PG=1 : 2 solution has the slowest evaporation rate. Instead, we chose a 0.05 M Na_2SO_4 1:1 DI-PG volume ratio for use in subsequent experiments since both the evaporation rate and its droplet conductivity must be considered.
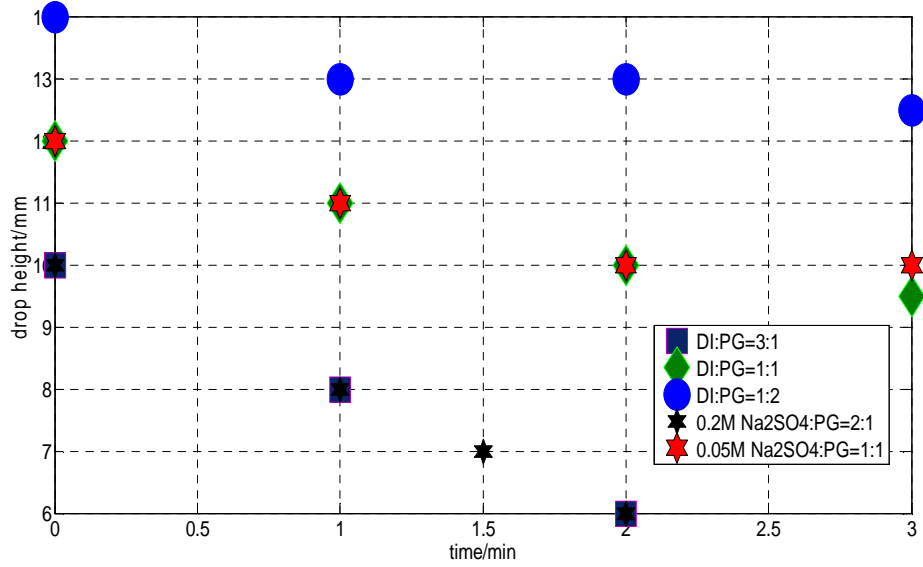
Fig. 4.5 Evaporation tests of various conductive liquids

4.3.2 The Top Platen Assembly Process

The final prototype is illustrated in Fig. 4.6. After the fabrication of the top moving platen, the SOI wafer is fixed to a PDMS (Polydimethylsiloxane) layer on an Acrylic plate using super glue. A cold curing conductive epoxy is bladed on a 25 µm thick Al foil by using two 25 µm thick Kapton films as spacers. The end with the bladed conductive epoxy on the Al foil is stuck to the Al contact pad. The other end of the Al foil is anchored to the Acrylic plate using super glue. A length of coated wire is fixed to the top side of the Al foil with conductive epoxy.

After the successful fabrication and characterization of the first generation prototype of the CFA top platen, we modified the assembly process to provide greater protection to the fragile platen wafer during assembly. Three small pieces of foam replaced the PDMS layer to act as a flexible support. This allows the spacers to set the alignment between the platen and the stationary wafers without the development of

51

stress concentrations at points of contact, Fig. 4.7. We used both plastic micro-beads (diameter 100 µm) and lapped wafers as spacers; the former has the advantage of being more robust to any curvature of the top platen.
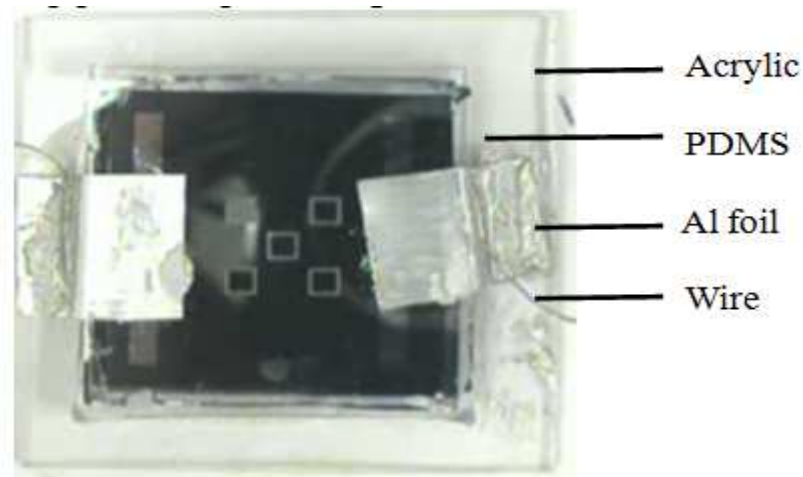
Fig.4.6 The top platen after assembling contact pads
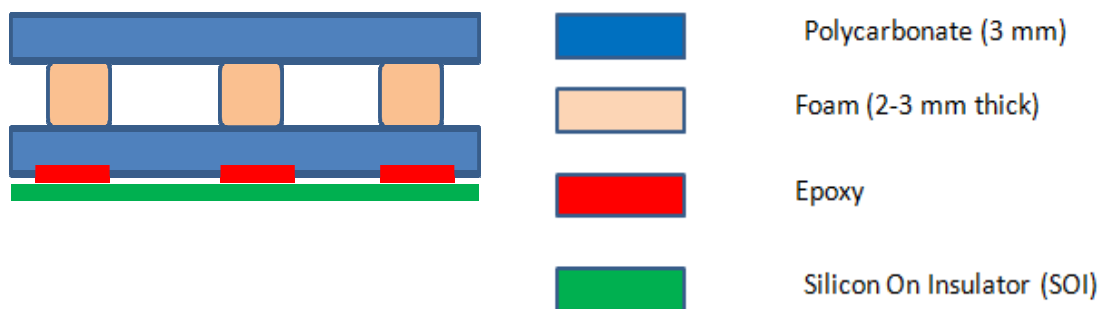
Fig. 4.7 Schematic figure of the second generation CFA prototype fixed into a piece of Polycarbonate

4.3.3 The CFA Device Assembly Process

We use a "flip chip" method to assemble the top platen and bottom wafers together to form a completed actuator, see Fig. 4.8. The top and bottom wafers are aligned using a microscope and linear translation stages. First, the liquid drop is

deposited on the bottom plate using a micropipette (0.1 µL to 0.5 µL). The top platen wafer is then positioned close to the bottom plate and the platen square is aligned with the drop. Finally, the bottom plate is moved up using the microscope fine focus knob so that the sessile drop contacts the platen square to form the liquid bridge. The entire process is recorded by a side view camera attached to the second microscope. A frame from this view is shown in Fig. 4.9 to illustrate the assembly steps. During the assembly process, we can tell the focus image to make sure the completion of the assemble process. Several different types of spacers were used during this research. For early tests, 100 mm insulated wafers were used to control the distance between top and bottom wafers. Later, 100 mm polystyrene microbeads were used. These were deposited in solution via micropipette on either the top or bottom wafer. We found ultimately that this was achieved more successfully in the following manner, see Fig. 4.10. On the bottom plate, we patterned photoresist (green in Fig. 4.10) to form "landing zones" for the beads. We then dispensed the beads (black in Fig. 4.10) on the zones to act as spacers. The photoresist provides protection to avoid scratching the hydrophobic and dielectric layers during the process of dispensing beads, and thereby creating an electrical path.
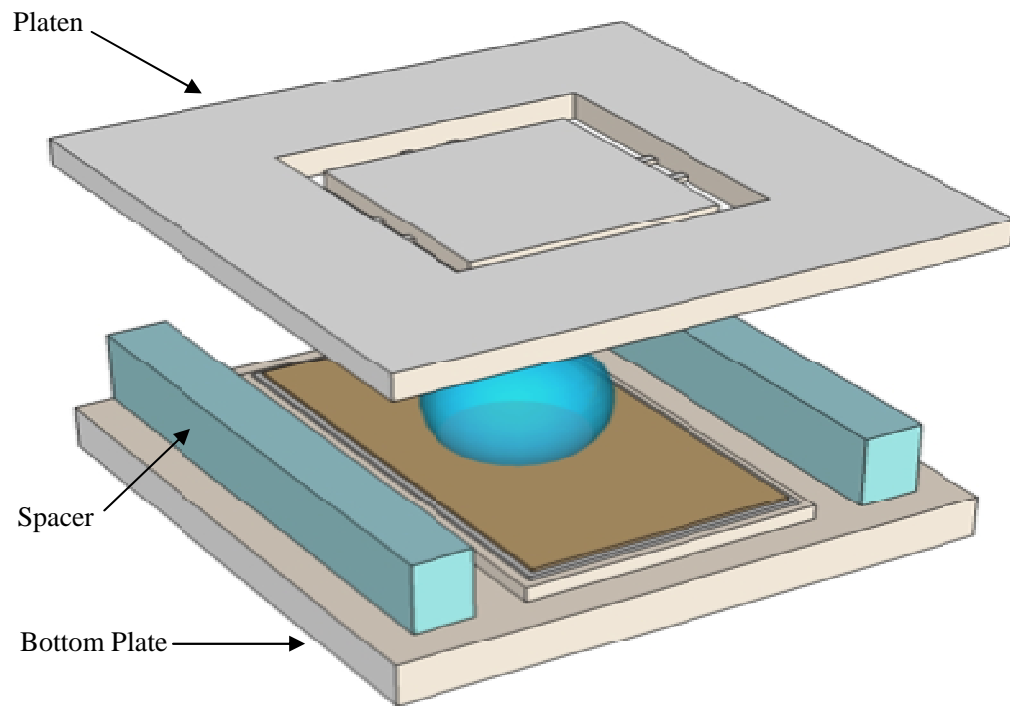
Fig. 4.8 A schematic picture of the flip chip assembly process
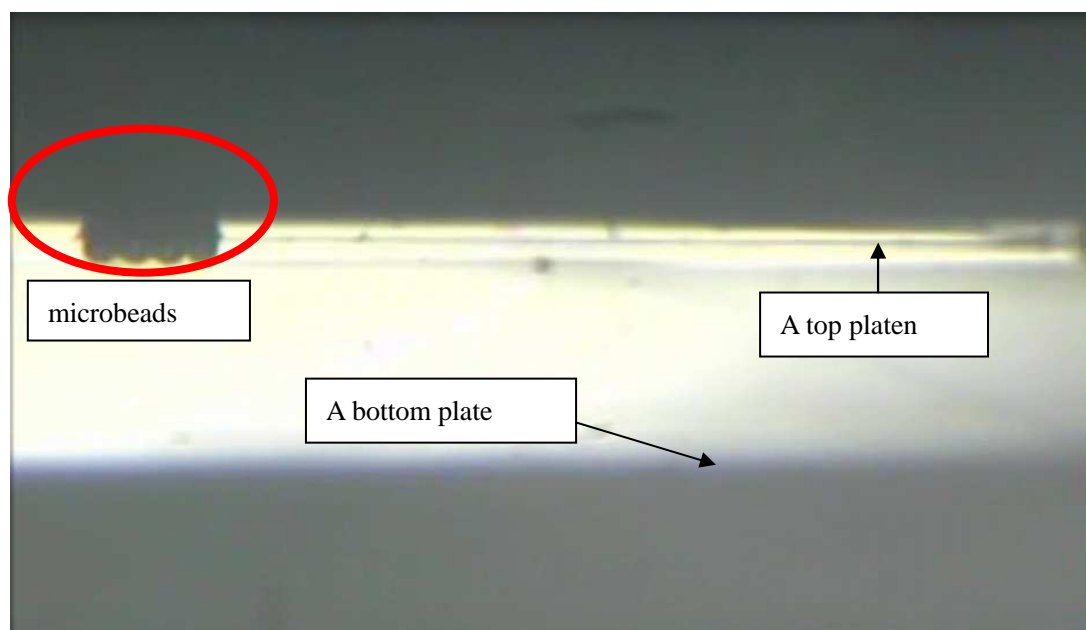
Fig. 4.9 A video frame of the assembly process
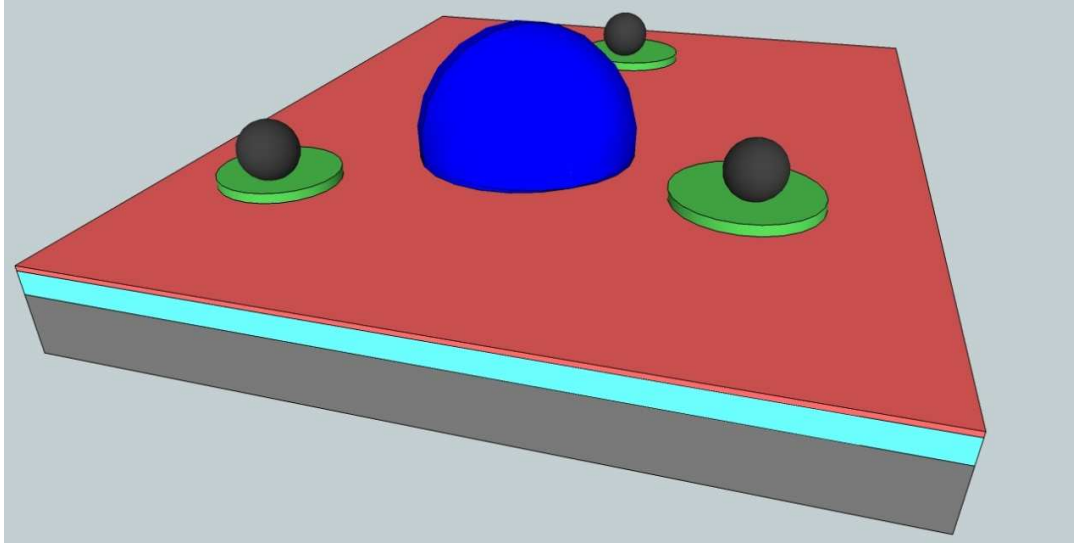
Fig. 4.10 Final method for dispensing microbeads on a bottom plate, photoresist landing zone shown in green

4.4 Summary

This chapter describes the fabrication process of a CFA prototype, consisting of a bottom fixed wafer and a top moving platen wafer. The fabrication of the top platen wafer is based on bulk microfabrication technology. The parameters of several major steps were characterized so that the fabrication process is reproducible. Finally, the flip chip assembly process of a CFA prototype is described.

5 Characterization of CFA Prototypes

Following the fabrication of CFA prototypes, we characterized their performance, in particular the displacement as a function of voltage, and the generated force. In this chapter, we describe the displacement measurement system and discuss how the force can be inferred from the mechanical behavior.

5.1 Characterization Systems

5.1.1 Displacement Measurement System

We considered a number of approaches to measuring the CFA displacement, including contact methods, capacitive sensing, and optical techniques. After considering the available laboratory equipment and facilities, we chose a non-contact, optical method to measure the displacement.

A test platform for measuring the displacement of the CFA prototype was set up as, shown in Fig. 5.1. This system consists of an Olympus BHM microscope with a Panasonic GPKR222 camera, linear translation stages, an HP3631A power supply and a Fluke 45 multimeter. Labview software is used to simultaneously control the voltage level and monitor the leakage current. Displacement was monitored using a fiber optic reflectometer from Luna Innovations, Inc., operated as an extrinsic Fabry-Perot interferometer.
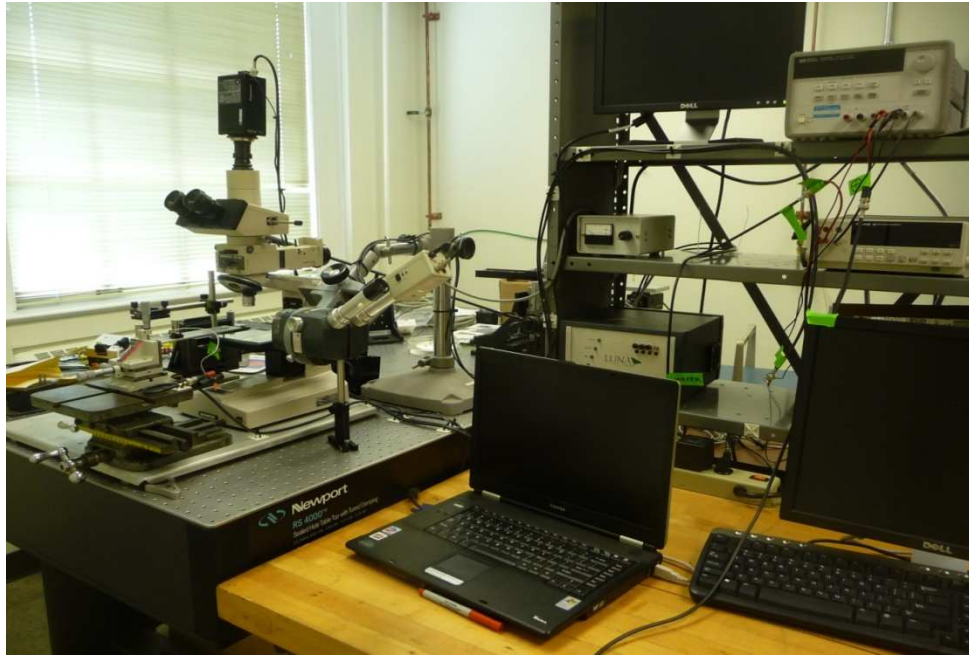
Fig. 5.1 The static displacement measurement platform, version 1.

After obtaining initial results, we encountered a number of experimental issues which needed to be addressed. These included a need for flexible multi-axis stage control, a stable but adjustable fixture to position the optical fiber, improved sample illumination, and an additional camera to record the liquid bridge from the side. Considering these factors, we set up an improved displacement measurement system, illustrated in Fig. 5.2. The improved setup includes a goniometer stage for the CFA bottom plate, and a new side view camera. The goniometer is used to maintain parallel alignment of the top and bottom plates during assembly. The side view camera and associated optics provide a way to record the liquid drop bridge during alignment and actuation.
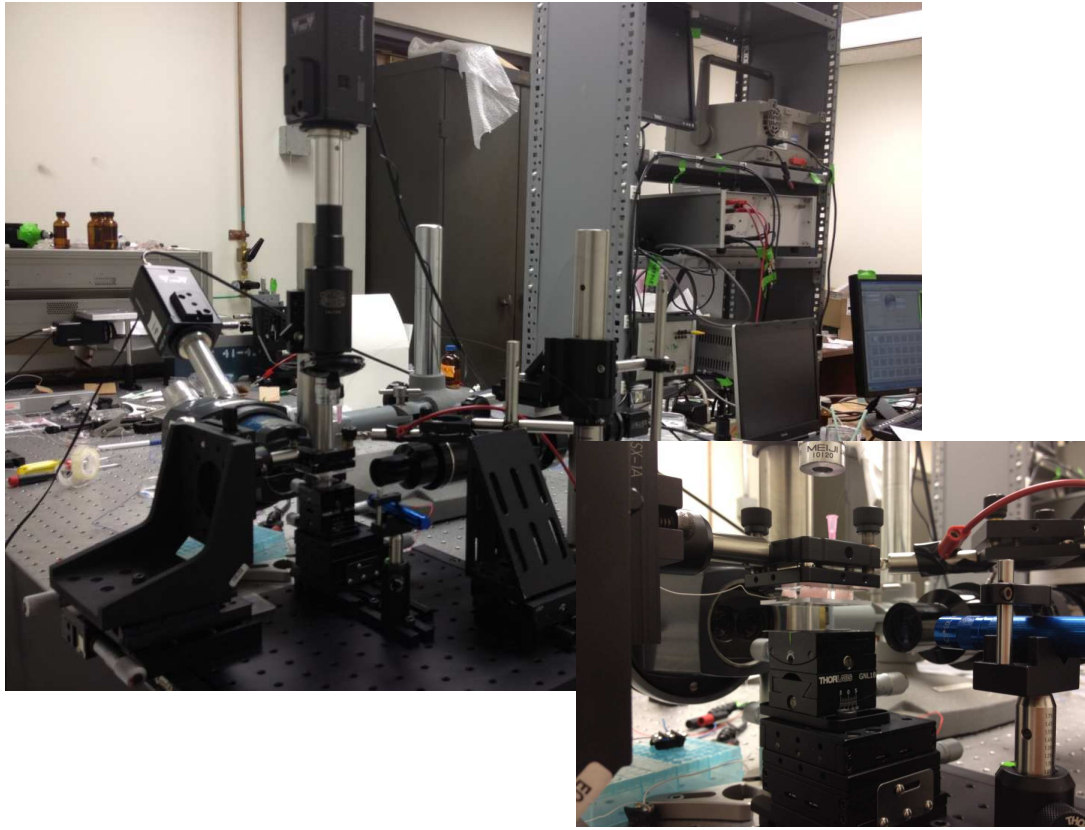
Fig. 5.2 The static displacement measurement platform, version 2.

5.1.2 Force Measurement System

After the fabrication of the top platen, we characterized the nonlinear force/displacement behavior using a specialized instrument. The mechanical properties of the top platen were measured using an MTS Instruments nanoindenter with a dynamic contact module (DCM II) and a Berkovich diamond tip. These measurements made use of the nanoindenter instrument in Prof. Matthew Begley's laboratory. (We acknowlede the assistance of Prof. Begley and John Gaskins for access to and use of the MTS machine.) From combining the experimental measurements of displacement with the nanoindenter characterization, the force produced by the CFA can be estimated from the measured displacement of the top platen.

5.2 Displacement Measurement Results and Analysis

5.2.1 Static Displacement Measurement Results and Analysis

For the static performance of the CFA, we are interested in the displacements at different DC signal levels. In these tests we used a range of 0-40 V.; this was based on the results of our previous electrowetting experiments. The static displacement was tested with both the first and second generation prototypes of the CFA; these differed in having eight or four support flexures on the top platen, respectively, but were otherwise identical.

After the assembly of a top platen and a bottom plate, tests were done twice without separating the top and bottom plates. Each test was done by scanning the voltage from 0 to 40 V and back to 0 V with a step of 2 V. Each voltage level was maintained for 3 s. Typical results are illustrated in Fig. 5.3 to Fig. 5.5.
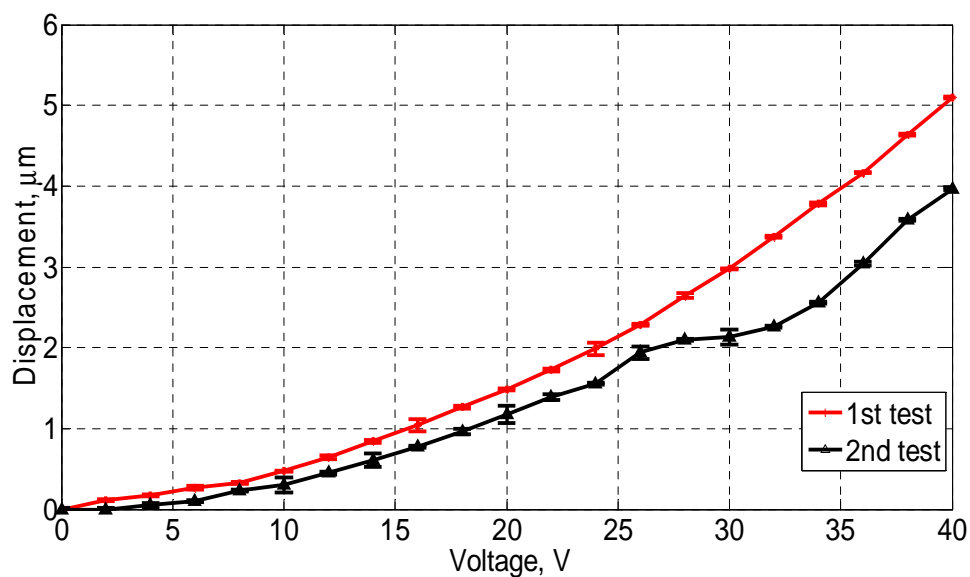
Fig. 5.3 The static displacement vs. voltage (The first generation prototype of CFA, the test was done on the same assembly)
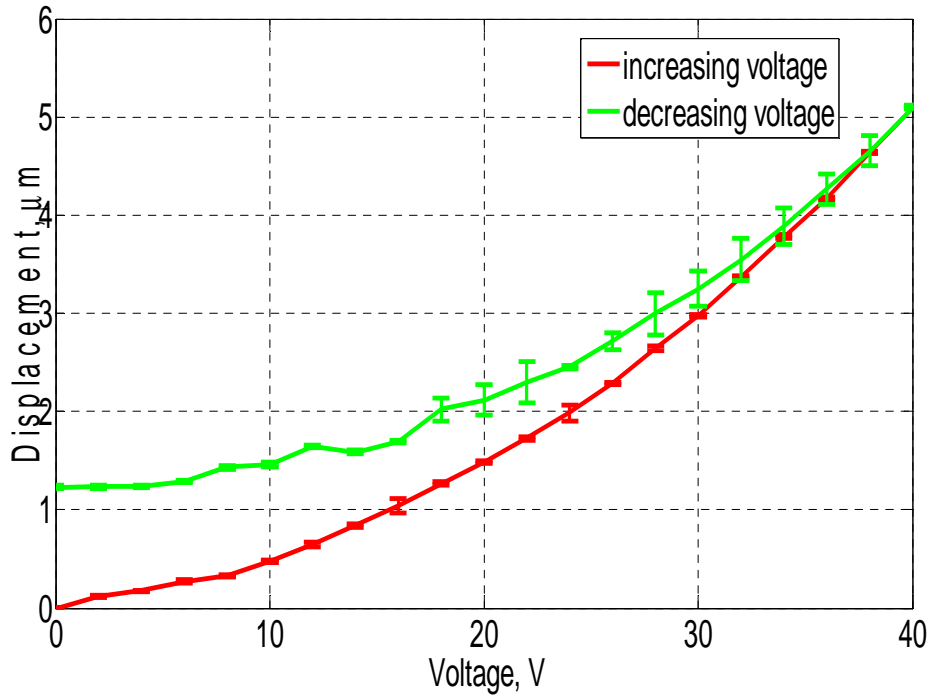
Fig. 5.4 The static displacement vs. voltage (increasing voltage and decreasing voltage, 1st test)
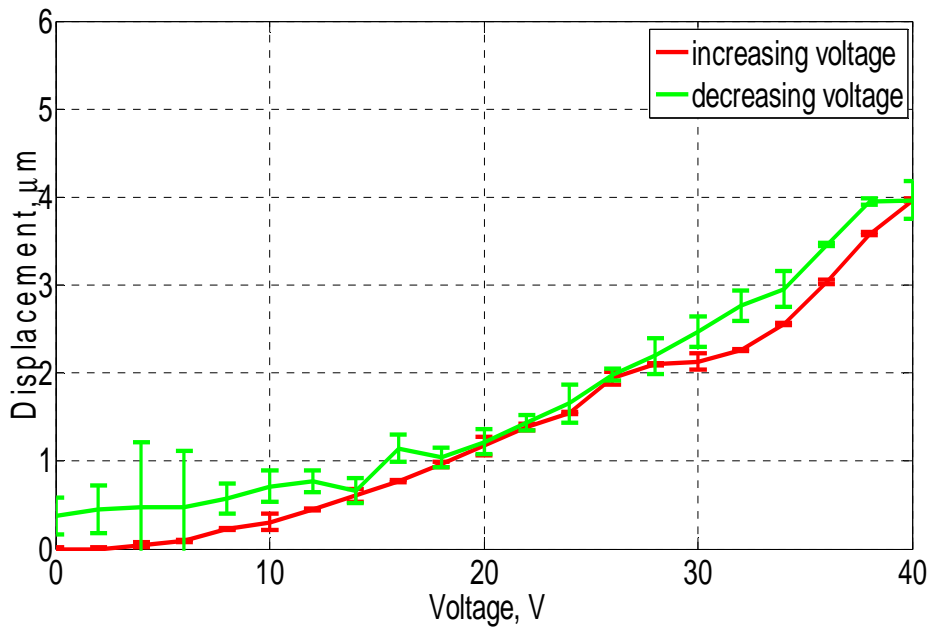
Fig. 5.5 The static displacement vs. voltage (increasing voltage and decreasing voltage, 2nd test)

Fig. 5.3 shows the maximum out of plane displacement is about 5 μm when a 40

V potential exists between two plates during the first test. The maximum displacement

of the second test done with the same assembly is about 4 μm when the same 40 V potential is applied. The reason for the difference may be due to the contact angle hysteresis such as that shown in Fig. 5.4, or a 'soft' breakdown of the dielectric layer. (By 'soft' we mean a low leakage current which cannot be measured by the Fluke 45 multimeter, which has a resolution of about 100 μA.) Fig. 5.4 and 5.5 show how the out-of-plane displacement changes when the voltage increases from 0 to 40 V and then back to 0 V. The difference between 0 volt displacements before and after the test is about 1.2 μm in the first test (Fig. 5.4) and the 0.5 μm in the second test (Fig. 5.5). This behavior may be due to the contact angle hysteresis of the hydrophobic layers, trapped charge, and/or evaporation. This trapped charge phenomenon has been seen in electrowetting experiments by other researchers [51].

Tests were also done by using the same top platen but different bottom plate samples. The applied voltage signals were the same as before. Results of such tests are shown in Figs. 5.6 and 5.7.
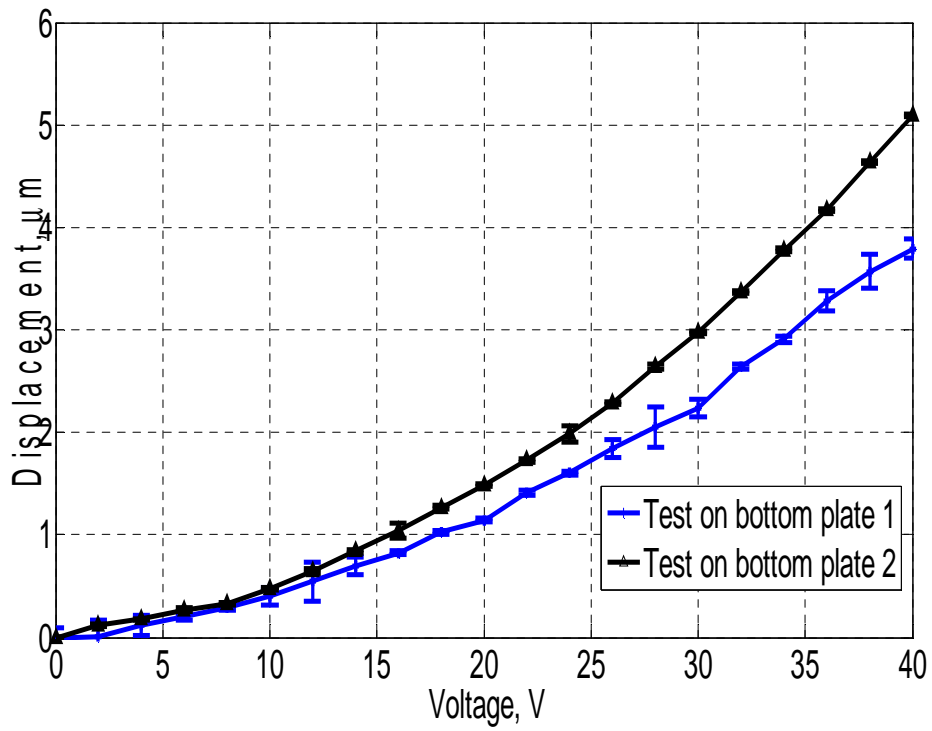
Fig. 5.6 The static displacement vs. voltage (The first generation prototype of CFA, the test was done on a different bottom plate)
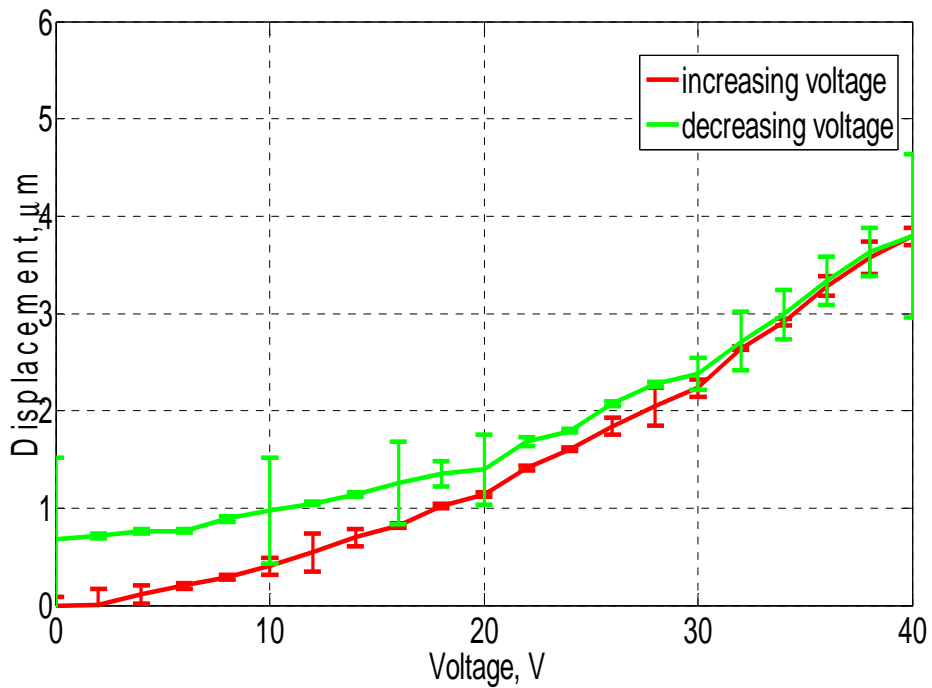
Fig. 5.7 The static displacement vs. voltage (increasing voltage and decreasing voltage)

From Fig. 5.6, we can see that the maximum displacement is about 3.8 μm when

40 V potential exists between two plates. The difference between the displacements is due to two factors. One source is the inability to precisely control drop volume and gap from one assembly process to the next. A second factor causing differences is changes to the top platen during the first test. Such changes are indicated in Fig. 5.7 which shows the hysteresis of displacement is about 0.7 μm when the voltage increases from 0 to 40 V and then back to 0 V.

In these tests, the uncertainty represented by the error bars on the graphs is calculated based on the standard deviation of displacement at each voltage level for the 3 s duration. The deviation is probably due to environmental factors like temperature change and air flow in the lab, along with quality of the interference pattern obtained from the platen.

Fig. 5.8 is a displacement result of first generation prototype of a CFA compared with that of a semi-analytical model. The CFA force in the semi analytical model is calculated based on the contact angle observed during electrowetting tests. The displacement is then determined from the force using the displacement-force relationship obtained from the nanoindenter experiments. The only unknown variable that is used to adjust the fit of the model is the droplet volume.
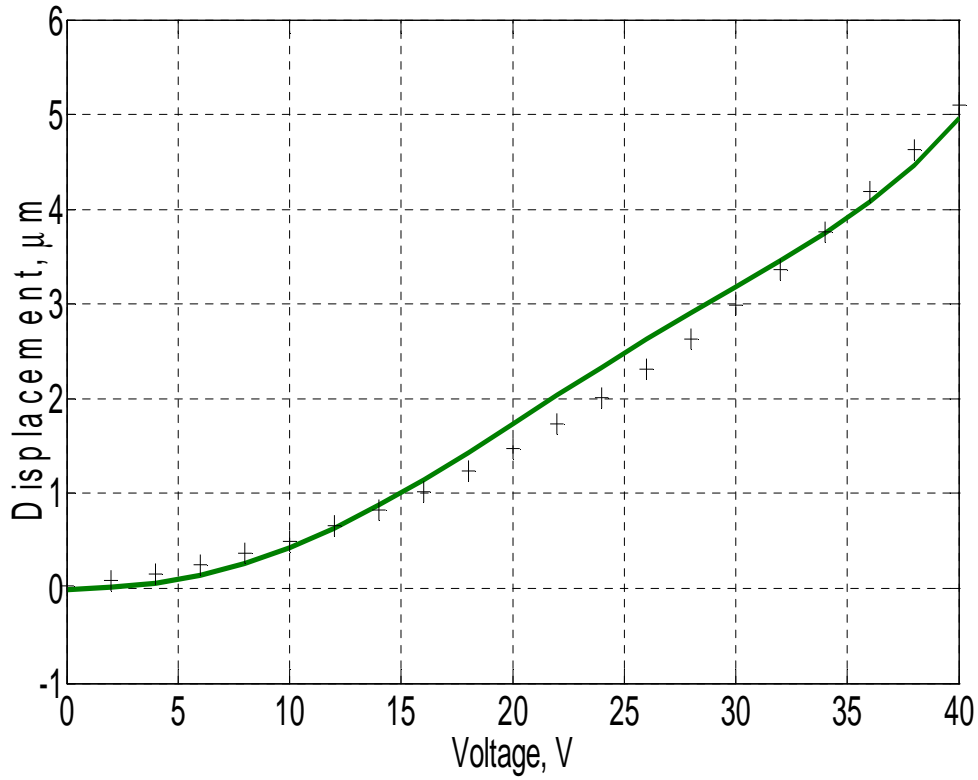
Fig. 5.8 Static displacement vs. voltage of the first generation CFA prototype. Black crosses are experimental results; the green curve represents the semi-analytic theoretical result.

The maximum displacement of about 5 μm at 40 V is considerably larger than that obtained with a comparably sized electrostatic actuator operating at the same gap: 0.4 μm at 40 V. The reason is the force produced by a CFA is much larger than that of a similarly size electrostatic actuator, as described in Eqn. 1.3 in Chapter 1.

To achieve an even larger displacement, we changed the structure of the top platen by reducing the number of beams, so as to make it more compliant. Fig. 5.10 is a test result of displacement done on a second generation prototype of CFA. The tests are done in the same conditions as previously discussed (DC voltage, drop volume and gap).
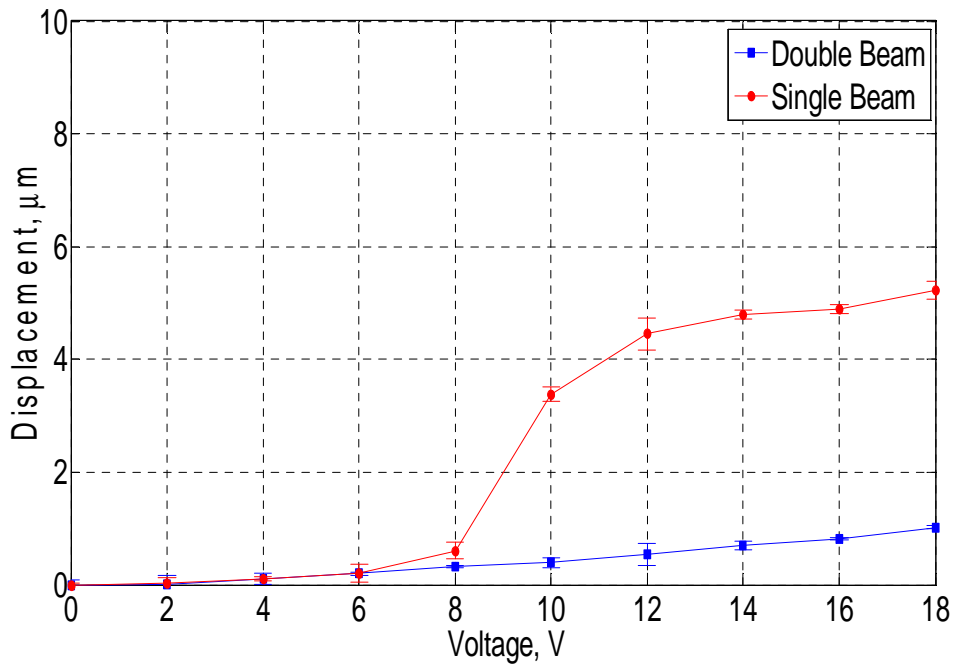
Fig. 5.9 Static displacement vs. voltage for first and second generation CFA prototypes

Fig. 5.9 shows the displacement of a second generation prototype is about 5 μm at 18 V while it is about 1 μm in the first generation CFA prototype. (In fact, the maximum out of plane displacement was observed to be approximately 12 μm at 40 V for the second generation prototype. Unfortunately, significant leakage current was recorded for applied potentials greater than 18 V, see Fig. 5.10. These results were considered to be unreliable so are not published here.)
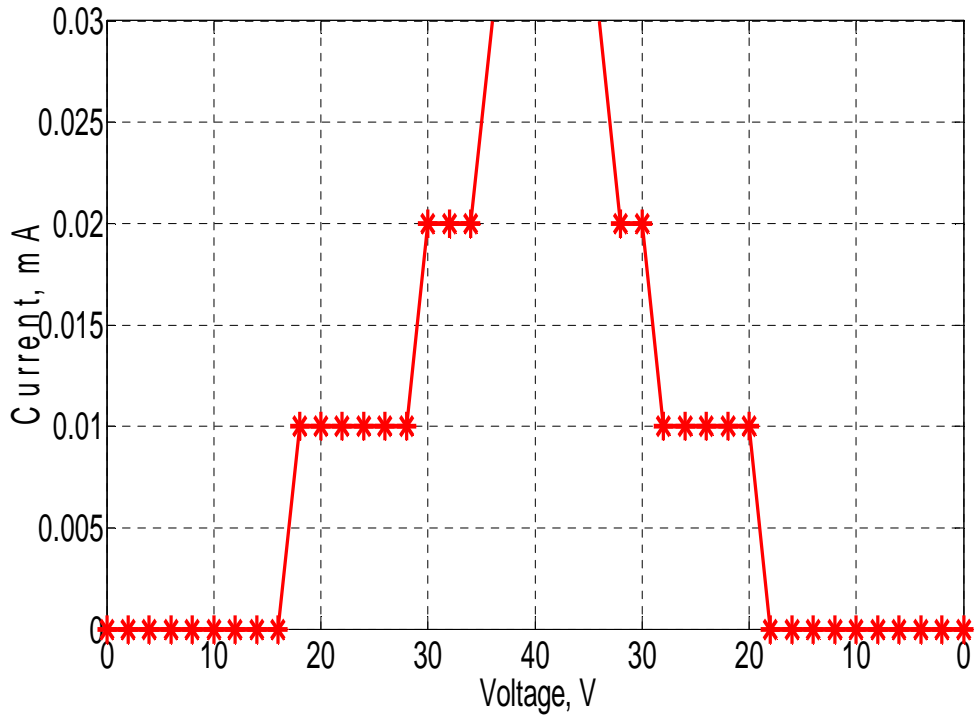
Fig. 5.10 The leakage current vs. voltage (The second generation prototype of CFA)

5.2.2 Dynamic Displacement Measurements

5.2.2.1 CFA Dynamic Displacement Measurements at 1 Hz

Dynamic tests were performed with the same displacement measurement setup, but with different time modulated signals. We used Labview to control a National Instruments (NI) myDAQ card connected with the amplifier to produce various signals. For example, AC signals were employed with an amplitude sweeping from 0 to 30 V or (40 V), and then back to 0 V. These AC signals were tested with frequencies of either 1 or 1000 Hz. We observe that electrowetting can follow an AC signal at 1 Hz; the resulting displacement is at twice the frequency since the actuation is proportional to the square of the applied voltage. However the drop shows a quasistatic behavior

when an AC signal at 1 kHz is applied. This frequency is too high for the electrowetting to follow the applied field; the response is thus related to the rms value of the signal. From the displacement results using the 1 kHz signals, we observe actuator performance similar to the DC results. This result is consistent with the dynamic electrowetting test results described in Chapter 2.

Results shown in red in Fig. 5.11 illustrate displacements using 1 Hz AC signals. In this experiment, a sinusoidal voltage is applied, with the amplitude increasing in 1V steps from 0 to 30 V and back to 0 V. Each voltage level is held for 1 s; i.e., a 1 V peak sinusoid for the first second, 2 V for the next second, etc.. The maximum displacement of a CFA is about 2 μm. The gap is estimated to be about 200 μm. All dynamic tests were done on the second generation prototypes.

Also results shown on this graph are the displacements obtained when the device is operated in electrostatic mode in blue, without a liquid drop. In this case, the maximum displacement is about 0.2 μm. From these results we can tell again that a CFA can provide displacements more than 10 times greater than that of a comparably sized electrostatic actuator. In both cases the output displacement signal is at double the frequency of the input voltage, which is expected since an attractive force will result regardless of the voltage polarity.

The CFA displacements in Fig. 5.11 (red curves), show an asymmetry between the positive and negative half cycles. Available evidence strongly supports that this is caused by an internal voltage drop generated inside the semiconductor substrate, this drop acting as a DC bias. To investigate this effect, we fabricated CFAs where both the

top and bottom plates are P type wafers and an alternate configuration, described next.
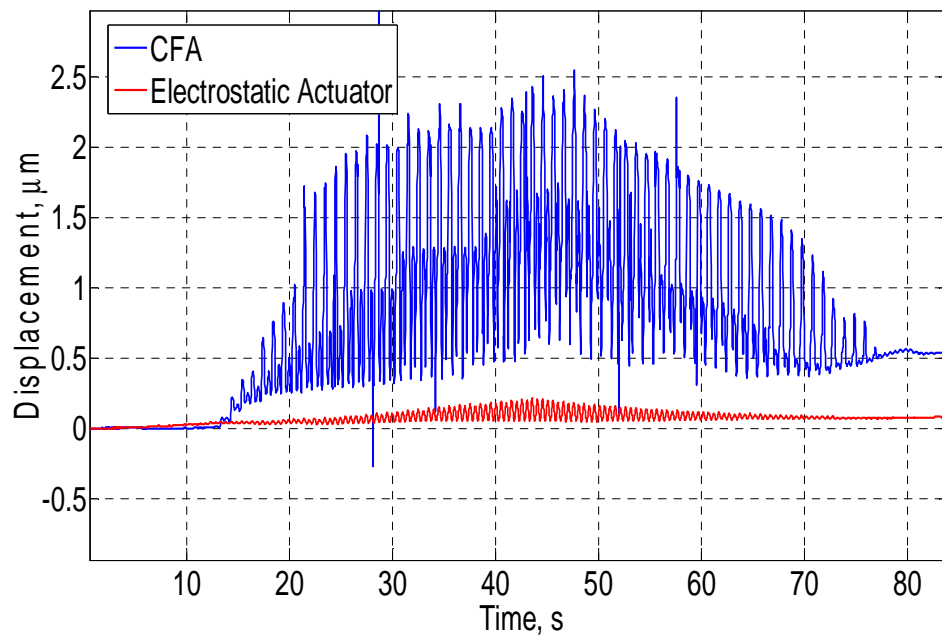
(a)
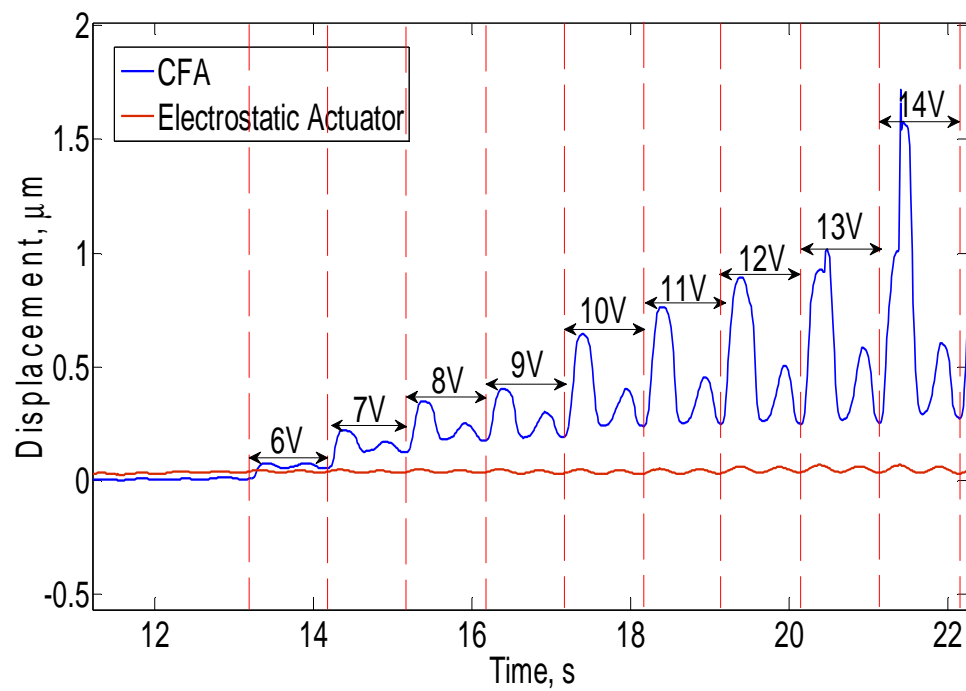
(b)

Fig. 5.11 The dynamic displacement vs. time (b is a zoom in part of picture a from 12 s to 22 s)

A simple equivalent electrical model for the CFA is two metal-oxide-

semiconductor (MOS) capacitors in series. Since we are using semiconductor wafers as the substrate electrodes, the applied voltage will tend to accumulate one surface and deplete or invert the other when both wafers are the same conductivity type (P or N type). However, if the wafers are opposite conductivity type, they will both accumulate for one voltage polarity, and both will deplete or invert synchronously for the opposite voltage polarity.

CFA prototypes were fabricated using P type silicon wafer for the top platen and an N type wafer for the bottom plate. Results are shown in Fig. 5.12. Here we applied a 1Hz AC signal from 0 to 50 V and back to 0 V. The maximum out of plane displacement was approximately about 2 μm corresponding to a 34 V peak to peak signal. At higher voltages, an electrolysis was observed in the video image (indicative of high leakage current) and a corresponding reduced displacement is also seen. From the video it was also observed that the contact line was pinned at one side, i.e. only the curvature of the other side of the bridge appeared to change. As a result, the force produced by this CFA would seem to be reduced resulting in only 2 μm out of plane displacement at 19 V_{rms} (V_{rms}=.707*V_{AC}). An analysis of the peak asymmetry in this configuration is described later.

(a)

(b)
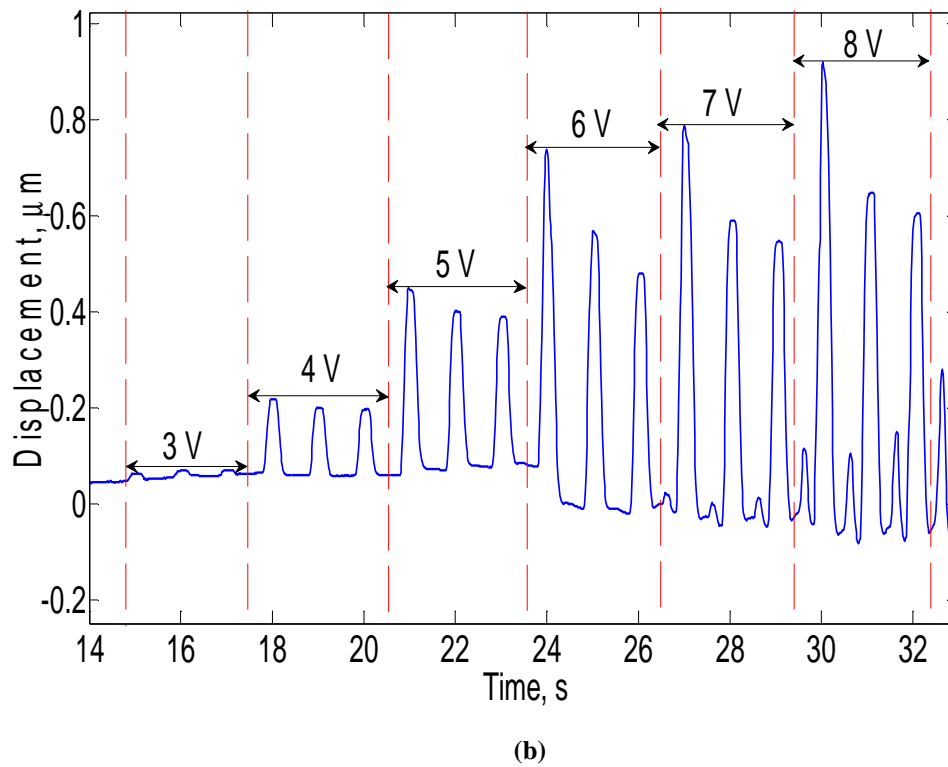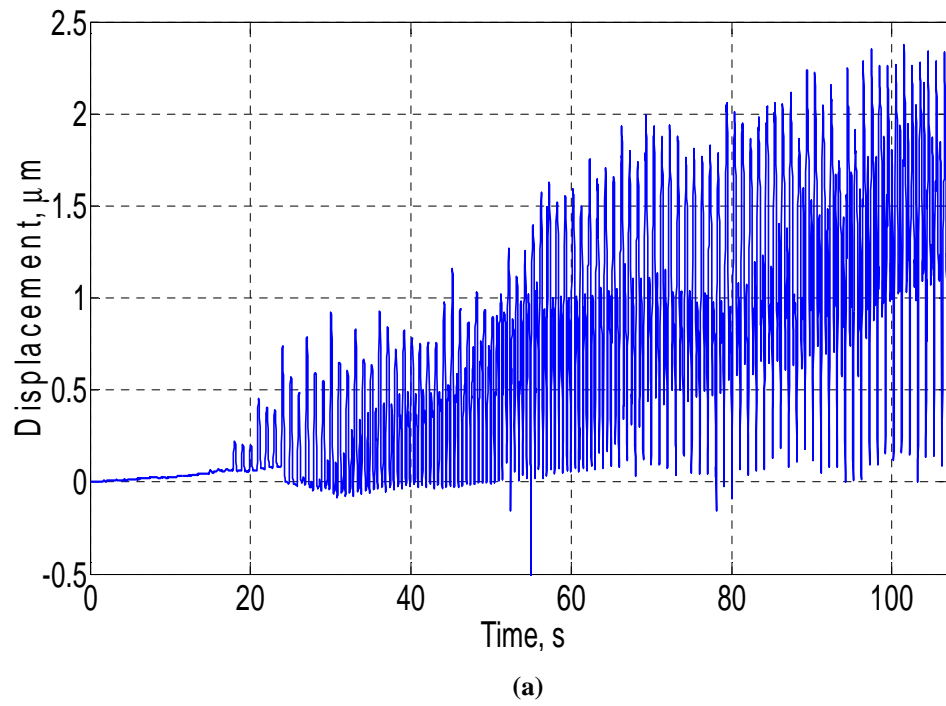
Fig. 5.12 The dynamic displacement vs. time (The second generation prototype of CFA, b is a zoom in picture of a, the label is the AC amplitude)

Two interesting phenomena were observed during this test, see Fig. 5.11-Fig. 5.12.

First, the number of peaks in displacement per cycle of voltage changes. At a lower voltage level, only one peak per cycle occurs. At higher voltage, peaks per cycle occur. We believe this is caused by the wafers being in different modes during the cycle: both top and bottom plates in inversion or both in accumulation. So the voltage drops in the wafers are different during the cycle in response to different modes.

The second phenomenon is the failure of the displacement to return to zero when an AC polarity is switched. This only happens when the AC amplitude is larger than 15 V. It may be due to the ion charges trapped in the polymer and that cannot respond quickly to an AC signal.

5.2.2.2 Dynamic Displacement Tests of both Electrostatic Actuators and CFAs

Following the AC tests, we design additional tests to understand the peak displacement asymmetry in the CFA dynamic response. We did electrostatic tests first with pure AC signal at 1 Hz. The amplitude of each voltage was kept constant for 3 seconds. Results of Fig. 5.13 showed that two peaks in one period were the same no matter what types of wafers were used as bottom plates. In electrostatic mode, the capacitance of the depletion or inversion layer is large compared with that of the gap between two plates. Therefore, the voltage drop is entirely across the air gap between the two plates. No asymmetry is observed since no appreciable voltage is dropped in the semiconductor layers.

71

(a)

(b)
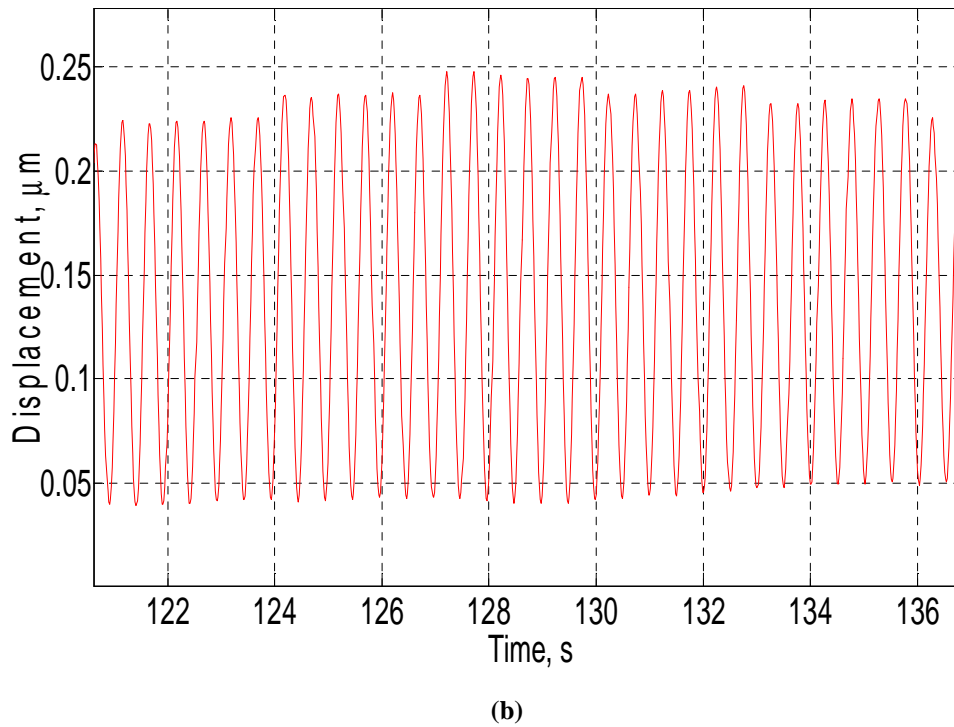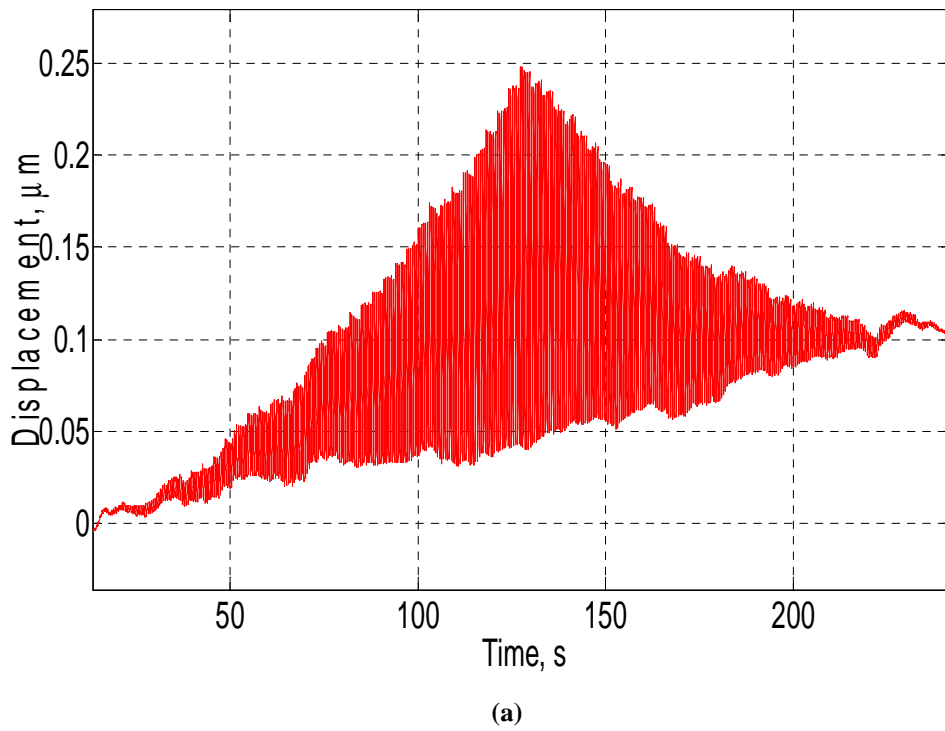
Fig. 5.13 The dynamic displacement of an electrostatic actuator vs. time (both top and bottom plates are P type, AC: 0-40 V, 1 Hz; b is a zoom in picture of a)

We also did tests with AC plus a DC bias to see if there was any influence of DC

bias on the two peak pattern for an electrostatic actuator. We incremented the AC amplitude as before, but simultaneously applied a fixed DC bias. (The AC voltage amplitude was incremented in 1 V steps every 3 s as before.) We noticed that there was only one peak per cycle at lower voltages and then two peaks per cycle at higher voltage, see Fig. 5.14. This makes sense since at higher AC voltages the net applied voltage reverses polarity, generating a doubled force at the frequency response, while at low AC voltage, the polarity does not reverse. Comparing this with the results in Section 5.2.2.1, we see that the peak asymmetry can be qualitatively accounted for if there is a DC offset in the system.

(a)

(b)
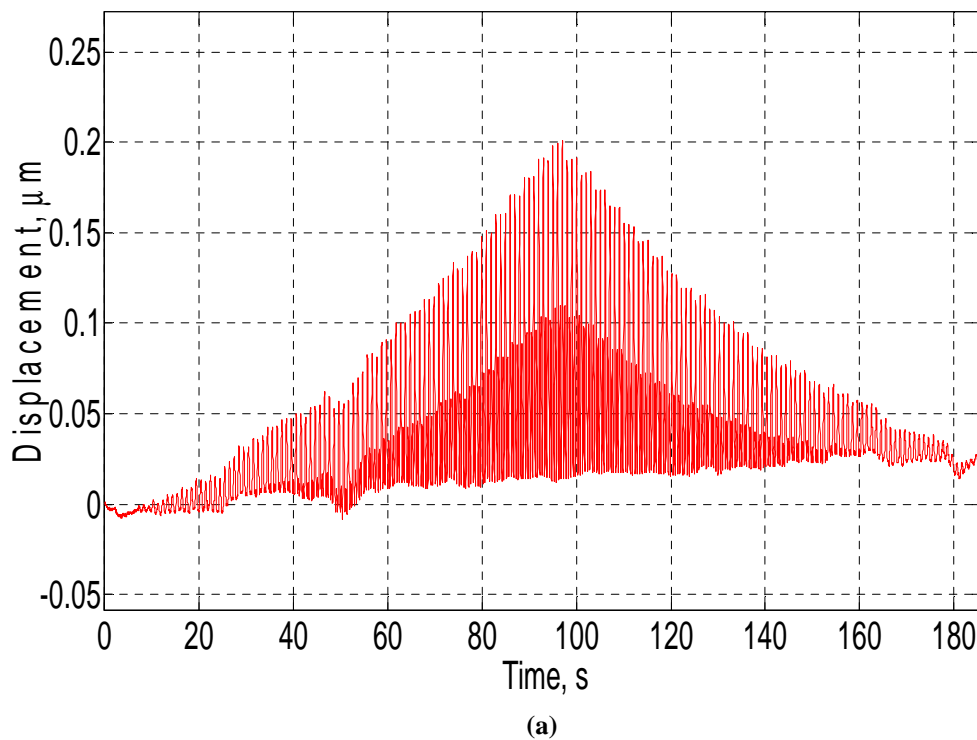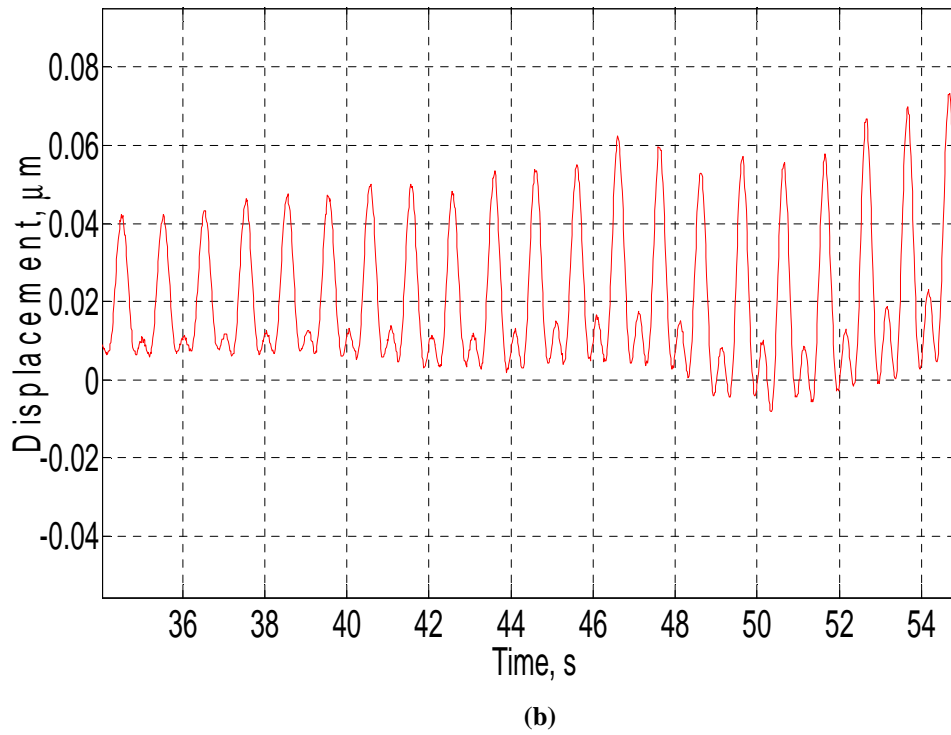
Fig. 5.14 The dynamic displacement of an electrostatic actuator vs. time (Top plate is P type and bottom plate is N type, AC: -30-0 V, 1 Hz, DC: -5 V)

We did tests on CFA prototypes (both P-P and P-N configurations) with an applied AC signal plus an adjustable DC bias. The DC bias was adjusted to remove the asymmetry in the peak displacements on each half cycle. The tests were repeated with different AC amplitudes (7 V, 10 V); the same DC offset was found to equalize the peak displacement in each case. We found that this DC offset was about 0.32 V for tests with a P type top moving platen and an N type Si wafer as a bottom plate, see Fig. 5.15. The graph shows the DC bias being switched on at t = 33 s; applying the DC offset removes the displacement asymmetry. This value is consistent with expected voltage across an inverted silicon electrode.

The DC bias needed to equalize peak displacements for a CFA prototype using P type Si wafers as both plates is about -0.08 V. The magnitude of the asymmetry is

smaller in this case since, unlike the P-N case, the P-P configuration has one electrode deplete or invert on each half cycle. The nonzero asymmetry is likely due to variations in dopant concentration for the two wafers; the wafer specifications allow the resistivity to vary over an order of magnitude range.

Based on these results, we believe the use of semiconductor electrodes will adversely impact the operation of a CFA by introducing a DC offset and also a series depletion capacitance which serves to reduce the voltage applied across the dielectric/hydrophobic layers. This suggests that metal materials, which unlike semiconductors will not deplete, should be explored as CFA electrodes.
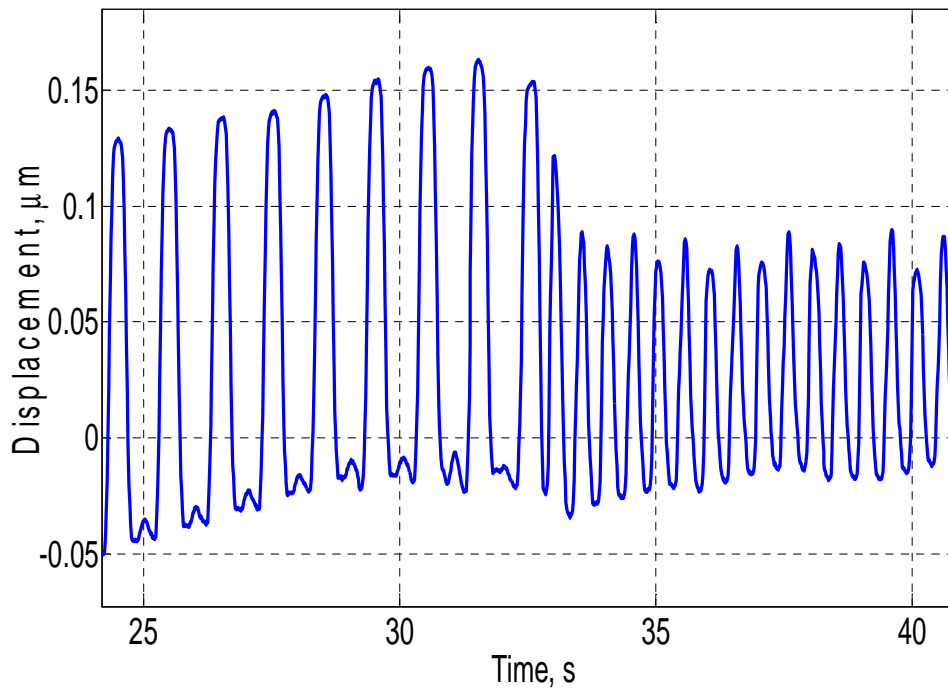
Fig. 5.15 The dynamic displacement of a CFA vs. time. The top plate is P type and bottom plate is N type AC: 7 V, 1 Hz. The DC bias is zero for t < 33 s; for t > 33 s the DC bias is : 0.32 V.

5.2.2.3 CFA Dynamic Displacement Measurements at 1 kHz

Tests were conducted using AC signals at 1 kHz with amplitude values sweeping

from 0 to 40 V (i.e. up to V_{rms}=28 V). We observe a quasi-static displacement behavior as expected, see Fig. 5.16. The results show that the maximum out of plane displacement in the tests was about 1.4 μm for a CFA but only about 0.2 μm for an electrostatic actuator with the same gap, approximately 200 μm. When the AC signal is at this higher frequency, the behavior was similar in several tests conducted: AC only, AC plus constant bias, AC plus variable bias, see Fig. 5. 17- 5. 18.
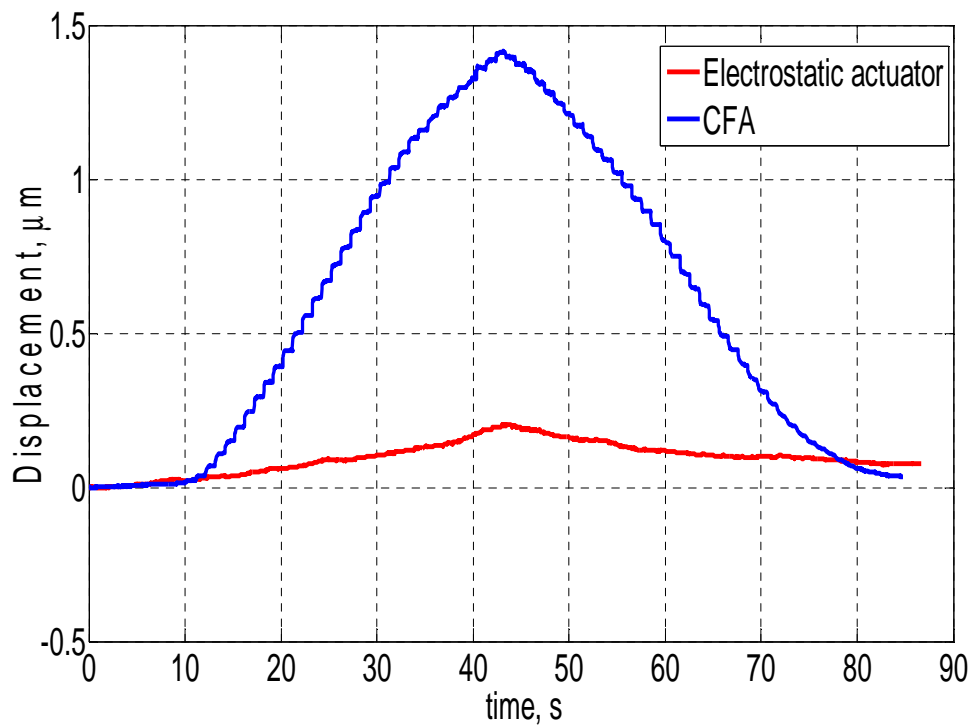
Fig. 5.16 The dynamic displacement vs. time (The second generation prototype of CFA, AC 0-40 V @ 1 kHz)
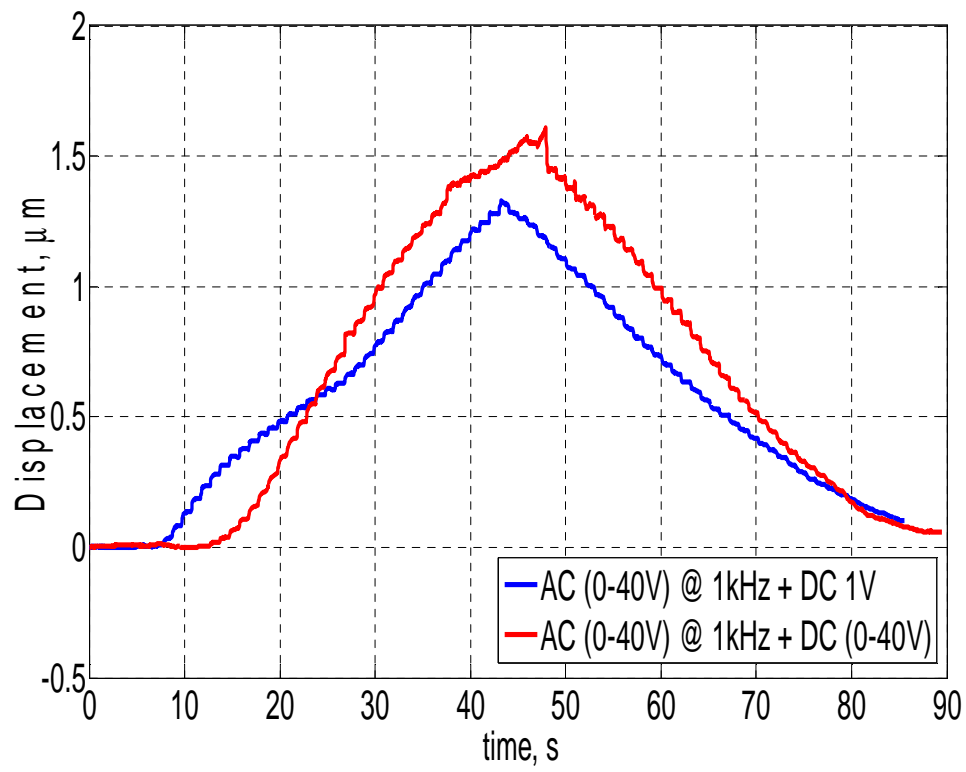
Fig. 5.17 The dynamic displacement vs. time (The second generation prototype of CFA)
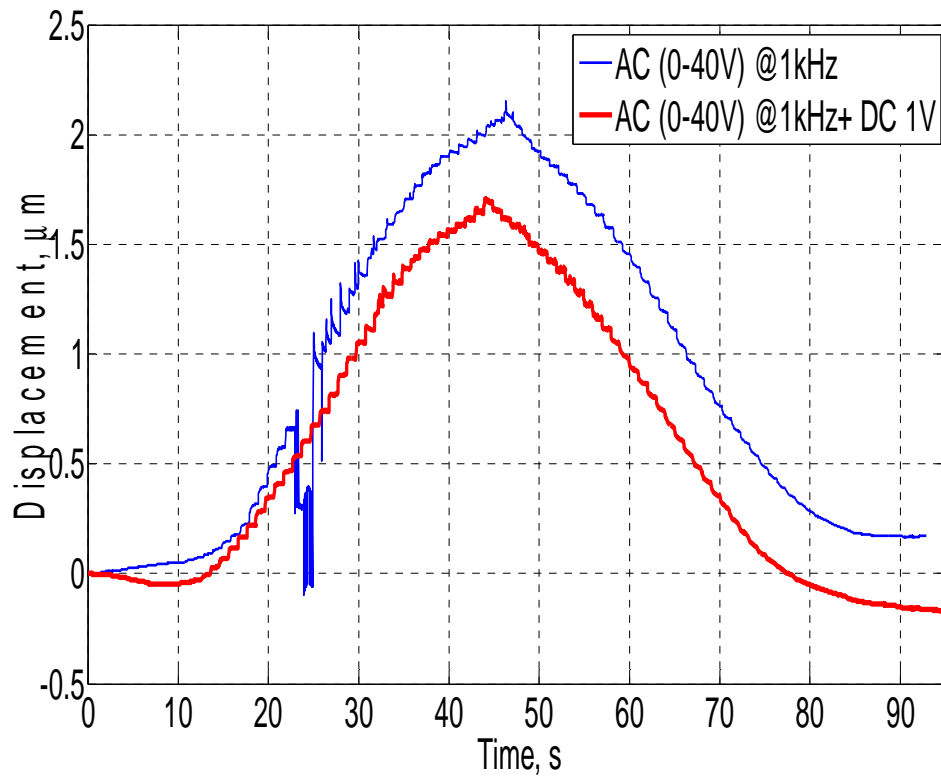
Fig. 5.18 The dynamic displacement vs. time (The second generation prototype of CFA)

5.3 CFA Force Estimation

Using the nanoindenter results discussed in Section 5.1.2, we determined the relationship between applied force and platen displacement. The experimental results are shown in Fig. 5.19 along with the simulation results from ANSYS. These experimental results are useful in estimating how much force was generated by a CFA prototype using the displacement data.
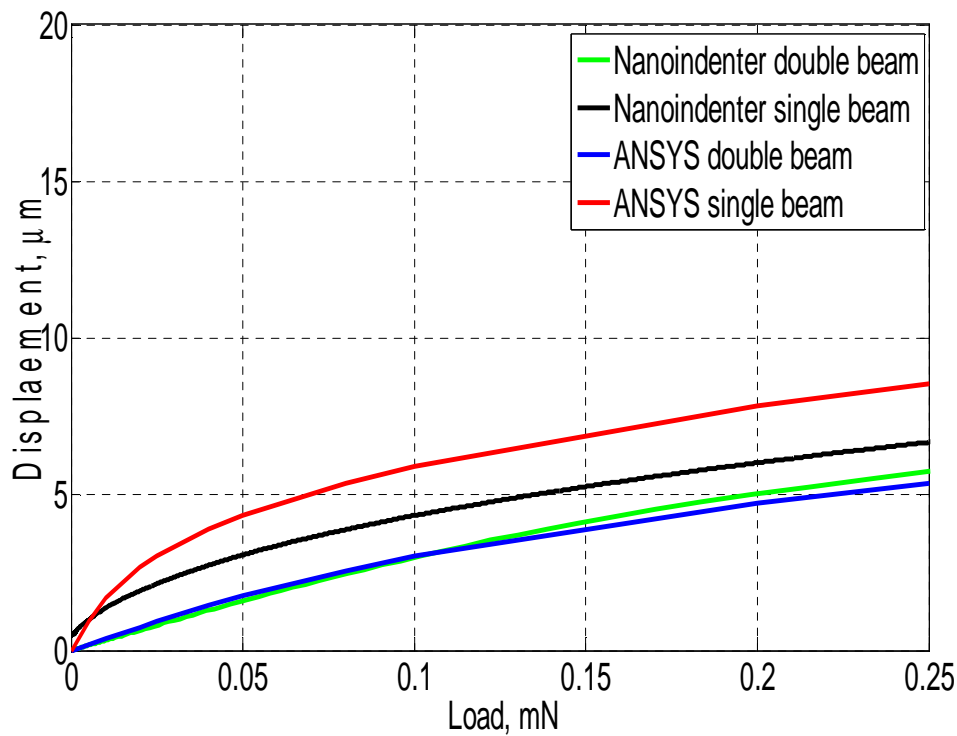
Fig. 5.19 The ANSYS simulation and nanoindenter experimental results of the static displacement v.s. the force (the first generation prototype of CFA)

After obtaining 5 μm displacement of the first generation CFA prototypes (with double flexures), we can estimate the force generated by the actuator was approximately 200 μN. This value is considerably larger than that produced by the equivalent electrostatic actuator: only 3 μN for the same applied voltage. Since the second generation CFA prototypes had the same configuration only greater compliance,

78

the force should be similar although the displacement would be different. From the results in Fig. 5.9, we observe that the displacement of the second generation prototype of CFA increases dramatically compared with that of the first generation CFA prototype under the same force. For example, the force corresponding to a 1 μm displacement of the first generation prototype can produce 4.5 μm displacement of the second generation prototype. The estimates of force corresponding to a given displacement is thus consistent with the results of our static displacement measurements of both first and second generation CFA prototypes in Fig. 5.9.

5.4 Summary

This chapter focuses on the characterization of a CFA in terms of displacement and force. It begins with a brief introduction of our custom displacement measurement system based on interferometry. This system is also used for assembling the top and bottom plates. For force characterization, we used a nanoindenter system to obtain the displacement vs. force relationship. We can estimate the force produced by the CFA by reading the displacement vs. force curve given an experimental value of displacement. We performed tests of static displacements of both first and second generation of CFAs. The maximum out-of-plane displacement is about 5 μm at 40 V applied for two plates of a first generation CFA. The displacement of the second generation CFA can reach 5 μm just at 18 V compared 1 μm with the same voltage applied to the first generation CFA. The dynamic displacement results show that a CFA responds synchronously with

an AC signal at 1 Hz while it has a quasistatic behavior when an AC signal at 1 kHz is applied. The dynamic displacement is about 2 μm at V_{AC}=34 V applied to two plates of a CFA while it is about 0.2 μm with the same voltage applied to a similar size electrostatic actuator. From the force test, we estimate the CFA can produce about 200 μN force while just 3 μN force would be produced by an electrostatic actuator with similar dimensions. These results experimentally demonstrate that our CFA can produce both considerably larger forces, resulting in a larger out of plane displacement compared with the similar size electrostatic actuators.

6 Conclusions and Future Work

This chapter summarizes and concludes the dissertation and proposes future avenues for this CFA research work.

6.1 Conclusions

A new type of microactuator, CFA, was designed, microfabricated and characterized in this work. A theoretical analysis of this structure shows that, for a given electrode size, the CFA can deliver significantly greater forces and longer actuation strokes than comparably sized electrostatic actuators. Also, the CFA can work with considerably larger electrode gaps (100 µm) with applied voltages in the tens of volts, much less than would be required for an electrostatic actuator with a comparable gap.

A CFA was designed based on the design chart presented by Nezamoddini, nonlinear beam theory, and FEA simulation. We developed a microfabrication process for a top platen using bulk micromachining of a silicon-on-insulator (SOI) wafer lapped to a thickness of 100 µm. The platen and supporting flexures are defined in the 3 µm thick top silicon layer using double-sided photolithography and bulk silicon etching in XeF_2. The top plate, supported by flexures (250 µm long, 30 µm wide and 3 µm thick) was successfully released. As a result they permit the platen to move in the direction normal to the silicon surface. Both the fixed, bottom plate and the moving

platen are covered by a 30 nm thermal SiO_2 dielectric layer and a 30 nm spin-deposited amorphous hydrophobic fluoropolymer (CYTOP) layer. The actuator is hand assembled after depositing a nominal 0.1 μL drop of electrolyte (Na_2SO_4 water / propylene glycol solution) on the fixed electrode.

Prior to the CFA assembly, the platen structure was characterized using a nanoindenter and also simulated with finite element modeling (ANSYS); the force-displacement characteristics are nonlinear. Actuator performance was assessed by applying voltage and measuring the displacement of the platen with a broadband source interferometer (Luna FiberPro2). The maximum displacement of the first generation prototype observed, approximately 5 μm, is a consequence of the large (100 μm) electrode gap in this prototype; decreasing the nominal gap would result in a larger range of displacement. With 40 V applied, the CFA is generating approximately 200 μN of force; a conventional air-gap electrostatic actuator with the same area, gap, and voltage would generate less than 3 μN. The displacement of the second generation CFA prototype is about 5 μm with 18 V applied to the two plates separated by 100 μm. The experimental characterization follows predictions of a model based on the Lippmann-Young equation. The dynamic displacement of the second CFA is about 2 μm when an AC signal at 1 Hz with a magnitude of 34 V is applied. We believe the smaller displacement is due to the pinning effects caused by hysteresis or nonoptimal electrowetting conditions.

6.2 Future Work

To improve the behavior of a CFA in terms of force and displacement, the following future work is suggested:

1. Electrowetting can be studied in an oil environment in order to reduce the hysteresis, evaporation, and environmental contamination. By reducing hysteresis and contact angle pinning, the contact angle will start changing at a lower voltage. Also the drop curvature will be changed more if the pinning behavior is reduced. In this case, the force produced a CFA will be increased resulting in a larger out of plane displacement.

2. In order to avoid the depletion issues from a semiconductor, a metal like Al can be considered to work as an electrode. Then an electroplated Al_2O_3 can be used as a dielectric layer. People in our group for another project have had a recipe for a dielectric layer of Al_2O_3 and characterized it in terms of breakdown strength. In this case, the dielectric constant can be improved from 3.8 to almost 9. As a result, the force produced by the CFA will be increased.

3. Another possible way to improve the force of the CFA is to reduce the gap between two plates, say from 100 μm to 50 μm or 20 μm. A simple way to realize it is to use a microbead with a diameter of 50 μm or 20 μm. Or we can use SU8 which is often used to pattern a high aspect ratio structure. In this case, the force will be increased from 1.35 mN (gap is 100 μm) to 2.7 mN (gap is 50 μm) or 6.75 mN (gap is 20 μm).

Appendix

1 Fabrication Procedure of Bottom Plate

Bottom plate

1. 2 inch Si wafer

2. 300 µm thick

3. (100) orientation

4. P type (Boron dopant)

5. 10-20 ohm.cm resistivity

6. One side polished

Bottom plate cleaning

1. Ethanol, D'Limonene and methanol clean

2. Buffered oxide etchant (BOE) dip for 1 min

3. Deionized (DI) water rinse for 1min

4. N_2 blow dry

Silicon dioxide (SiO_2) as a dielectric layer growth

1. Dry thermal growth of SiO_2 in rapid thermal annealing (RTA) at $1100°C$ degree

   for 10 mins with 100 sccm of O_2 flow rate

2. Measure SiO_2 layer thickness with the ellipsometry

Bottom plate cut

1. Spin AZ 4330 photoresist on the Si wafer at 2000 rpm for 30 s, wait for 5 mins at room temperature and bake it at 100°C degree for 2 mins

2. Cut the wafer into a 5 cm long and 1cm width rectangle one

3. Remove the photoresist with Acetone

4. DI water rinse for 1 min

5. N_2 blow dry

Hydrophobic layer spin

1. Mix Cytop from (Bellex International Corporation) and its solvent to 1 wt%

2. Spin 1 wt% Cytop on the Si wafer at 2000 rpm for 30 s, wait for 5mins at room temperature and bake it at 170ºC degree for 1 hour

Pattern the bottom plate for the wire connection and drop position

1. Cover the Si wafer with the window mask in the Trion plasma etching machine

2. P=50 mT, ICP-100 W, RIE=50 W, O_2=25 sccm, t=45 s

Connect a coated wire to the bottom plate

1. Connect a coated wire (30AWG from DigiKey) to the bottom plate by using a cold temperature conductive epoxy from MSChem

2. Cure it at room temperature for 3 hours

2 Fabrication Procedure of Top Moving Platen

Top moving platen

1. 4-inch SOI wafer

2. 3 µm thick of Si device layer, 1 µm thick buried oxide layer and 300 µm thick Si handle layer

3. (100) orientation for the device layer and the handle layer

4. P type (Boron dopant)

5. Resistance (0.1-0.5 ohm.cm)

6. Double side polished

Top moving platen cleaning

Silicon dioxide (SiO$_2$) as a dielectric layer growth

Top moving platen cut

These three steps are the same as those for the bottom plate except that the top moving platen size is 1 inch square.

Lapping the top moving platen

1. Stick 4 pieces SOI wafers on the glass substrate with the wax at 145ºC degree hot plate (the device layer facing down)

2. Put the glass substrate with wafers onto a hot plate at 150ºC degree with the mechanical jig for at least 1 hour

3. Cool it at room temperature for at least 30 mins

4. Set up the lapping machine with flatten plate first to level the plate

5. Put the glass substrate with wafers to the vacuum stage of the lapping machine

6. Lap the samples to 110 µm thick

7. Check the thickness of samples with the mechanical stylus once every hour

8. Release samples from the glass substrate in 70ºC degree D'Limonene for 2 hours and Methanol for 5 mins

9. DI water rinse for 1min

10. N_2 blow dry

Easy handle of samples preparation

1. Spin AZ 4330 photoresist on a glass slide at 2000 rpm for 30 s

2. Put a piece of 1 inch square wafer onto the glass slide (top side up)

3. Bake it at 100ºC degree for 2 mins

Contact pad on the top side

1. Spin LOR5B resist on the wafer at 2000 rpm for 30 s , wait at room temperature for 5 mins and bake it at 100ºC degree for 1 min, 130ºC degree for 1 min and 160ºC degree for 2 mins

2. Spin AZ 4330 photoresist on a glass slide at 4000 rpm for 30 s, wait at room temperature for 5 mins and bake it at 110ºC degree for 2 mins

3. Patter the contact pad with mask 1 in 8.4 with MJB4 exposure for 200 s with

the soft contact at 320 nm UV wave length

4. Develop the pattern in 1:3 solution (AZ400k:DI water) for 45 s and DI water rinse for 1 min

5. N_2 blow dry

6. Check the pattern under the microscope

7. BOE etch for 1 min and DI water rinse for 1 min

8. N_2 blow dry

9. Load samples in Ebeam and deposit 200 nm thick Al on them

10. Lift off the Al layer beyond the contact pad areas in the heated (90ºC degree) N-Methylpyrrolidone (NMP) for 10 mins

11. DI water rinse for 1 min

12. N_2 blow dry

Al deposition on the back side of wafers

1. Load samples with the bottom side up with a 8mm square mask covering the center part into Ebeam

2. Deposit 200 nm Al on them

Easy handle of samples preparation

1. Spin AZ 4330 photoresist on a glass slide at 2000 rpm for 30 s

2. Put a piece of 1 inch square wafer onto the glass slide (bottom side up)

3. Bake it at 100ºC degree for 2 mins

Back side pattern

1. Spin AZ 4330 photoresist on a glass slide at 4000 rpm for 30 s, wait at room temperature for 5 mins and bake it at 110ºC degree for 2 mins

2. Patter the contact pad with mask 2 in 8.4 with MJB4 exposure for 200 s with the soft contact at 320 nm UV wave length

3. Develop the pattern in 1:3 solution (AZ400k:DI water) for 45 s and DI water rinse for 1 min

4. N_2 blow dry

5. Check the pattern under the microscope

6. Residual photoresist clean in Trion plasma machine (P=50 mT, ICP=100 W, RIE=50 W, O_2=25 sccm, t=45 s)

7. Tape the samples with HR resist tapes

8. Load samples into XeF_2 Si dry etching machine (Cycle number=10, each cycle duration =60 s, N_2 pressure=3 mT)

9. Check the pattern under the microscope

10. Release tapes from samples in Acetone-2 mins

11. DI water rinse for 1 min

12. N_2 blow dry

13. Spin AZ 4330 photoresist along the wafer edge to cover the marks on the back side of the wafer at 2000 rpm for 30 s

14. Bake it at 100ºC degree for 2 mins

15. Tape the wafer again with HF resist tape

16. Etch the buried oxide layer in BOE for 1 hour

17. DI water rinse for 1 min

18. N$_2$ blow dry

19. Release tapes in Acetone and samples from the glass slides in the heated (90ºC degree) N-Methylpyrrolidone (NMP) for 10 mins

20. DI water rinse for 1 min

21. Dry samples naturally

Easy handle of samples preparation

1. Spin AZ 4330 photoresist on a glass slide at 2000 rpm for 30 s

2. Put a piece of 1 inch square wafer onto the glass slide (top side up)

3. Bake it at 100ºC degree for 2 mins

Top side pattern

1. Spin LOR5B resist on the wafer at 2000 rpm for 30 s , wait at room temperature for 5 mins and bake it at 100ºC degree for 1 min, 130ºC degree for 1 min and 160ºC degree for 2 mins

2. Spin AZ 4330 photoresist on a glass slide at 3500 rpm for 30 s, wait at room temperature for 5 mins and bake it at 110ºC degree for 2 mins

3. Patter the front side with mask 3 in 8.4 with EVG620 double aligner for 300 s with the gap exposure mode

4. Develop the pattern in 1:3 solution (AZ400k:DI water) for 45 s and DI water

rinse for 1 min

5. Check the pattern under the microscope

6. BOE etch for 1min and DI water rinse for 1 min

7. Dry etch 3 μm thick Si in Trion plasma machine (p=100 mT, ICP=300 W, RIE=150 W, O_2=3 sccm, SF_6=25 sccm, t=120 s)

8. Check the pattern under the microscope

9. Release samples from the glass slides in the heated (90ºC degree) N-Methylpyrrolidone (NMP) for 2 hours

10. Dry samples in the Critical Point Drier (CPD) for 45 mins

Fix top moving platen

1. Fix the PDMS onto the Acrylic with the super glue

2. Stick the top moving platen on the PDMS with the super glue

3. Blade the conductive epoxy on the 25 μm thick Al foil with 25 μm thick Kapton as spacers

4. Stick the Al foil with the conductive epoxy onto the contact pad of the wafer

5. Cure for 2 hours at least

6. Anchor the Al foil into the Acrylic

7. Stick the wire to the top side of the anchored side of the Al foil and cure it for 2 hours at least

Bibliography

1.   D. Bell, T. Lu., N. Fleck, and S. Spearing, MEMS actuators and sensors: observations on their performance and selection for purpose. Journal of Micromechanics and Microengineering, 2005. 15: p. 153-164.

2.   E. Thielicke, E. Obermeier, Microactuators and their technologies. Mechatronics, 2000. 10: p. 431-455.

3.   Ing. Habil, H. Janocha, Microactuators-Principles, Applications, Trends. Laboratory for Process Automation (LPA), Saarland University: Saarbrucken, Germany.

4.   C. Liu, Y. B. Cohen, Scaling Laws of Microactuators and Potential Applications of Electroactive Polymers in MEMS. in Proceedings of SPIE's 6th Annual International Symposium on Smart Structures and Materials. 1999. Newport Beach, CA.

5.   M. J. Madou, Fundamentals of microfabrication: the science of miniaturization. 2002: CRC Press.

6.   P. Abgrall, A. M. Gu, Lab-on-chip technologies: making a microfluidic network and coupling it into a complete microsystem—a review. J. Micromech. Microeng., 2007. 17: p. 15-49.

7.   M. Tabib-Azar, Microactuators Electrical, Magnetic, Thermal, Optical, Mechanical, Chemical and Smart Structures. Electronic Materials: Science and Technology, ed. H.L. Tuller. 1998: Kluwer Academic Publishers.

8.   D. Mark, S. Haeberle, G. Roth, Felix von Stetten and R. Zengerle, Microfluidic lab-on-a-chip platforms: requirements, characteristics and applications. Chem. Soc. Rev., 2010. 39: p. 1153-1182.

9.   R. Zengerle, D. Mark, and Felix von Stetten, Microfluidic platforms for lab- on-a-chip applications. Lab Chip, 2007: p. 1094-1110.

10.   K. B. Lee, and Y. H. Cho, Laterally Driven Electrostatic Repulsive-Force Microactuators Using Asymmetric Field Distribution. JOURNAL OF MICROELECTROMECHANICAL SYSTEMS, 2001. 10(1).

11.   Y. Zhao, Fabrication of high-aspect-ratio polymer-based electrostatic comb drives using the hot embossing technique. J. Micromech. Microeng., 2003. 13: p. 430–435.

12.   Han-Sheng Lee, Chi H. Leung, J. Shi, Shih-Chia Chang, S. Lorincz, and I. Nedelescu, Integrated Microrelays: Concept and Initial Results. JOURNAL OF MICROELECTROMECHANICAL SYSTEMS, 2002. 11(2).

13.   L. Li, J. G. Brown and D. Uttamchandani, Study of scratch drive actuator force characteristics. J. Micromech. Microeng., 2002. 12: p. 736–741.

14.   M. A. Erismis, H. Pereira Neves, P. De Moor, C. Van Hoof, R. Puers, *Low voltage electrostatic inchworm actuators in aqueous environments.* Prodedia Chemistry 1 2009: p. 686-689.

15.   M. Mita, M. Arai, S. Tensaka, D. Kobayashi, *A Micromachined Impact Microactuator Driven by Electrostatic Force.* JOURNAL OF MICROELECTROMECHANICAL SYSTEMS, 2003. **12**(1).

16.   M. Shikida, K. Sato, and T. Harada, *Fabrication of an S-shaped Microactuator.* JOURNAL OF MICROELECTROMECHANICAL SYSTEMS, 1997. **6**(1).

17.   R. Yeh, S. Hollar, and K. S. J. Pister, *Single Mask, Large Force, and Large Displacement*

Electrostatic Linear Inchworm Motors. JOURNAL OF MICROELECTROMECHANICAL SYSTEMS, 2002. **11**(4).

18.   R. Legtenberg, J. Gilbert, S. D. Senturia and M. Elwenspoek, *Electrostatic Curved Electrode Actuators.* JOURNAL OF MICROELECTROMECHANICAL SYSTEMS, 1997. **6**(3).

19.   J. D. Grade, H. Jerman, and T. W. Kenny, *Design of large deflection electrostatic actuators.* JOURNAL OF MICROELECTROMECHANICAL SYSTEMS, 2001.

20.   J. Li, *Electrostatic Zipping Actuators and Their Application to MEMS*, in *Dept. of Mechanical Engineering*. 2004, Massachusetts Institute of Technology.

21.   M. A. Erismis, H. P. Neves., R. Puers, and C. V. Hoof, *A low-voltage large-displacement large-force inchworm actuator.* JOURNAL OF MICROELECTROMECHANICAL SYSTEMS, 2008. **17**(6).

22.   G. Krijnen and N. Tas, *Micromechanical Actuators*. MESA + Research Institute, Transducer Technology Laboratory, University of Twente, The Netherlands: http://www.utwente.nl/ewi/tst/education/el-bach/mandt/extra/background/mems_actuators.pdf.

23.   V. T. Srikar, S. M. Spearing, *Materials selection for microfabricated electrostatic actuators.* Sensors and Actuators A 2003. **102**: p. 279-285.

24.   H. J. Cho and C. H. Ahn, *A Bidirectional Magnetic Microactuator Using Electroplated Permanent Magnet Arrays.* JOURNAL OF MICROELECTROMECHANICAL SYSTEMS, 2002. **11**(1).

25.   M. Ruan, J. Shen, and C. B. Wheeler, *Latching Micromagnetic Relays.* JOURNAL OF MICROELECTROMECHANICAL SYSTEMS, 2001. **10**(4).

26.   M. Khoo, C. Liu, *Micro magnetic silicone elastomer membrane actuator.* Sensors and Actuators A, 2001. **89**: p. 259-266.

27.   I. Roch, Ph Bidaud, D. Collard and L. Buchaillot, *Fabrication and characterization of an SU-8 gripper actuated by a shape memory alloy thin film.* J. Micromech. Microeng., 2003. **13**: p. 330–336.

28.   T. J. Lu, J. W. Huntchinson, A. G. Evans, *Optimal design of a flexural actuator.* Journal of the Mechanics and Physics of Solids 2001. **49**: p. 2071 – 2093.

29.   T. Moulton, G. K. Ananthasuresh, *Micromechanical devices with embedded electro-thermal-compliant actuation.* Sensors and actuators A, 2001. **90**: p. 38-48.

30.   Q. Q. Zhang, S. J. Gross, S. Tadigadapa, T. N. Jackson, F. T. Djuth, S. Trolier-McKinstry, *Lead zirconate titanate films for d33 mode cantilever actuators.* Sensors and Actuators A 2003. **105**: p. 91–97.

31.   T. Bourouina, E. Lebrasseur, G. Reyne, A. Debray, H. Fujita, A. Ludwig, E. Quandt, H. Muro, T. Oki, and A. Asaoka, *Integration of Two Degree-of-Freedom Magnetostrictive Actuation and Piezoresistive Detection: Application to a Two- dimensional Optical Scanner.* JOURNAL OF MICROELECTROMECHANICAL SYSTEMS, 2002. **11**(4).

32.   C. R. Knsope,, *Method and System for Capillary Force Actuators*. May 15, 2012: U.S.

33.   S. A. Nezamoddini, *Capillary Force Actuators*, in *Mechanical and Aerospace Engineering*. 2008, University of Virginia.

34.   G. Lippmann, *Relations entre les ph´enom`enes ´electriques et capillaires* Ann. Chim. Phys, 1875. **5**: p. 594.

35.   F. Mugele and J. C. Baret, *Electrowetting: from basics to applications.* J.Phys.: Condens. Matter, 2005. **17**: p. 705-744.

36.   J. Lee, H. Moon , J. Fowler, T. Schoellhammer, C. J. Kim, *Electrowetting and electrowetting-on-dielectric for microscale liquid handling.* Sensors and Actuators A 2002. **95**: p. 259-268.

37.   A. G. Papathanasiou, A. T. Papaioannou and A. G. Boudouvis, *Illuminating the connection between contact angle saturation and dielectric breakdown in electrowetting through leakage current measurements.* Journal of Applied Physics, 2008. **103**.

38.   S. W. Walker, B. Shapiro and R. H. Nochetto, *Electrowetting with contact line pinning: Computational modeling and comparisons with experiments.* Physics of Fluids 2009. **21**(10).

39.   Im Maesoon, D. H. Kim, J. H. Lee, J. B. Yoon, and Y. K. Choi, *Electrowetting on a Polymer Microlens Array*, in *Langmuir*. 2010.

40.   B. Raj, M. Dhindsa, N. R. Smith, R. Laughlin and J. Heikenfeld, *Ion and Liquid Dependent Dielectric Failure in Electrowetting Systems.* Langmuir, 2009. **10**.

41.   H. You, and A. J. Steckl, *Three-color electrwetting display device for electronic paper.* Applied Physics letters, 2010. **97**.

42.   P. Muller, R. Feuerstein, and H. Zappe, *A fully Integrated optofluidic micro-iris*, in *25th IEEE MEMS*. 29 January- 2 February, 2012: Paris, France.

43.   A. Takei, K. Matsumoto and I. Shomoyama, *Capillary Motor driven by electrowetting.* Lab on a chip, 2010. **10**(14): p. 1741-1880.

44.   R. Digilov, *Charge-Induced Modification of Contact Angle: The Secondary Electrocapillary Effect*, in *Langmuir*. 2000. p. 6719-6723.

45.   K. H. Kang, *How Electrostatic Fields Change Contact Angle in Electrowetting*, in *Langmuir*. 2002. p. 10318-10322.

46.   J. Buehrle, S. Herminghaus and F. Mugele, *Interface Profiles near Three-Phase Contact Lines in Electric Fields.* Physical Review Letters, 2003. **91**(8).

47.   T. B. Jones, *An electromechanical interpretation of electrowetting* J. Micromech. Microeng., 2005. **15**: p. 1184-1187.

48.   F. Mugele, *Fundamental challenges in electrowetting: from equilibrium shapes to contact angle saturation and drop dynamics.* Soft Matter, 2009. **5**: p. 3377-3384.

49.   R. Gupta, G. K. Oliver and J. Frechette, *Invariance of the Solid-Liquid Interfacial Energy in Electrowetting Probed via Capillary Condensation*, in *Langmuir*. 2010.

50.   http://www2.dupont.com/Teflon_Industrial/en_US/store/teflon_af_home.html.

51.   H. J. J. Verheijen, and M. W. J. Prins, *Reversible electrowetting and trapping of charge: model and experiments.* Langmuir, 1999. **15**: p. 6616-6620.

52.   A. G. Papathanasiou, and A. G. Boudouvis, *Manifestation of the connection between dielectric breakdown strength and contact angle saturation in electrowetting.* Appl. Phys. Lett., 2005. **86**.

53.   B. Shapiro, H. Moon, R. L. Garrell, and C. J. Kim, *Equilibrium behavior of sessile drops under surface tension, applied external fields, and material variations.* J. Appl. Phys., 2003. **93**(9): p. 5794-5811.

54.   M. Vallet, M. Vallade, B. Berge, *Limiting phenomena for the spreading of water on polymer films by electrowetting.* The European Physical Journal B - Condensed Matter and Complex Systems, 1999. **11**(4): p. 583-591.

55.   H. J. J. Verheijen, and M. W. J. Prins, *Reversible Electrowetting and Trapping of Charge: Model and Experiments.* Langmuir, 1999. **15**: p. 6616-6620.

56.   V. Peykov, A. Quinn, and J. Ralston, *Electrowetting: a model for contact-angle saturation.* Colloid and Polymer Science, 2000. **278**: p. 789-793.

57.   A. Quinn, R. Sedev, J. Ralston, *Contact Angle Saturation in Electrowetting.* J. Phys. Chem. B, 2005. **109**: p. 6268-6275.

58.   R. Sedev, *Electrowetting: Electrocapillary, Saturation and Dynamics.* Eur. Phys. J. Special Topics 2011. **197**: p. 307-319.

59.   http://www.agc.com/english/chemicals/shinsei/cytop/about.html.

60.   http://www.pinnaclesys.com.

61.   R. Malk, L. Davoust, and Y. Fouillet, *EWOD-based chip characterization under AC voltage.* Microelectronic Engineering 2011. **88**: p. 1745-1748.

62.   S. B. Q. Tran, D. Byun, V. D. Nguyen and T. S. King, *Liuqid meniscus oscillation and drop ejection by ac voltage, pulse and superimposing dc to ac voltages.* Physical Review E, 2009. **80**.

63.   Q. Jing, *Modeling and Simulation for Design of Suspended MEMS.* 2003, Carnegie Mellon University.